

UC San Diego

UC San Diego Electronic Theses and Dissertations

Title

Water Oxidation Catalysts with Heteroatom Pendant Bases and Instrumentation for Quantifying Oxygen

Permalink

<https://escholarship.org/uc/item/6tw810dc>

Author

Nash, Aaron Gabriel

Publication Date

2019

Peer reviewed|Thesis/dissertation

UNIVERSITY OF CALIFORNIA SAN DIEGO

SAN DIEGO STATE UNIVERSITY

Water Oxidation Catalysts with Heteroatom Pendant Bases and
Instrumentation for Quantifying Oxygen

A dissertation submitted in partial satisfaction
of the requirements for the degree Doctor of Philosophy

in

Chemistry

by

Aaron Gabriel Nash

Committee in charge:

University of California, San Diego

Professor John Crowell
Professor Arnold Rheingold

San Diego State University

Professor Douglas Grotjahn, Chair
Professor Jing Gu
Professor Roland Wolkowicz

2019

Copyright
Aaron Gabriel Nash, 2019
All rights reserved

The Dissertation of Aaron Gabriel Nash is approved, and it is acceptable in quality and form for publication on microfilm and electronically:

Chair

University of California San Diego
San Diego State University
2019

DEDICATION

For Mom and Dad

EPIGRAPH

The greater is the circle of light, the greater is the boundary of the darkness by which it is confined. But, notwithstanding this, the more light we get, the more thankful we ought to be, for by this means we have the greater range for satisfactory contemplation. In time the bounds of light will be still farther extended; and from the infinity of the divine nature, and the divine works, we may promise ourselves an endless progress in our investigation of them: a prospect truly sublime and glorious.

— Joseph Priestley
in *Experiments and Observations with a Continuation of the Observations on Air* (1781), Vol. 2, Preface, ix.

Table of Contents

Signature Page	iii
Dedication	iv
Epigraph	v
Table of Contents	vi
List of Figures	viii
List of Tables	xi
Acknowledgements	xii
Vita	xv
Abstract of the Dissertation	xvii
Chapter 1 – A Renewable Energy Cycle from Water	1
1.1 Depletion of Fossil Fuels	1
1.2 Global Warming	2
1.3 Storing Energy from the Sun in Water	5
1.4 Electrocatalysis – A review	9
1.6 A Brief History of $[(\text{terpy})(\text{bipy})\text{Ru}(\text{OH}_2)]^{2+}$	15
1.7 Designing a Better Water Oxidation Catalyst	21
References	24
Chapter 2 – Appending Heteroatom Pendant Bases to the $[(\text{terpy})(\text{phen})\text{Ru}(\text{OH}_2)]^{2+}$ Platform	27
2.1 A Review of Pendant Bases in Molecular Ruthenium Water Oxidation Catalysis	27
2.2 Literature Review of Sulfonate Ligands on Ruthenium Catalysts	32
2.3 Motivation	37
2.4 Synthesis and Characterization	39
2.5 Testing with Sacrificial Oxidant	47
2.7 Computational Results	55
2.8 EPR Results	60
2.9 Conclusions and Future Work	67
2.10 Experimental Details	71
Acknowledgements	115
References	116

Chapter 3 – Improved Instrumentation for Quantifying Oxygen	119
3.1 To Build a Better Pressure Testing Cell.....	119
3.2 Measuring oxygen and trace gases in an electrochemical cell.....	125
3.3 Conclusions and Future Work	134
References	135

LIST OF FIGURES

Figure 1. 1 Atmospheric carbon dioxide concentrations in parts per million (ppm) for the past 800,000 years.....	3
Figure 1. 2 Greenhouse gas emissions by type.	4
Figure 1. 3 Comparison of volumetric and gravimetric density of fossil fuels and hydrogen gas	6
Figure 1. 4 Schematic of a photoelectrochemical cell	8
Figure 1. 5 Free energy diagram for an endothermic reaction.	11
Figure 1. 6 Comparison of catalysis with a sacrificial oxidant vs. electrocatalysis.	12
Figure 1. 7 “Z-scheme” depicting the electron transport chain of the light cycle of photosynthesis	13
Figure 1. 8 (A) X-ray structure of the oxygen evolving complex; (B) scheme depicting attack of a bound hydroxide on a manganese oxo; (C) scheme depicting radical coupling of a manganese terminal oxo and a structural oxygen (figure from ref. 25). ...	14
Figure 1. 9 Meyer’s proposed mechanism for water oxidation by [(terpyridine)(LL)Ru(OH ₂)] ²⁺	18
Figure 1. 10 Pushkar’s proposed mechanism for water oxidation by [(terpy)(bipy)Ru(OH ₂)] ²⁺	21
Figure 2. 1 Improved synthesis of 2-chlorophenanthroline.....	39
Figure 2. 2 Synthetic scheme for diisopropyl (2-(1,10-phenanthrolin-2-yl)phosphonate and its phosphonic acid sodium salt	40
Figure 2. 3 Synthesis of 2.22	41
Figure 2. 4 Synthesis of 2.23	42
Figure 2. 5 Synthesis of 2.24	43
Figure 2. 6 Solid state structure of 2.21-BARF	45
Figure 2. 7 Solid state structure of 2.24-OTf	46
Figure 2. 8 O ₂ evolution traces determined by manometry for 2.6 , 2.21 , and 2.24	47

Figure 2. 9	O ₂ evolution over 12h of catalysis at different concentrations of 2.24	49
Figure 2. 10	O ₂ evolution within the first 10 minutes of catalysis at different concentrations of 2.24	49
Figure 2. 11	Determination of pseudo first order rate constant of 2.24	50
Figure 2. 12	Comparison of cyclic voltammograms of 2.6 , 2.21 , and 2.24	51
Figure 2. 13	Variable scan rate study of 2.24	51
Figure 2. 14	Plot of peak current vs. square root of scan rate for 2.24	52
Figure 2. 15	Pourbaix diagram of 2.12	54
Figure 2. 16	First PCET oxidation of 2.24	55
Figure 2. 17	Formation of the Ru ^{III} -O [•] species.....	56
Figure 2. 18	Proposed catalytic cycle for water oxidation by 2.24	57
Figure 2. 19	Computed bond distances for the first two oxidations of 2.24	59
Figure 2. 20	EPR spectrum (10 K) of 2.29 + 10 equiv Ce ⁴⁺	63
Figure 2. 21	EPR spectrum (77K) of 2.24 with increasing amounts of Ce ⁴⁺	64
Figure 2. 22	EPR spectrum (RT) 2.24 + 2 equiv Ce ⁴⁺ + 1 equiv DMPO.....	65
Figure 2. 23	Simulated spectrum of DMPO=O	65
Figure 2. 24	A plausible mechanism for the formation of DMPO=O by 2.24	66
Figure 2. 25	Proposed synthesis for cyclometallating analog of 2.6	69
Figure 2. 26	Proposed synthesis for carbene analog of 2.6	70
Figure 3. 1	A double Clark electrode system.....	119
Figure 3. 2	An early attempt at cell design	120
Figure 3. 3	The revised cell maintained pressurization	121
Figure 3. 4	LabView interface created by Colton Breyer	122

Figure 3. 5	Water droplets cause errors	123
Figure 3. 6	Schematic of pressure cell used in this study.....	124
Figure 3. 7	Piping and instrumentation diagram (P&ID)	125
Figure 3. 8	Panel (front) of automated headspace sampling panel	126
Figure 3. 9	Panel (back) of automated headspace sampling panel.....	127
Figure 3. 10	Cutout diagram of automated headspace sampling panel	128
Figure 3. 11	Front of completed panel.....	129
Figure 3. 12	Completed setup with manual control gas manifold	130
Figure 3. 13	Closeup of completed bulk electrolysis cell with process fittings.....	131
Figure 3. 14	Schematic of bulk electrolysis cell.....	132
Figure 3. 15	Schematic of bulk electrolysis cell.....	133

LIST OF TABLES

Table 1. 1	Years remaining of fossil fuels in two models.....	2
Table 2. 1	Comparison of redox couples of 2.11 and 2.12	36
Table 2. 2	Improvements upon the [(terpy)(bipy)Ru(OH ₂)] ²⁺ platform	37
Table 2. 3	Comparison of catalytic performance and durability.....	48
Table 2. 4	2D NMR data for 2.17	79
Table 2. 5	2D NMR data for 2.21	81
Table 2. 6	2D NMR data for 2.22	83
Table 2. 7	2D NMR data for 2.24	85
Table 2. 8	Crystallographic information for 2.21-BARF	87
Table 2. 9	Atomic coordinates and equivalent isotropic displacement parameters for 2.21-BARF	88
Table 2. 10	Bond lengths [Å] for 2.21-BARF	91
Table 2. 11	Bond angles [°] for 2.21-BARF	94
Table 2. 12	Anisotropic displacement parameters for 2.21-BARF	98
Table 2. 13	Hydrogen coordinates and isotropic displacement parameters for 2.21-BARF	101
Table 2. 14	Crystallographic information for 2.24-OTf	102
Table 2. 15	Atomic coordinates and equivalent isotropic displacement parameters for 2.24	103
Table 2. 16	Bond lengths [Å] for 2.24-OTf	105
Table 2. 17	Bond lengths angles [°] for 2.24-OTf	107
Table 2. 18	Anisotropic displacement parameters for 2.24-OTf	111
Table 2. 19	Hydrogen coordinates and isotropic displacement parameters for 2.24-OTf	112

ACKNOWLEDGEMENTS

I write these acknowledgements with relief and appreciation for the many people who have helped make my PhD studies a success.

I must first sincerely thank my advisor, Prof. Douglas Grotjahn. His equanimity, work ethic, and optimism are inspiring. I respect him immensely as a synthetic chemist and am grateful to have been his student. When laboratory challenges seemed insurmountable Doug reminded me to “keep the faith”. I can say now at the end that faith manages.

There are a few individuals I wish acknowledge with whom I worked closely especially in the last two years of my studies. Brett Vincenzini joined the lab as a sophomore and has become an excellent synthetic chemist and electrochemist. Under my instruction Brett first prepared and characterized the sulfonate catalyst that became the foundation of the work described in this dissertation. I admire his intelligence, diligence, and enthusiasm and have no doubt he will excel in graduate school and beyond. I also wish to thank my graduate student colleague Colton Breyer. Colton developed the code for the pressure testing cell, collaborated with me on the design of all instrumentation in chapter 3, and ran the oxygen evolution experiments. I could not have completed this work without Colton and am grateful to call him a colleague and a friend. Braden Silva provided his keen insight and many useful discussions over the years, kept the large ship that is our lab on course, and is a true DudeBerry. I also wish to especially thank Profs. Arnold Rheingold, Roland Wolkowicz, and Gilbert Valadez for their mentorship and guidance throughout my studies.

I thank the rest of my lab mates and fellow graduate students with whom I have worked over the years: in particular I wish to thank Drs. Jayneil Kamdar, Erik Paulson, Nobuyuki Yamamoto and Caline Abidjian for their support and advice especially near the end of my PhD studies.

I thank Prof. Diane Smith for the provision of potentiostats, instruction, patience, and good humor during the electrochemical characterization of the compounds described in chapter 2. Prof. Dale Chatfield provided consultation on the design of the automated headspace sampling system described in chapter 3 as well as expert GC/MS support and is gratefully acknowledged. I thank Prof. Arnold Rheingold for solving all the solid-state structures described in chapter 2.

Chapter 2 contains material that is currently being prepared for publication. Nash, A.G.; Breyer, C.J.; Vincenzini, B.D.; Elliott, G.; Smith, D.K; Rheingold, A.L.; Musaev, D.; Grotjahn, D.B. "A Fast and Durable Ruthenium-Based Water Oxidation Catalyst with a Sulfonate Moiety in the Active Site". *Manuscript in Preparation*. The dissertation author was the primary researcher for the data presented. I thank Colton Breyer for performing manometry and voltammetry experiments. Brett Vincenzini performed the initial syntheses of the sulfonate and phosphonate complexes under the instruction of the dissertation author and is gratefully acknowledged. I thank Prof. Diane Smith for providing equipment, consultation and advice on all voltammetry experiments. I thank Dr. Gregory Elliot for performing high resolution mass spectrometry experiments. I thank Prof. Arnold Rheingold who provided x-ray crystallography support and solved all structures presented in this work. Graduate student Justin Lee and Prof. Andrew Borovik of the University of California Irvine provided access to EPR instrumentation

that is gratefully acknowledged. I thank Prof. Jamal Musaev of the Cherry L. Emerson Center for Scientific Computing at Emory University for performing detailed calculations from which we developed our tentative mechanism. Financial support for all work in this publication was provided the US Department of Energy (grant no. DE-SC0018310) and is gratefully acknowledged.

VITA

2006-2009	Bachelor of Science, Chemistry, Miami University Bachelor of Arts, Philosophy, Miami University
2009-2016	Teaching Assistant, San Diego State University
2009-2019	Graduate Researcher, San Diego State University
2009-2014	Master of Arts, Chemistry, San Diego State University
2012-2019	Doctor of Philosophy, Chemistry, University of California San Diego and San Diego State University

Manuscripts in Preparation

1. Nash, A.G.; Breyer, C.J.; Vincenzini, B.D.; Elliott, G.; Smith, D.K.; Rheingold, A.L.; Musaev, D.; Grotjahn, D.B. "A Fast and Durable Ruthenium-Based Water Oxidation Catalyst with a Sulfonate Moiety in the Active Site"
2. Williams, N.; Nash, A.G.; Yamamoto, N.; Patrick, M.; Tran, I.; Gu, J. "Unraveling Activity and Decomposition Pathways of [FeFe] Hydrogenase Mimics Covalently Bonded to Silicon Photoelectrodes"

Presentations (*presented by underlined author*)

1. "Heteroatom pendant bases for ruthenium catalyzed water oxidation," B.D. Vincenzini, A.G. Nash, C.J. Breyer, B.E. Silva, D.B. Grotjahn, poster presentation at the 258th National Meeting of the American Chemical Society, San Diego, CA, August 2019, abstract #: INOR 0146
2. "Strongly σ -donating ligands with pendant bases for water oxidation catalysis" A.G. Nash, B.D. Vincenzini, C.J. Breyer, B.E. Silva, D.B. Grotjahn, oral presentation at the 258th National Meeting of the American Chemical Society, San Diego, CA, August 2019, abstract #: INOR 0740
3. "Ligands possessing C- and N-donors for ruthenium catalyzed water oxidation: Synthesis, characterization, and electrochemistry" A.G. Nash, D.B. Grotjahn, oral presentation at the 251st National Meeting of the American Chemical Society, San Diego, CA, March 2016, abstract #: INOR 1392

Honors and Awards

Hologic Science and Technology Scholarship (2017)

Major Fields of Study

Major Field: Chemistry (Organic)

Studies in Synthesis and Organometallic Catalysis
Professor Douglas B. Grotjahn

ABSTRACT OF THE DISSERTATION

Water Oxidation Catalysts with Heteroatom Pendant Bases and
Instrumentation for Quantifying Oxygen

by

Aaron Gabriel Nash

Doctor of Philosophy in Chemistry

University of California San Diego, 2019

San Diego State University, 2019

Professor Douglas B. Grotjahn, Chair

Avid consumption of fossil fuels by humans has led to record high levels of the greenhouse gas carbon dioxide (CO_2). An energy storage medium to replace dwindling and finite fossil fuel supplies must be found. Hydrogen gas (H_2) is an attractive alternative to hydrocarbon fuels but presently natural gas is the primary feedstock for H_2 production globally. Therefore, an alternative process for hydrogen production must be developed. Photoelectrochemical electrolysis of water (H_2O) presents a promising method for the clean generation of H_2 . The oxidation of water to oxygen (O_2), four protons (H^+), and four electrons (e^-) must precede the reduction of H^+ to H_2 and is the more demanding reaction both kinetically and thermodynamically. Transition metal catalysis can realize this challenging transformation. Careful choice of metal and ligand

design can facilitate each stage of the oxidation of water; in particular, the management of H^+ during catalysis can help improve both the speed and the durability of the catalyst. This dissertation describes the synthesis, characterization, and water oxidation activity of two new water oxidation catalysts featuring heteroatom H^+ relays and the development of instrumentation to better quantify the O_2 produced during H_2O oxidation.

Chapter 2 describes the incorporation of phosphonate monoester and sulfonate and pendant bases into the first coordination sphere of the well-studied water oxidation platform $[(2,2';6',2''\text{-terpyridine})(2,2'\text{-bipyridine})Ru(OH_2)]^{2+}$. The complexes were characterized by combustion analysis, NMR spectroscopy, and x-ray crystallography. The catalytic performance of the complexes was evaluated for water oxidation catalysis using ceric ammonium nitrate (CAN) as a sacrificial oxidant *via* manometry and by square wave and cyclic voltammetry in a buffered aqueous milieu. The phosphonate monoester was found to perform poorly under chemical oxidation conditions but did show electrocatalytic behavior by cyclic voltammetry. The sulfonate system performed very well with CAN as the oxidant demonstrating a turnover frequency of 0.88 s^{-1} and turnover number of 7402. The sulfonate system also demonstrated electrocatalytic behavior suggesting homogenous electrocatalysis is maintained. Pourbaix analysis and a computational study suggest the intermediacy of a unprecedented ruthenium (III) oxyl, with the sulfonate acting as a pendant base late in the catalytic cycle.

Chapter 3 describes the development of two pieces of instrumentation for the detection of oxygen produced by our water oxidation catalysts. The first instrument is a dual manometry/optical oxygen sensing cell which was constructed for evaluating catalyst performance. Problems with the fluorescent oxygen sensor including drift and

sensitivity to humidity led us to focus on pressure as the primary indication of oxygen production. The cell is a robust and easy to use system that provides excellent repeatability and reliability, with <2% drift at more than twice typical operating pressure over 60 h. The second piece of instrumentation was an automated system for sampling headspace gas in a bulk electrolysis (BE) cell. The design and construction of a panel that interfaces a custom BE cell, potentiostat, and gas chromatograph/mass spectrometer (GC/MS) is described.

Chapter 1 – A Renewable Energy Cycle from Water

1.1 Depletion of Fossil Fuels

Fossil fuels represent 81% of the world's total primary energy supply as of 2017. Human activity has resulted in the consumption of 1 trillion barrels of oil in the last 140 years. Presently the world's demand for energy amounts to the consumption of over 1000 barrels of oil, 100000 cubic meters of natural gas and 244 tons of coal *per second*¹. Such avid consumption of these resources will lead to several significant problems for humans.

The first and most obvious problem is the limited supply: fossil fuels are a finite resource that will eventually be depleted. A coordinated shift from fossil fuel to renewable energy resources seems unlikely. There are myriad reasons for this, but one particularly compelling reason is the so called “the tragedy of the commons”. This phenomenon was first described by English economist William Forster Lloyd and developed in an essay in *Science* by Garrett Hardin². It describes the diffusion of responsibility for management of a shared and limited resource that inevitably leads to its exhaustion. A corollary of this is contamination of a shared resource, wherein no collective action is taken to safeguard its continued viability. Unfortunately, global consensus on reduction or elimination of fossil fuel usage has as of this writing not been reached, with the US and China as primary holdouts. Finally, fossil fuels are not evenly distributed across the globe. The geographical gap between the heaviest consumers of these resources and the countries richest in them will inevitably lead to geopolitical conflict as fossil fuels become more scarce¹. It is worth mentioning here that scarcity is not merely an eschatological fantasy: one scenario envisaged in 2009 by Topal et al.

Table 1. 1 Years remaining of fossil fuels in two models ³

Model	Klass Model			Topal Model		
	oil	coal	gas	oil	Coal	gas
Years	34	106	70	35	107	37

predicts that coal reserves will be the only fossil fuel remaining after 2042, and even coal will be depleted by 2112. Though hydraulic fracturing has made available oil and natural gas reserves that were previously thought inaccessible⁴, these production techniques come with their own environmental hazards and simply defer the time until fossil fuels will be exhausted. In the meantime, oil and gas consumption will continue to rise, and so will the prices of these commodities. A less discussed but equally important factor is the effects on human health. In the US alone, approximately 200,000 premature deaths per year occur due to combustion emissions, with the leading sources being road transportation and power generation⁵. Globally, fossil-fuel-related emissions are estimated responsible for 65% of the excess mortality rate attributable to air pollution. Millions of lives could be saved if fossil fuels were rapidly phased out and replaced with emission and carbon neutral power sources⁶.

1.2 Global Warming

There is a much more insidious and catastrophic problem than the increasing scarcity of hydrocarbon fuels: global warming. Though it is currently fashionable to refer to this phenomenon as “climate change” the trend of global temperature over the past 40 years has been in one direction, namely upwards. Present scientific consensus is that alterations in climate are anthropogenic in origin. As human civilization has

expanded, so too has the amount of greenhouse gases increased. The most significant culprit is carbon dioxide (CO₂). The concentration of atmospheric CO₂ reached a record 407.4 ppm in 2018. Climate scientists estimate that global CO₂ levels were last this high over 3 million years ago⁷.

CO₂ during ice ages and warm periods for the past 800,000 years

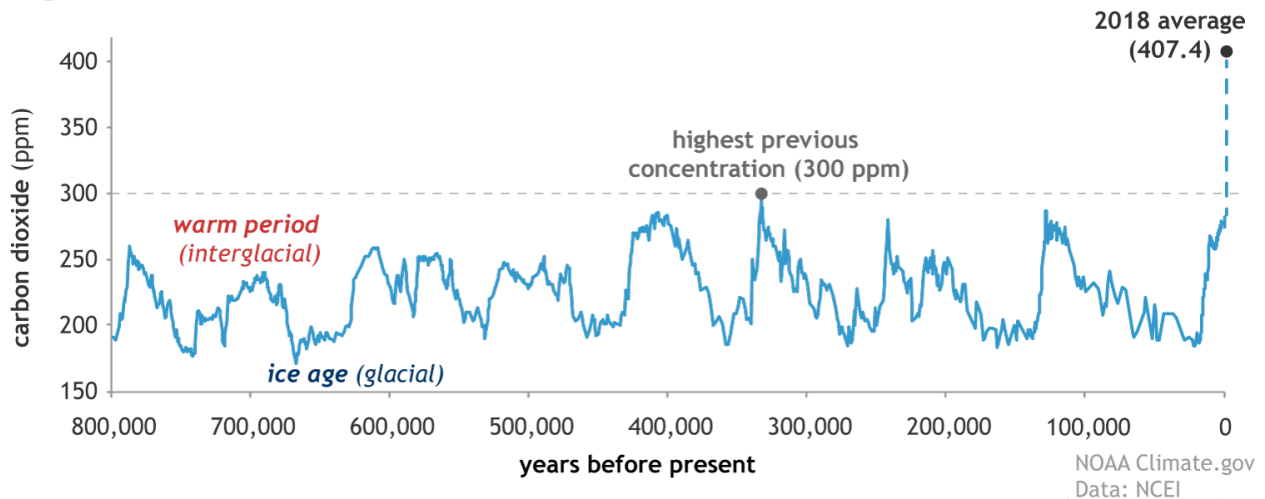


Figure 1. 1 Atmospheric carbon dioxide concentrations in parts per million (ppm) for the past 800,000 years, based on EPICA (ice core) data. The peaks and valleys in CO₂ levels track the coming and going of ice ages (low carbon dioxide) and warmer interglacials (higher levels). Throughout these cycles, atmospheric carbon dioxide was never higher than 300 ppm; in 2018, it reached 407.4 ppm (black dot)⁷.

In terms of global climate, rising CO₂ levels are accompanied by average global temperature approximately 2°–3°C higher than during the pre-industrial era when sea levels were 15–25 meters higher than present levels. More worryingly, the yearly rate of increase in atmospheric CO₂ over the past 60 years is approximately 100 times faster than previous natural increases, such as those that occurred at the end of the last ice age 11,000-17,000 years ago⁷.

None of the myriad effects of increasing average global temperature bode well for human civilization. The likelihood of extreme weather that adversely impact costal

enclaves will greatly increase⁸. Draught and serious impacts on food supply are also existential threats to human civilization. Tropical diseases will likely propagate as conditions for their proliferation become more widespread. Moreover, the effects are not restricted to those on land. The ocean has absorbed enough carbon dioxide to lower its pH by 0.1 units which corresponds to a 30% increase in acidity. Increasing ocean acidity affects the ability of marine life to extract calcium from ocean water, which can cause serious damage to marine ecosystems from the bottom up, disrupting the growth cycles of plankton that form the basis of oceanic food chains and disrupt fisheries that serve as critical food supplies⁹. Increasing ocean temperatures threaten coral reef biomes by increasing the occurrence of bleaching events. Some coral reef ecosystems have been so severely impacted it is not clear if they will ever fully recover from the damage⁷.

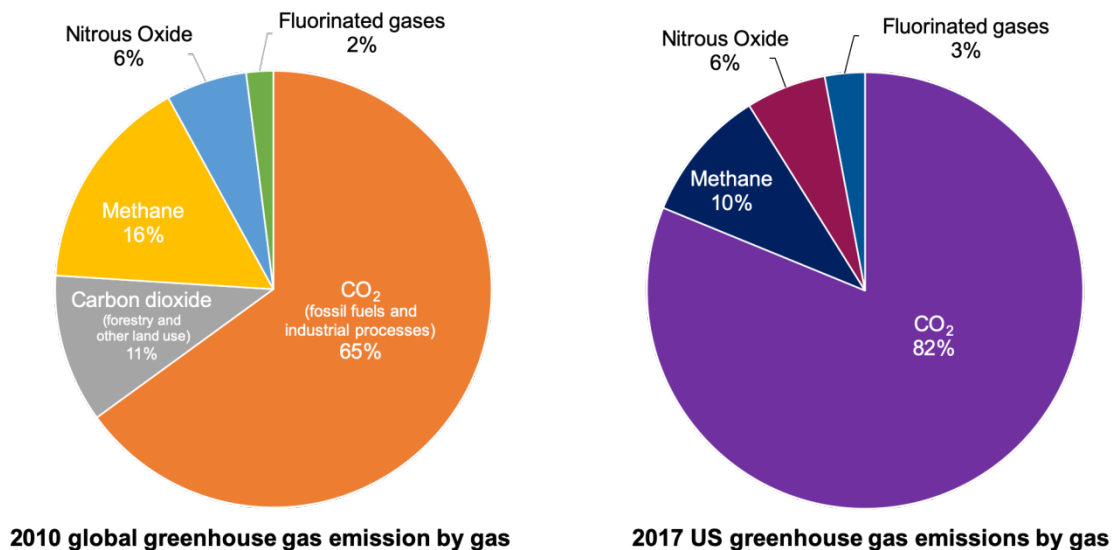


Figure 1.2 Greenhouse gas emissions by type. Global greenhouse gas distribution (2010)¹⁰ is indicated left, US greenhouse gas distribution (2017)¹¹ on the right. Of US greenhouse gas emissions, 76% of CO₂ comes from the burning of fossil fuels.

The primary driver for CO₂ production in the modern era is the burning of fossil fuels. Indeed, the total global output of CO₂ dwarfs that of other greenhouse gases. Data from 2010¹⁰ indicate that CO₂ derived from fossil fuel consumption and industrial processes represented 65% of global greenhouse gas emission. In the United States as of 2017¹¹, CO₂ represented 76% of total greenhouse gas emissions resulting from fossil fuel consumption and industrial output. Given the seriousness of the problem it is clear that a transition to renewable fuel sources is essential for the continued survival of human civilization and the maintenance of life as we know it on this planet.

1.3 Storing Energy from the Sun in Water

Proposal of alternatives to fossil fuel consumption was put forth even in the era of the industrial revolution. In the novel *The Mysterious Island* (1874), science fiction author Jules Verne speculated that:

water will one day be employed as a fuel, that hydrogen and oxygen that constitute it, used singly or together, will furnish an inexhaustible source of heat and light, of an intensity of which coal is not capable. Someday the coal rooms of steamers and the tenders of locomotives will, instead of coal, be stored with these two condensed gases, which will burn in the furnaces with enormous caloric power...I believe, that when the deposits of coal are exhausted, we shall heat and warm ourselves with water ...Water will be the coal of the future.¹²

Giacomo Ciamician, the father of modern photochemistry, took this idea even further. In 1912 he proclaimed:

...if in a distant future the supply of coal becomes completely exhausted, civilization will not be checked by that, for life and civilization will continue as long as the sun shines! If our black and nervous civilization, based on coal, shall be followed by a quieter civilization based on the utilization of solar energy that will not be harmful to progress and to human happiness.

The words of these men were visionary and indeed, energy storage in the form of hydrogen gas (H_2) is now a reality. However, there remain significant hurdles to the widespread implementation of hydrogen as a fuel. In order to understand why it is helpful to compare the chemical and physical properties of H_2 and hydrocarbon fuel sources and their respective production methods.

Liquid H_2 has an energy density of 8 MJ/L whereas gasoline has an energy density of 32 MJ/L, as shown in the figure below. H_2 is a gas at room temperature, but must be compressed to very high pressures (5000-10000 psi = 350-700 bar) in order for its storage to be practical for an application like on-board vehicular use. However, once compressed the physical and chemical properties of H_2 compare favorably to those of liquid hydrocarbons¹³.

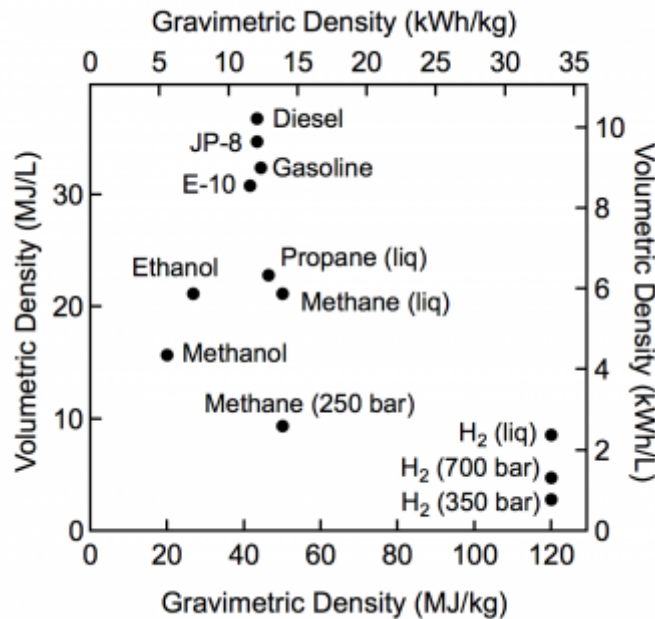


Figure 1.3 Comparison of volumetric and gravimetric density of fossil fuels and H_2 gas. H_2 has almost three times the gravimetric energy density of gasoline¹³.

H₂ contains 2.8x the energy content of gasoline on a mass basis —120 MJ/kg for hydrogen compared to 44 MJ/kg for gasoline. For an application such as onboard vehicular use 5–13 kg of hydrogen is required for the typical driving range of a light-duty vehicle¹³. Furthermore, the only products of H₂ oxidation are energy and water:



The storage technology necessary has already been commercialized by several automobile manufacturers: the Toyota Mirai Fuel Cell Vehicle surpassed sales of 3000 in California by the end of 2018¹⁴, and there are currently 41 H₂ fueling stations throughout the state¹⁵.

The problem now is production: 96% of H₂ produced today comes from non-renewable sources¹⁶. The total market value is expected to reach \$154.7 billion by 2022¹⁷. Most of that H₂ finds use in the petrochemical, fine chemical, and electronics industries.

Today most H₂ gas is produced by a process called steam reforming with the typical feedstock being methane from the natural gas industry. In this process the methane is reacted with water between 450-950 °C at 20-30 atm over a nickel catalyst yielding H₂ and carbon monoxide (CO). A second reaction known as the water gas shift converts the CO to CO₂ and yields a further equivalent of H₂. The final balance is one equivalent of CO₂ and four equivalents of H₂¹⁸.





A non-fossil fuel source of H_2 is water itself, wherein the water is electrolyzed to produce hydrogen and oxygen gases. At present only 4% of global H_2 is produced from electrolysis¹⁶.

For a H_2 fuel cycle to be renewable the primary energy input must also come from a renewable source. Fortunately, there is a nearly endless source of energy constantly supplying the Earth an average of over 1300 W/m^2 of power: the sun¹⁹. Coupling the oxidation of water to a photovoltaic cell would be the ideal solution.

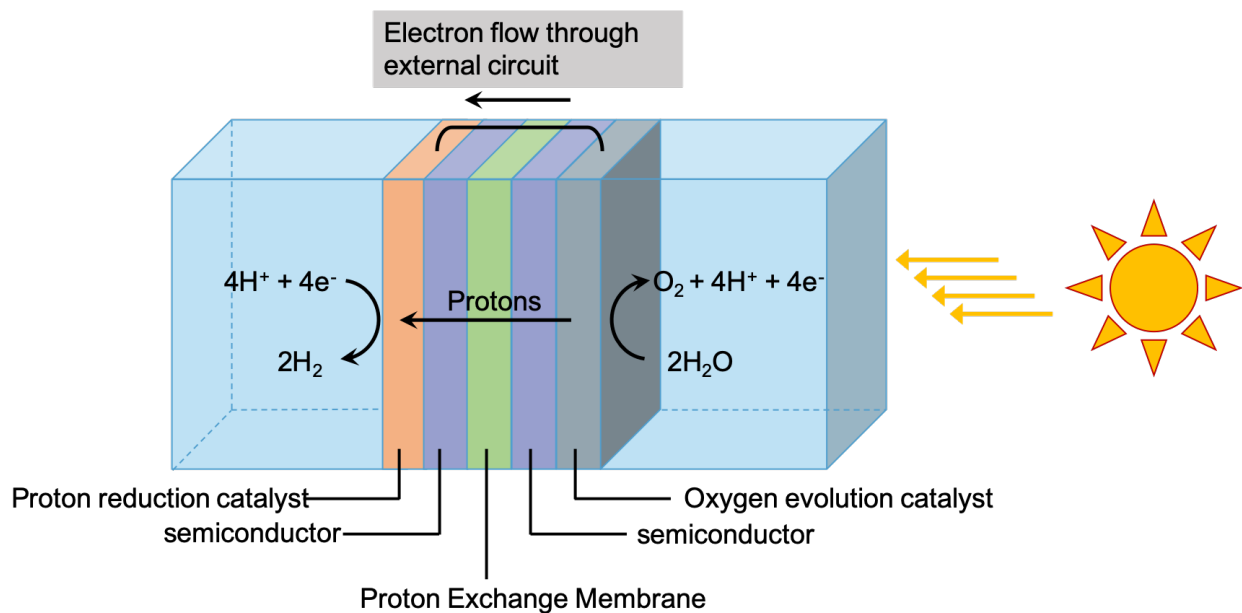
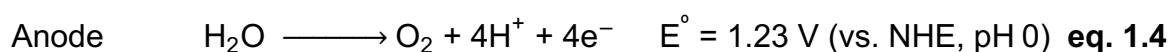


Figure 1.4 Schematic of a photoelectrochemical cell. A typical proton exchange membrane is a material like Nafion™ (adapted from ref. 20).

In the system portrayed in Figure 1.4, sunlight provides the necessary energy to a semiconductor interfaced to a water oxidation catalyst. The catalyst effects the anodic

reaction in which two molecules of water are oxidized to oxygen, four protons, and four electrons. The protons are conveyed to the other compartment *via* proton exchange membrane where they are reduced at a different catalyst/semiconductor assembly to two molecules of hydrogen. Of these two reactions, the anodic part is both thermodynamically and kinetically more demanding, requiring the breaking of four bonds and the making of a double bond.



The standard potential of each half reaction varies with the Nernst equation ($\Delta E = 0.059 \text{ V/pH unit}$) but the thermodynamic difference will remain $\Delta E = 1.23 \text{ V}$. This equates to $+475 \text{ kJ/mol O}_2$, which is a quite endothermic reaction. In practice, the energetic requirement of catalyzed water oxidation will always be higher than the thermodynamic requirement alone the reasons for which are discussed in the next section.

1.4 Electrocatalysis – A review

Energy in excess of the energetic difference between reactant(s) and product(s) is always required to affect a chemical transformation. The additional energy is required to organize the reactant(s) into a configuration that will result in product formation, and the amount of energy required to reach a productive configuration of substrate is called the activation energy (E_a). As a reacting substrate undergoes its transition to product it

will reach a configuration of maximum energy referred to as the free energy of the transition state (ΔG^\ddagger). A catalyst can help minimize ΔG^\ddagger and thus facilitate a chemical reaction by replacing a single or small number of high energy transition states with a larger number of low energy transition states. When driven by an electrode, a catalyst participating in this type of transformation is referred to as an electrocatalyst. In the electrocatalytic context ΔG^\ddagger can be analogized to overpotential (η): the difference between the potential applied at the electrode (V_{applied}) and the thermodynamic potential of the reaction being catalyzed ($E^\circ_{\text{P/S}}$, the thermodynamic difference between product and substrate).

$$\eta = V_{\text{applied}} - E^\circ(\text{P/S}) \quad \text{eq. 1.6}$$

If the catalyst and reactant(s) are in the same phase, the catalyst is termed a homogenous electrocatalyst, whereas if the catalyst is in a different phase (typically immobilized on the electrode surface) it is termed a heterogenous electrocatalyst. A good electrocatalyst can minimize η by facilitating electron transfer between the electrode, solution, and reactants, as well as facilitating chemical transformations directly. In the case of water oxidation that entails stabilizing (but not too much, otherwise catalysis stops) reactive metal-oxygen transition states and managing protons during the course of catalysis, it is helpful to keep in mind that in pH 7 water $E^\circ_{\text{P/S}} = 0.82$ V.

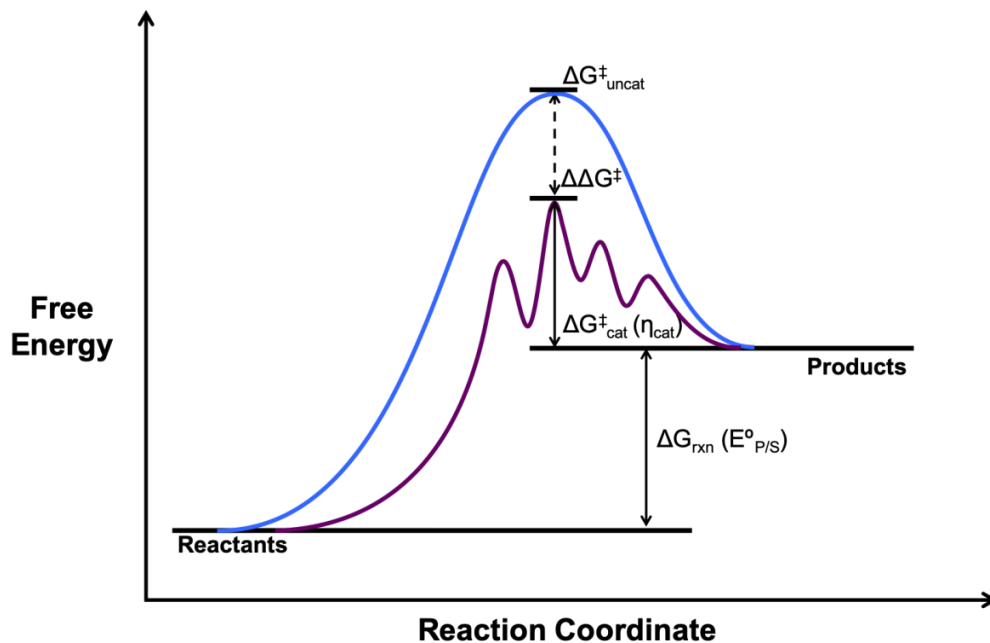


Figure 1.5 Free energy diagram for an endothermic reaction illustrating the different energy profiles of catalyzed and uncatalyzed reactions. Note that the free energy difference between reactants and products remains the same between conditions. In the catalyzed case however the free energy of the highest energy transition state is much lower than in the uncatalyzed case.

In an endothermic reaction like the one diagrammed above the catalyst requires an input of energy as the products are higher in energy than the reactants. This energy can be delivered by either chemical or electrochemical oxidizing equivalents.

The first scenario requires a reservoir of chemical oxidant that is depleted over the course of reaction, which can be very useful when testing catalytic performance as one can vary the amount of sacrificial oxidant to obtain mechanistic information about a catalyst. A typical sacrificial oxidant used in testing of water oxidation catalysts is ceric ammonium nitrate (CAN, $E^{\circ} = 1.61 \text{ V vs. NHE}, 1.41 \text{ V vs. Ag/AgCl}$). As a practical matter, the constant resupply of a sacrificial oxidant is unrealistic for use in large scale water electrolysis systems.

An electrode can also be used to oxidize the catalyst to its activated form. The electrode is held at a potential to repeatedly re-oxidize the catalyst as it returns to its resting state. An external power source provides the necessary potential difference and can be calibrated close to the η required for the reaction.

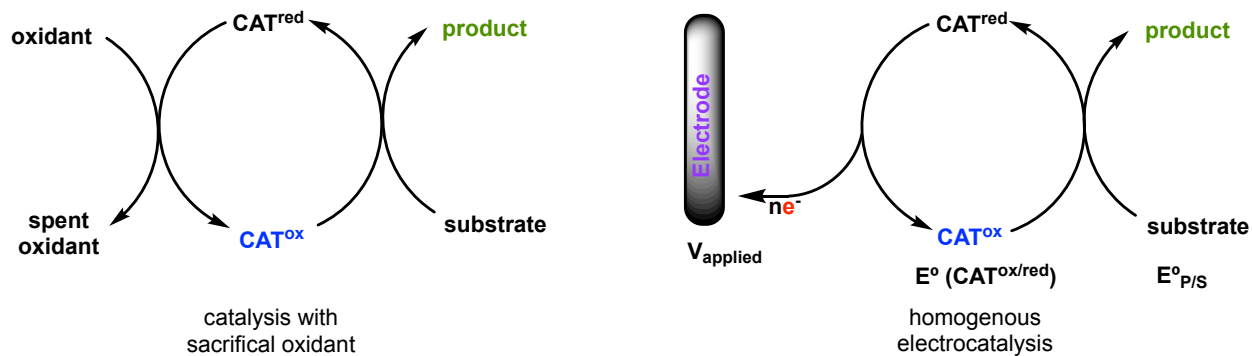


Figure 1. 6 Comparison of catalysis with a sacrificial oxidant versus electrocatalysis. Note that in the sacrificial oxidant case, catalysis will proceed until the sacrificial oxidant is depleted, whereas in the case of electrocatalysis, as long as fixed potential is applied at the electrode, catalysis will continue. In both cases, the catalyst can degrade with time.

An outstanding example of photoelectrochemical H_2O oxidation already exists in Nature, realized in the form of solar powered oxygenic photosynthesis. Photosystem II and its oxygen evolving complex (OEC) make these transformations possible and are discussed in the next section.

1.5 Photosystem II – Nature’s Water Oxidation Catalyst

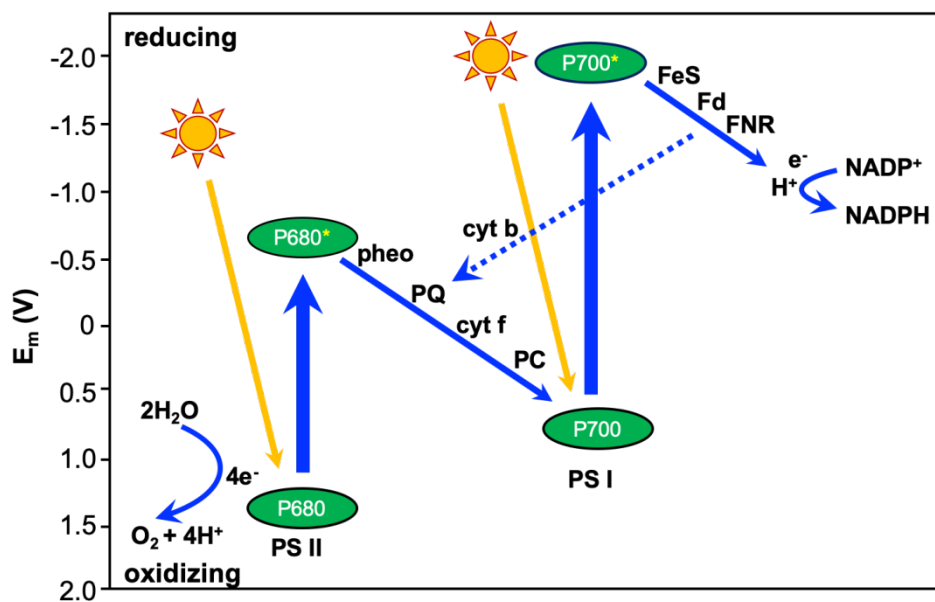


Figure 1.7 “Z-scheme” depicting the electron transport chain of the light cycle of photosynthesis. The process begins with water oxidation by photosystem II, with exciton conveyed through the electron transport chain and ultimately reducing NADP^+ (adapted from ref. 21).

Water oxidation is the first link in the electron transport chain that ultimately generates reducing equivalents for CO_2 fixation, an elegant union of opposite chemical processes that makes life on Earth possible. The process begins with the absorption of a red photon by a pair of special pair of chlorophyll molecules embedded in photosystem II/P680 generating an exciton. The electron is moved into the electron transport chain where it will ultimately reduce NADP^+ to NADPH. The hole is very oxidizing at $\sim 1.3 \text{ V}^{22}$, and ultimately oxidizes a tyrosine residue (TyrZ) adjacent the active site of the enzyme. The now redox-active tyrosyl radical cation mediates proton coupled electron transfer (PCET) at the oxygen evolving complex (OEC).

The OEC is the active site of Photosystem II and contains a cluster of the formula $Mn_4CaO_5(H_2O)_4$. Three manganese and one calcium ions are organized in a cubane-like motif. The other manganese is outside the cubane nearest the calcium. The cluster is stabilized by several basic amino acid residues as well as structural waters. An intricate network of structural waters and aspartate outside the first coordination sphere of the cluster helps convey protons away from the active site as the catalysis proceeds^{23,24}.

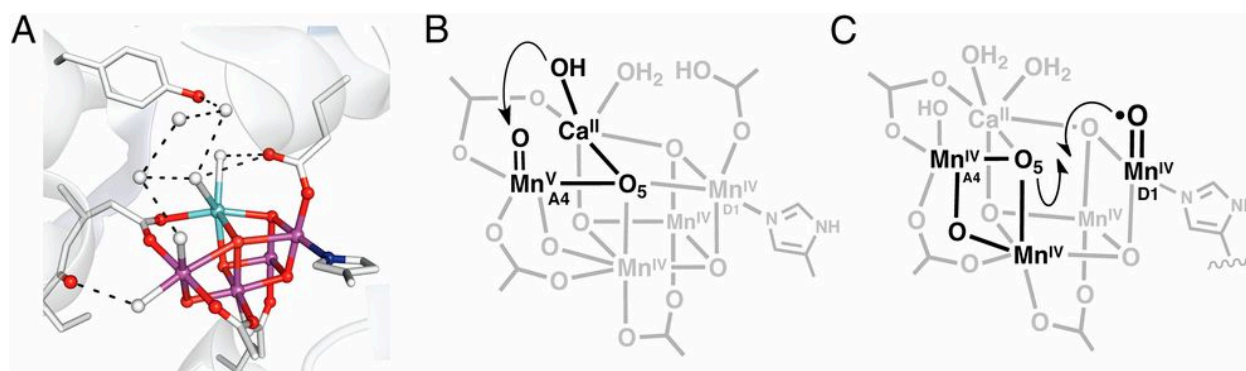


Figure 1. 8 (A) X-ray structure of the oxygen evolving complex; (B) scheme depicting attack of a bound hydroxide on a manganese oxo; (C) scheme depicting radical coupling of a manganese terminal oxo and a structural oxygen (figure from ref. 25).

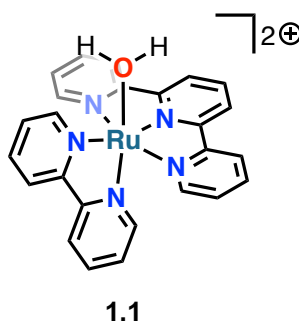
There is considerable debate in the literature in terms of the oxygen formation mechanism. There are two contending proposals for the oxygen-oxygen bond forming step. The first envisions a water attacking an electrophilic $Mn=O$ moiety. This is termed the acid/base or water nucleophilic attack mechanism (WNA). The other mechanism is a radical coupling of a terminal manganese oxo reaction with a structural oxygen to effect $O-O$ bond formation, often referred to as radical oxo coupling (I2M).

Contemporary evidence favors the oxyl/oxo coupling mechanism as depicted in figure **1.8c**²⁶.

Photosystem II is exceptionally fast at generating oxygen with turnover frequencies in excess of 100 s^{-1} ²⁷ and turnover numbers of approximately 600,000²⁸, all at overpotentials of approximately 70 mV²⁷. Any artificial system should be benchmarked against this performance.

1.6 A Brief History of [(terpy)(bipy)Ru(OH₂)]²⁺

The quest to develop a synthetic molecular H₂O oxidation catalyst has been a challenging one^{29–32}. Intense efforts by research groups worldwide have realized many successes. One of the most well studied platforms is the mononuclear system [(2,2':6',2''-terpyridine)(2,2'-bipyridine)Ru(OH₂)]²⁺ (**1.1**) which is the foundation of the work in this dissertation.



The first report of **1.1** came in 1963 from a report by F. Dwyer, H.A. Goodwin, and E.C. Gyarfar³³ in the *Australian Journal of Chemistry*. The authors remarked on the stability of the parent cation [(terpy)(bipy)Ru(Cl)]²⁺ and its amenability for ligand substitution. Rather presciently, they noted:

“Because, in effect, five coordination positions are tied off in these bipyridine-terpyridine chelates, which are reversibly oxidizable and

reduceable, they should be valuable substances for kinetic studies of substitution."³³

17 years later Moyer and Meyer³⁴ reported on the redox activity of this complex, noting that it readily underwent a $2e^-/2H^+$ process to form a ruthenium oxo species. They chose **1.1** in particular because their attempts with $[(bipy)_2(py)Ru(H_2O)]^{2+}$ system revealed an unacceptably high kinetic instability, specifically the formation of what they inferred to be $[(bpy)_2(H_2O)Ru-(\mu_2-O)-Ru(py)(bpy)_2]^{4+}$. The focus of their work was the oxidation of organic substrates, and the catalyst system was not driven to potentials high enough to affect the oxidation of water. However, in 1984 Takeuchi and Meyer³⁵ reported further on the redox chemistry of **1.1** system including a full Pourbaix diagram. Their results indicated that the oxo formed after undergoing two discrete PCET events:

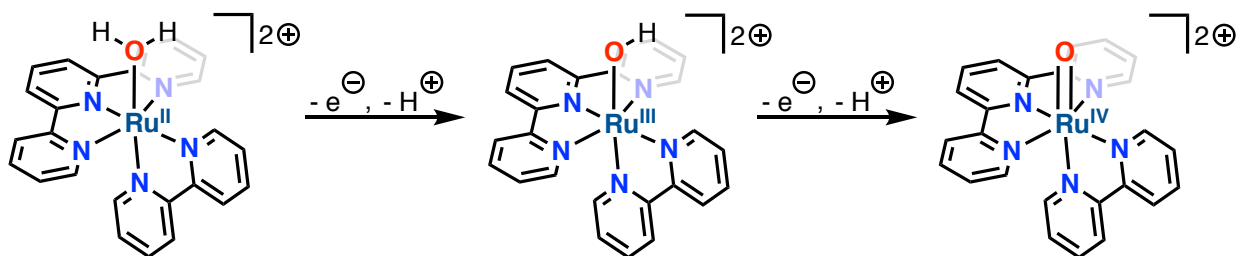
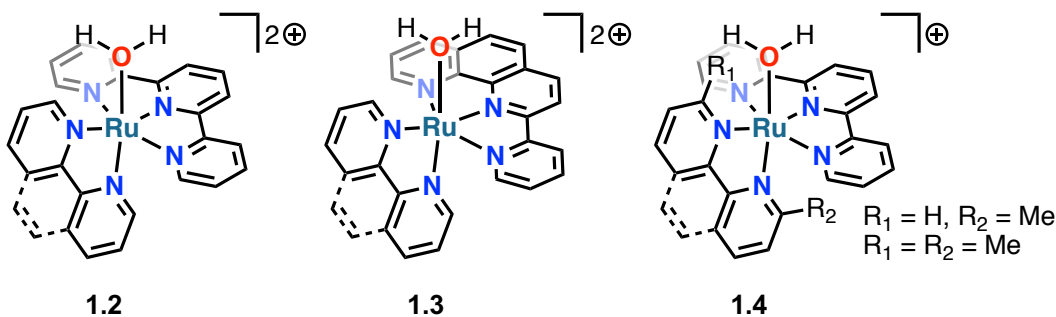


Figure 1.9 Meyer's proposed mechanism for the formation of a $Ru^{IV}=O$ moiety by two PCET events. Note that the charge of the complex remains the same even as the ruthenium center is oxidized by two electrons (adapted from ref. 35)

The first reports of water oxidation by **1.1** would not arrive until 2008. At that time, a series of seminal publications by the groups of Thomas Meyer, Kenji Sakai, and Randolph Thummel reignited interest in the family of molecules related to **1.1**. Nearly simultaneously, Thummel³⁶ and Sakai³⁷ published works revealing the water oxidation activity of **1.1**. The chemical oxidant ceric ammonium nitrate (CAN) was used as a sacrificial oxidant in both studies, which represented a departure from previous studies in which only electrochemistry was reported.



Thummel's work focused on building a library of complexes with ligands of different denticities and discerning structure-activity relationships therefrom^{36,38} (members of the library such as **1.2-1.4** above are similar to **1.1**). They found that complexes possessing two tridentate ligands were inactive for H₂O oxidation, and those with multiple monodentate ligands such as 4-picoline tended to perform worse than those with one tridentate ligand and one bidentate ligand, with the remaining site occupied by a labile ligand such as water.

Sakai's work was oriented toward characterization and mechanistic studies. His group reported that the observed reaction rate was first order in catalyst³⁵. They ruled out a radical oxo coupling mechanism based on this finding, but it is worth noting that the rate determining step could be formation of an oxo following a rate law $r = k [\text{cat}][\text{Ce}^{\text{IV}}]$, followed by radical oxo coupling. Sakai's group also found that complexes with a Cl⁻ ligand instead of H₂O exhibited an induction period and the addition of NaCl suppressed catalysis. Mass spectrometric studies were used to establish the robustness of the catalyst.

Meyer's group presented an even more detailed mechanistic proposal based on extensive electrochemical experiments and UV-visible spectroscopy³⁹. They used two different bidentate ligands in place of 2,2'-bipyridine: bipyrimidine and bipyrazine. A

Pourbaix diagram described a $2e^-/2H^+$ redox process from pH 0 to pH 9.7. In the acidic region from pH 0-3 there is a pH independent $1e^-$ event assignable to $Ru^{IV}=O/Ru^V=O$ oxidation; this event coincides with the onset of a catalytic wave in the cyclic voltammetry suggesting that $Ru^V=O$ is the catalytically competent species. The authors also identify two high-valent ruthenium species in the UV-visible spectrum: a $Ru^{IV}-OO$ and a $Ru^V=O$ species. They infer that the $Ru^V=O$ is the critical intermediate which is attacked by H_2O .

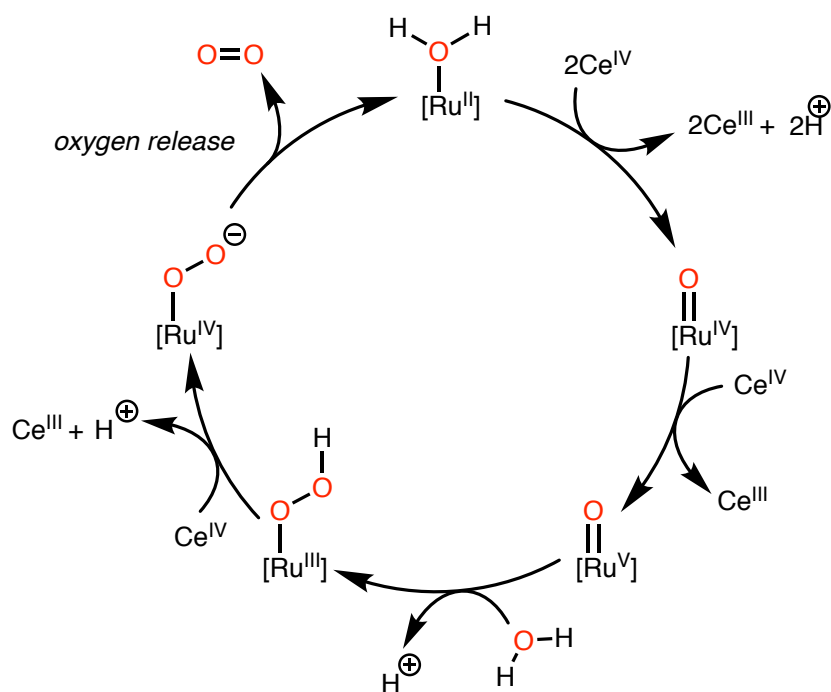
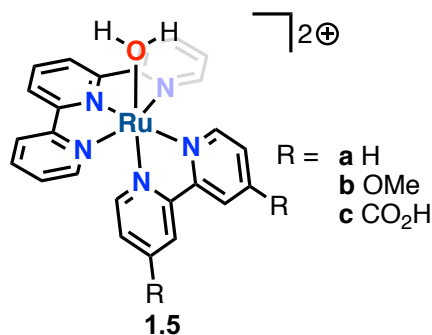


Figure 1. 10 Meyer's proposed mechanism for water oxidation by $[(\text{terpyridine})(LL)Ru(OH_2)]^{2+}$. Note the initial $2e^-/2H^+$ PCET steps, and the invocation of the high valent and electrophilic $Ru^V=O$ moiety.

Berlinguette's group explored structure-activity relationships by modifying the electronics of the bidentate ligand. Their paper in 2010⁴⁰ further elucidated the mechanism of this family of catalysts with an elegant mixture of structure activity

relationships and detailed kinetic studies. To that end, they synthesized a series of three structurally analogous catalysts of the form $[\text{Ru}(\text{terpy})(2,2'\text{-bipy-4,4'-R})(\text{H}_2\text{O})]^{2+}$ (where $\text{R} = \text{H}, \text{OMe}, \text{and CO}_2\text{H}$). As with the initial studies performed by Meyer's group, they inferred from cyclic voltammetry studies that the catalyst is oxidized by $3e^-$ to afford the active intermediate $\text{Ru}^{\text{V}}=\text{O}$.



The first event in their proposed catalytic cycle is described as an $1e^-$ oxidation to a $\text{Ru}^{\text{III}}\text{-OH}_2$ species, followed by a $1e^-/2\text{H}^+$ redox process to afford $\text{Ru}^{\text{IV}}=\text{O}$. This species is then oxidized to $\text{Ru}^{\text{V}}=\text{O}$, which is attacked by water. **1.5c** was found to be faster than the other two by stopped flow kinetic studies. In the cases of **1.5a** and **1.5c**, they determined the rate determining step to be release of oxygen from $\text{Ru}^{\text{IV}}\text{-O-O}$. The authors also performed detailed isotopic labeling studies which revealed that nitrate anions from the sacrificial oxidant can participate in O-atom transfer reactions to generate O_2 . Interestingly the authors suggest that the dimethoxy ligand of **1.5b** helped stabilize a higher oxidation state $\text{Ru}^{\text{V}}\text{-O-O}$. While release of dioxygen was thought to be faster at the formal oxidation state of V, the rate of formation of the Ru^{V} species was inferred to be comparatively slow and thus rate-determining.

There is some controversy about the invocation of very high oxidation states of ruthenium in the catalytic cycle, some of which was put to rest by 2014 in the

mechanism proposed by Pushkar et al.⁴¹ They studied **1.5a** using EPR, XANES, and EXAFS and used the data obtained to draw several conclusions that differed from Berlinguette's proposed mechanism. The first steps are like those in Berlinguette's proposal. The first oxidation gives a ruthenium(III) species without proton loss. The second oxidation proceeds with loss of two protons to generate a ruthenium(IV) oxo. Concomitant oxidant and H₂O nucleophilic attack and H⁺ loss generate a ruthenium(III) hydroperoxide. The hydroperoxide is again oxidized in a PCET step to generate a ruthenium(IV) peroxido that reductively eliminates O₂ and binds a H₂O to restart the catalytic cycle. The authors went to some length to consider other processes that invoke Ru(V) species during catalysis. The first is formation of a ruthenium(V) oxo from the ruthenium(IV) oxo. The other scenario is an alternative pathway to O₂ release. In this scheme, the ruthenium(IV) peroxido can undergo one electron oxidation to form a ruthenium(V) peroxide which reductively eliminates O₂ and binds H₂O to form the ruthenium(III) aquo.

The Pushkar group noted the absence of a detectable ruthenium(V) species with a variety of techniques in the primary catalytic cycle when excess CAN were used. Even in the presence of 20 equivalents of CAN the only detectable EPR signal was consistent with a ruthenium (III) hydroperoxide or silent, suggesting a Ru(IV) species. Moreover, XANES data was more consistent with a ruthenium(IV) oxo in terms of both the edge position and the calculated Ru—O bond distance from those data. Pushkar as well as Berlinguette offer a compelling reason to exclude Ru(V) in purely thermodynamic terms:

“Using the Ce^{III} /Ce^{IV} (1.45 V [vs. NHE]) and Ru^{IV}/Ru^V (1.80 V [vs. NHE]) one can derive the ratio of Ru^V to Ru^{IV} to be on the order of 10⁻⁶, which critically contradicts the results of [previous] kinetic modeling.”

Pushkar's group also collaborated with Meyer and analyzed several different water oxidation catalysts in an effort to detect a Ru(V)=O intermediate. No such entity was detected.

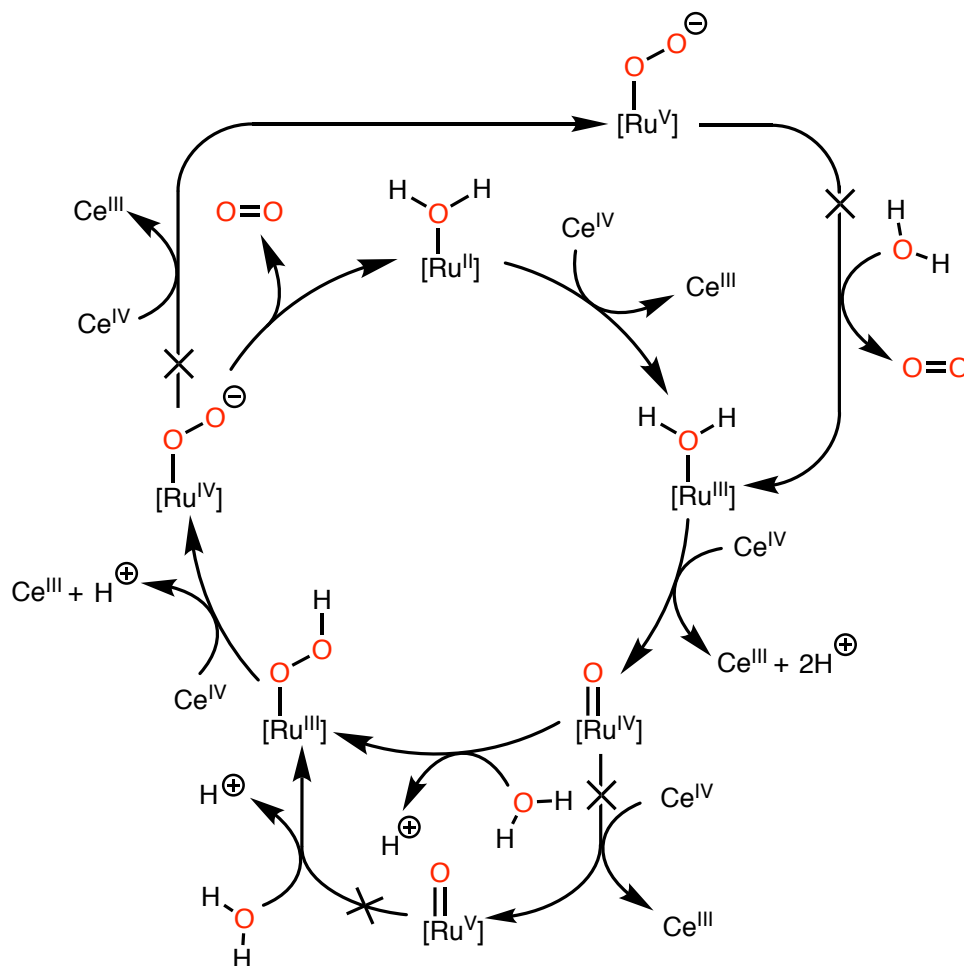


Figure 1.11 Pushkar's proposed mechanism for water oxidation by $[(\text{terpy})(\text{bipy})\text{Ru}(\text{OH}_2)]^{2+}$. Note that in the primary catalytic cycle the formal oxidation of the metal state does not exceed Ru(IV); Ru(V) species are excluded.

1.7 Designing a Better Water Oxidation Catalyst

At this point it is worthwhile to consider what can be done to improve the already well-studied 1.1 platform. Betley and coworkers^{42,43} published two papers laying out various design criteria for synthetic water oxidation complexes, basing their arguments

on ligand field theory considerations, noting how different symmetries can have profound effects on the nature of the M—O bond, and ultimately the operative mechanism of water. They paid specific attention to how d-electron count of the metal center affects the metal-oxygen bond order, noting that odd electron counts favor a radical coupling mechanism whereas even electron counts favor water nucleophilic attack. They also note that at a d^5 metal center, the metal-oxygen bond is diminished in π character due to population of metal d_{xz} and d_{yz} orbitals which are antibonding with respect to the M—O bond. These destabilizing effects complicate formation of a metal oxo bond in a tetragonal (C_{4v} pseudosymmetric) ligand field. More intriguingly, they note that “the issue of the extent of oxygen radical character at odd-electron metal-oxo centres has remained experimentally unresolved.” The following design criteria were thus put forth:

1. The active site of a water oxidation catalyst should permit control of the secondary coordination sphere to organize a water molecules as part of nascent O-O bond formation;
2. Electron and proton transfer steps should be coupled (PCET);
3. Water derived hydroxide should generate the metal oxo species.

All three design criteria invite the use of pendant bases strategically positioned near the metal-aquo moiety in order to both capture incoming water molecules and facilitate key proton transfer steps. However, it is also worth noting a comment by Nocera:

“Any practical catalysts for water oxidation will have to be stable and stand up to a highly active oxo core. It seems almost a paradox—the presence of a high-valent and reactive oxo in an environment rife with reducible moieties—i.e. the C—C and C—H bonds of a ligand framework.”

This statement is also surely true of a pendant base moiety close to the active site. Thus, further design criteria would include a pendant base that is oxidatively robust and can withstand close proximity to the highly oxidizing Ru=O fragment. These considerations were the lodestar for the study described in the next chapter and helped achieve improvements on prior catalysts, with indications of a novel mechanism of catalysis.

References

1. Armaroli, N.; Balzani, V. *Energy Environ. Sci.* **2011**, *4*, 3193.
2. Hardin, G. *Science* **1968**, *162*, 1243.
3. Shafiee, S.; Topal, E. *Energy Policy* **2009**, *37*, 181.
4. Gwyn, J. E. *Fuel Process. Technol.* **2001**, *70*, 27.
5. Caiazzo, F.; Ashok, A.; Waitz, I. A.; Yim, S. H. L.; Barrett, S. R. H. *Atmos. Environ.* **2013**, *79*, 198.
6. Lelieveld, J.; Klingmüller, K.; Pozzer, A.; Burnett, R. T.; Haines, A.; Ramanathan, V. *Proc. Natl. Acad. Sci.* **2019**, *116*, 7192.
7. Lindsay, R. Climate Change: Atmospheric Carbon Dioxide. *Clim. Change Atmospheric Carbon Dioxide*.
<https://www.climate.gov/newsfeatures/understanding-climate/climate-change-atmospheric-carbon-dioxide> (accessed October 17, 2019).
8. Special Report on the Ocean and Cryosphere in a Changing Climate — Special Report on the Ocean and Cryosphere in a Changing Climate.
<https://www.ipcc.ch/srocc/home/> (accessed November 9, 2019).
9. Free, C. M.; Thorson, J. T.; Pinsky, M. L.; Oken, K. L.; Wiedenmann, J.; Jensen, O.P. *Science* **2019**, *363*, 979.
10. US EPA, O. Global Greenhouse Gas Emissions Data. *US EPA*.
<https://www.epa.gov/ghgemissions/global-greenhouse-gas-emissions-data> (accessed November 3, 2019).
11. US EPA, O. Inventory of U.S. Greenhouse Gas Emissions and Sinks. *US EPA*.
<https://www.epa.gov/ghgemissions/inventory-us-greenhouse-gas-emissions-and-sinks> (accessed November 8, 2019).
12. Ryabchuk, V. K.; Kuznetsov, V. N.; Emeline, A. V.; Artem'ev, Y. M.; Kataeva, G. V.; Horikoshi, S.; Serpone, N. *Molecules* **2016**, *21*, 1.
13. Hydrogen Storage. *Energy.gov*. <https://www.energy.gov/eere/fuelcells/hydrogen-storage> (accessed November 8, 2019).
14. Hydrogen is Going the Distance: Toyota Surpasses 3,000 Mirai Hydrogen Fuel Cell Vehicle Sales in California. *Toyota USA Newsroom*.

- <https://pressroom.toyota.com/toyota-surpasses-3000-mirai-hydrogen-fuel-cell-vehicle-sales-in-california/> (accessed November 9, 2019).
15. Stations Map | California Fuel Cell Partnership. <https://cafcp.org/stationmap> (accessed November 9, 2019).
 16. Voldsund, M.; Jordal, K.; Anantharaman, R. *Int. J. Hydrog. Energy* **2016**, *41*, 4969.
 17. Hydrogen Generation Market by Application & Technology - Forecast 2023. <https://www.marketsandmarkets.com/Market-Reports/hydrogen-generation-market-494.html> (accessed November 9, 2019).
 18. Vozniuk, O.; Tanchoux, N.; Millet, J.-M.; Albonetti, S.; Di Renzo, F.; Cavani, F. In *Studies in Surface Science and Catalysis*; Albonetti, S.; Perathoner, S.; Quadrelli, E. A., Eds.; Horizons in Sustainable Industrial Chemistry and Catalysis; Elsevier, **2019**; Vol. 178, pp 281.
 19. Coddington, O.; Lean, J. L.; Pilewskie, P.; Snow, M.; Lindholm, D. *Bull. Am. Meteorol. Soc.* **2015**, *97*, 1265.
 20. Roger, I.; Shipman, M. A.; Symes, M. D. *Nat. Rev. Chem.* **2017**, *1*, 1.
 21. Light Reactions. http://plantphys.info/plant_physiology/lightrxn.shtml (accessed November 8, 2019).
 22. Nicholls, D. G.; Ferguson, S. J. In *Bioenergetics (Fourth Edition)*; Nicholls, D.G.; Ferguson, S. J., Eds.; Academic Press: Boston, **2013**; pp 159.
 23. Polander, B. C.; Barry, B. A. *Proc. Natl. Acad. Sci.* **2012**, *109*, 6112.
 24. Nagao, R.; Ueoka-Nakanishi, H.; Noguchi, T. *J. Biol. Chem.* **2017**, *292*, 20046.
 25. Gupta, R.; Taguchi, T.; Lassalle-Kaiser, B.; Bominaar, E. L.; Yano, J.; Hendrich, M.P.; Borovik, A. S. *Proc. Natl. Acad. Sci.* **2015**, *112*, 5319.
 26. Suga, M.; Akita, F.; Yamashita, K.; Nakajima, Y.; Ueno, G.; Li, H.; Yamane, T.; Hirata, K.; Umena, Y.; Yonekura, S.; Yu, L.-J.; Murakami, H.; Nomura, T.; Kimura, T.; Kubo, M.; Baba, S.; Kumasaka, T.; Tono, K.; Yabashi, M.; Isobe, H.; Yamaguchi, K.; Yamamoto, M.; Ago, H.; Shen, J.-R. *Science* **2019**, *366*, 334.
 27. Askerka, M.; Brudvig, G. W.; Batista, V. S. *Acc. Chem. Res.* **2017**, *50*, 41.
 28. Cady, C. W.; Crabtree, R. H.; Brudvig, G. W. *Coord. Chem. Rev.* **2008**, *252*, 444.

29. Wasylenko, D. J.; Palmer, R. D.; Berlinguette, C. P. *Chem. Commun.* **2012**, 49, 218.
30. Kärkäs, M. D.; Verho, O.; Johnston, E. V.; Åkermark, B. *Chem. Rev.* **2014**, 114, 11863.
31. Blakemore, J. D.; Crabtree, R. H.; Brudvig, G. W. *Chem. Rev.* **2015**, 115, 12974.
32. Matheu, R.; Garrido-Barros, P.; Gil-Sepulcre, M.; Ertem, M. Z.; Sala, X.; Gimbert-Suriñach, C.; Llobet, A. *Nat. Rev. Chem.* **2019**, 3, 331.
33. Dwyer, F. P.; Goodwin, H. A.; Gyarfas, E. C. *Aust. J. Chem.* **1963**, 16, 42.
34. Moyer, B. A.; Thompson, M. S.; Meyer, T. J. *J. Am. Chem. Soc.* **1980**, 102, 2310.
35. Takeuchi, K. J.; Thompson, M. S.; Pipes, D. W.; Meyer, T. J. *Inorg. Chem.* **1984**, 23, 1845.
36. Tseng, H.-W.; Zong, R.; Muckerman, J. T.; Thummel, R. *Inorg. Chem.* **2008**, 47, 11763.
37. Masaoka, S.; Sakai, K. *Chem. Lett.* **2009**, 38, 182.
38. Kaveevivitchai, N.; Zong, R.; Tseng, H.-W.; Chitta, R.; Thummel, R. P. *Inorg. Chem.* **2012**, 51, 2930.
39. Concepcion, J. J.; Jurss, J. W.; Templeton, J. L.; Meyer, T. J. *J. Am. Chem. Soc.* **2008**, 130, 16462.
40. Wasylenko, D. J.; Ganesamoorthy, C.; Henderson, M. A.; Koivisto, B. D.; Osthoff, H. D.; Berlinguette, C. P. *J. Am. Chem. Soc.* **2010**, 132, 16094.
41. Pushkar, Y.; Moonshiram, D.; Purohit, V.; Yan, L.; Alperovich, I. *J. Am. Chem. Soc.* **2014**, 136, 11938.
42. Betley, T. A.; Surendranath, Y.; Childress, M. V.; Alliger, G. E.; Fu, R.; Cummins, C.C.; Nocera, D. G. *Philos. Trans. R. Soc. Lond. B Biol. Sci.* **2008**, 363, 1293.
43. Betley, T. A.; Wu, Q.; Van Voorhis, T.; Nocera, D. G. *Inorg. Chem.* **2008**, 47, 1849.

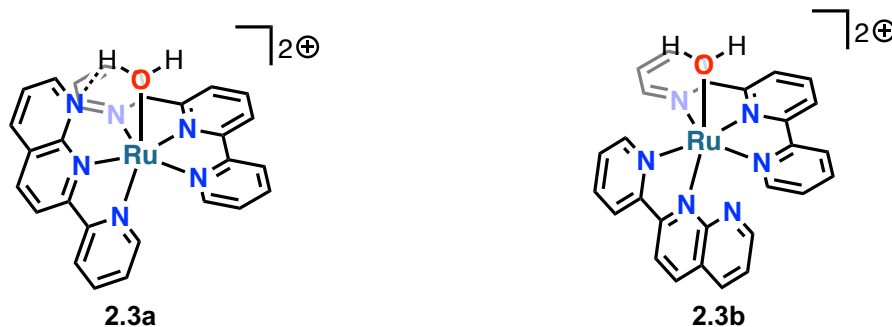
Chapter 2 – Appending Heteroatom Pendant Bases to the $[(\text{terpy})(\text{phen})\text{Ru}(\text{OH}_2)]^{2+}$ Platform

2.1 A Review of Pendant Bases in Molecular Ruthenium Water Oxidation Catalysis

Catalytic multielectron oxidations involving transition metals are typically understood to involve formally high-valent metal centers. As the metal becomes more electron-deficient, the thermodynamic cost of each subsequent oxidation grows as well. This challenge is exemplified in the catalytic oxidation of H_2O to O_2 , wherein the catalyst must reach oxidation numbers at least as high as $n + 2$ (wherein n is the oxidation number of the resting state of the catalyst). In the case of ruthenium-based water oxidation catalysts starting with Ru^{2+} or Ru^{3+} this means invoking Ru^{4+} or even Ru^{5+} over the course of the catalytic cycle. To further complicate matters, the four-electron oxidation of H_2O must be accompanied by the movement of four protons (H^+) away from the active site of the catalyst. In the last 10 years, several research groups have made efforts to improve ruthenium water oxidation catalysts by incorporating a pendant base into the second coordination sphere of the complex. It quickly became apparent, however, that oxidable bases such as nitrogen heterocycles or phenols would not survive adjacent to a high valent ruthenium-oxo moiety. It stands to reason that incorporating more oxidatively robust pendant bases might lead to more durable and faster catalysts.

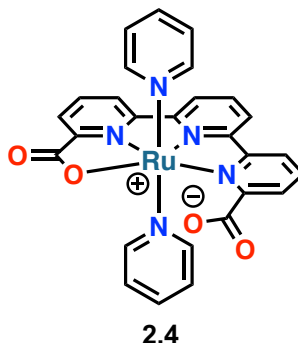
There are several examples of ruthenium water oxidation catalysts featuring pendant bases in the literature. Most are based on the $[(\text{terpy})(\text{bipy})\text{Ru}(\text{OH}_2)]^{2+}$ platform and the rest upon $[(\text{bda})\text{RuL}_2]$. The basic principle of action of pendant bases in the

water oxidation context is hydrogen bonding to water in the second coordination sphere of the metal, which can facilitate proton coupled electron transfer during catalysis. A brief review of pendant bases in water oxidation is provided below.

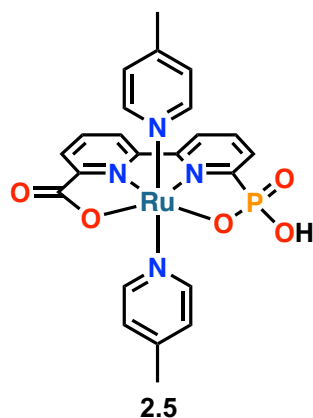


An early and striking example is the nearly simultaneous reports from the groups of Fujita/Thummel¹ and Yagi² in 2011 describing diastereomers of the complex $[(\text{terpy})\text{Ru}(\text{pynap})(\text{OH}_2)]^{2+}$ (pynap = 2-(pyridin-2-yl)-1,8-naphthyridine) (**2.3a** and **2.3b**). The diastereomers were designated *proximal* (with the naphthyridine nitrogen *cis* to the water ligand, **2.3a**) and *distal* (with the naphthyridine ligand *trans* to the water ligand, **2.3b**). Chemical intuition would suggest that the proximal isomer would be the better catalyst, given the close position of the unbound naphthyridine nitrogen to the aquo ligand. Interestingly, the opposite was true: the distal isomer performed much better than the proximal isomer under chemical oxidation conditions with CAN as the sacrificial oxidant, reaching 3200 turnovers within 50 h. The proximal isomer on the other hand achieved a turnover number of “approximately one” and more CO₂ was produced, presumably from some catalyst decomposition. The reason for the dramatic difference in catalytic performance was developed in a subsequent report from Yagi’s group. They proposed on the basis of computational results that as the proximal diastereomer is oxidized orbital amplitude develops on the pynap ligand rather than the Ru-O moiety³,

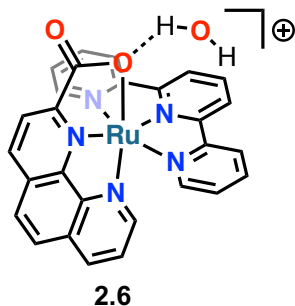
making the pynap ligand more electrophilic and thus more susceptible to nucleophilic attack by water and ultimately, degradation.



Perhaps the most impressive example of pendant base enhancement of water oxidation catalysis came in 2015 from Llobet's group, who successfully modified the platform developed by Sun and coworkers by replacing a tetradentate 2,2'-bipyridine-6,6'-dicarboxylic acid with the pentadentate [2,2':6',2''-terpyridine]-6,6''-dicarboxylic acid, forming **2.4**. In the ruthenium (II) oxidation state shown in **2.4**, the equatorial ligand binds in a κN^3O mode, with one of the carboxylates unbound, but as the metal is oxidized the dangling carboxylate can either bind to Ru, or dissociate to aid water nucleophilic attack. The authors evaluated catalyst performance exclusively by electrochemical methods, and reported an impressive 8000 s^{-1} turnover frequency at pH 7, thanks to the dangling anionic carboxylate. In a subsequent report⁴ the authors reported reaching turnover numbers of over 1 million by affixing the catalyst to multi-walled carbon nanotubes. A high turnover number of 8076 s^{-1} was maintained even after the grafting process. The authors went to considerable lengths to verify their catalyst was unchanged after extended electrolysis by using XAS. They also noted the absence of RuO_2 that would be indicative of catalyst degradation⁴. The performance of this system represents the state of the art for ruthenium-catalyzed H_2O oxidation^{5,6}.



Concepcion's group reported a H₂O oxidation catalyst (**2.5**) derived from [(bda)RuL₂] featuring the dual carboxylate/phosphonate ligand 6'-phosphono-[2,2'-bipyridine]-6-carboxylic acid. The kinetics in the presence of Ce⁴⁺ show first order dependence in [Ce⁴⁺] as determined using stopped-flow UV-visible spectroscopy to monitor loss of Ce⁴⁺. Looking at experimental rate constants, the hybrid ligand containing complex outperformed both Sun's catalyst and its phosphate congener: 1.2×10⁵ M⁻¹s⁻¹ for [(bpHc)Ru(pic)₂][ClO₄] (**2.5**) and 1.6 ×10⁵ M⁻¹s⁻¹ for [(bpHc)Ru(isq)₂] (where pic = 4-picoline and isq = isoquinoline). The related bda catalysts were slower by a factor of 10, with 6.7×10⁴ M⁻¹s⁻¹ and 1.8 ×10⁴ M⁻¹s⁻¹ for [(bda)Ru(pic)₂] and [(bda)Ru(isq)₂]. At a concentration of 100 μM, **2.5** reached a turnover frequency of 107 s⁻¹, while the bda complex at the same concentration had a TOF of 65 s⁻¹. Interestingly, Ce⁴⁺ did not perform well as a sacrificial oxidant with this system only reaching a turnover number of about 70. However, when cobalt(III) was used as the oxidant turnover numbers of 1600 were achieved⁷. It was hypothesized that Ce⁴⁺ associated with phosphonate moieties, hindering pendant base activity. Diphosphonate analogs of **2.5** reported by both our laboratory⁸ and Concepcion's group⁹ exhibited slightly higher turnover of 225 when Ce⁴⁺ was used as the oxidant.



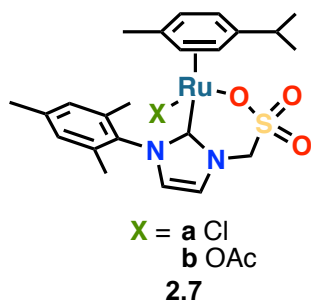
In 2017 Thummel's group published a report in which they investigated the effects of CAN upon catalyst decay. The study appears to have begun as examination of different supporting monoanionic ligand architectures, and accordingly they began by synthesizing complexes of the form [(terpy)Ru(L₂X)] using the following ligand library: 2-([2,2'-bipyridin]-6-yl)phenol, 2-(1,10-phenanthroline-2-yl)phenol, 2,2'-bipyridine-6-carboxylic acid, and 1,10-phenanthroline-2-carboxylic acid, with the latter ligand appearing in **2.6**. The complexes were then subjected to aqueous CAN and their H₂O oxidation performance assayed by manometry. The bipyridine-derived ligands were poor catalysts but the phenanthroline-containing catalysts performed well, especially **2.6**. More interestingly though, both **2.6** and an analog with a phenolate at the same position as the carboxylate exhibited almost identical performance, with the carboxylate complex reaching ~700 turnovers over 10 h. The authors were clearly intrigued and turned to mass spectrometry to study the effects of oxidant concentration on catalysis. After 8 equivalents of oxidant were added, a signal corresponding to the mass of the carboxylate complex emerged. They also assayed the headspace during CAN facilitated water oxidation with gas chromatography and found CO₂ present in the case of the phenolate complex. Overall, carboxylate complex **2.6** significantly outperformed its phenanthroline congener which reached 400 turnovers. Computational modeling

suggested that in its unbound form the carboxylate facilitated aquo ligand association to the ruthenium. Under the highly acidic conditions of CAN testing (pH 1) the carboxylate was inferred to be protonated and uncoordinated based on NMR evidence. In the solid state however, the carboxylate remained coordinated with an H-bonded water associated with the carbonyl oxygen of the ligand.

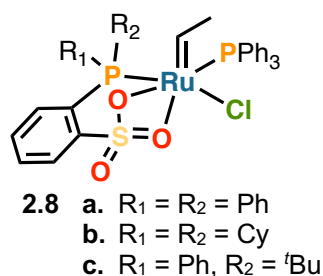
As can be seen, most oxygen pendant bases in the context of molecular ruthenium water oxidation catalysis have been either carboxylates or phosphonates. Sulfonates are much less basic, and as ligands more easily dissociated, all because in the sulfonate anion, the negative charge is delocalized over three oxygen atoms. Hence, sulfonates suggested themselves as attractive variants, and a literature survey of sulfonate ligands on ruthenium complexes and catalysts is warranted.

2.2 Literature Review of Sulfonate Ligands on Ruthenium Catalysts

Sulfonates are generally regarded as poorly coordinating¹⁰. The prototypical example is the triflate ligand which finds routine use as non-coordinating anion^{11,12}. This hemilabile behavior can be quite useful in catalysis. For example, a sulfonate can de-coordinate from a formally 18e⁻ catalyst to generate a more electrophilic 16e⁻ species. The incoming substrate can then bind to the catalyst. Later in the catalytic cycle, the sulfonate can re-coordinate and restore the electron count of the catalyst. Furthermore the sulfonate functional group is hydrophilic and confers favorable solubility in water¹³. A brief review of literature examples of ruthenium catalysts possessing sulfonate ligands as detailed below.

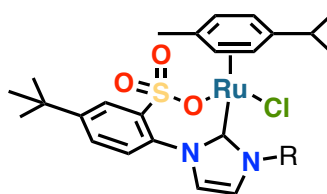


The group of Bruneau prepared ruthenium catalysts **2.7** possessing an N-heterocyclic carbene ligand with a pendant methylene sulfonates¹⁴. Interestingly, the chelating sulfonate compound was found not to undergo displacement of the coordinated arene in boiling acetonitrile. The authors took note of the ruthenium compound's thermal stability and tested it as a catalyst for the condensation of amines with alcohols and for alcohol etherification. In the *N*-alkylation of piperidine with benzyl alcohol, **2.7b** outperformed all but its iridium congener. The complex also effected the homocoupling of 2-phenylethanol to its corresponding ether, which the analogous iridium complex did not.



The group of Claverie prepared a series of *ortho*-substituted phosphine sulfonate complexes **2.8a-c** and found them to be active for ring-closing metathesis, cross-metathesis, and ring-opening metathesis polymerization despite having formal 18e⁻ configurations¹⁵. One would expect an 18e⁻ closed shell configuration to be inert

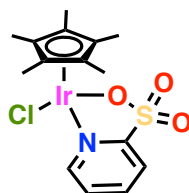
whereas a $14e^-$ species of the form $RuLX_2(=CHR)$ is needed for successful alkene metathesis. Nonetheless, a sulfonate complex prepared outperformed the Grubbs first-generation catalyst and approached the activity of the second-generation Grubbs system. A variable temperature NMR study of the ^{31}P resonances ranging from 22 to 60 °C revealed fluxional binding of the sulfonate, with an activation energy of 16.1 kcal/mol for the $\kappa^2-O,O' \rightarrow \kappa^1-O \rightarrow \kappa^2-O,O'$ isomerization. This finding is similar to calculated activation barriers for $\eta^3 \rightarrow \eta^1 \rightarrow \eta^3$ isomerization in allyl complexes.



2.9 R = **a** CH₂Mes
b CH₂Ph
c ⁿBu
d ⁱPr

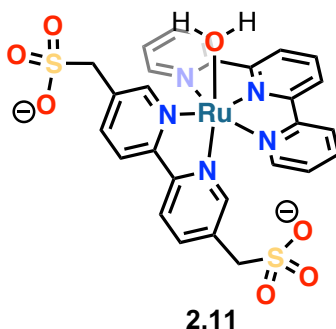
Li et al. reported¹⁶ a series of complexes featuring a carbene sulfonate ligands for ring-opening metathesis polymerization. **2.9a** performed the best out of the group, efficiently catalyzing the polymerization of norbornene as well as its copolymerization with cyclooctene with Et₂AlCl as a cocatalyst. The focus of this work was catalyst screening, and the authors did not comment on a particular advantage of the sulfonate.

The next two examples pertain specifically to water oxidation catalysis. As of this writing iridium complex **2.10** represents one of two molecular transition metal water oxidation catalysts with a sulfonate bearing ligand, so it is included here.



2.10

Koelewijn et al. prepared a series of iridium complexes based on the Cp*Ir fragment (where Cp* = pentamethylcyclopentadienyl anion)¹⁷. They screened six different ligands, including pyridine-2-sulfonate (resulting in **2.10**) and evaluated the complexes for water oxidation catalysis using Ce⁴⁺ as the oxidant, using detailed kinetic studies with UV–visible stopped-flow spectroscopy and analyzed the data using the reaction progress kinetics analysis method of Blackmond¹⁸. They found three clear phases in the reaction: catalyst activation, H₂O oxidation catalysis, and Ce⁴⁺ concentration-controlled catalysis at the end of the reaction. For IrCp*(pyrSO₃)Cl, a reaction order of ~1.6 was found in [catalyst] from both the method of initial rates and by studying the relationship of rate/Ir^{III} and [Ce⁴⁺]/[Ce⁴⁺]₀. The non-integer reaction order suggests that for IrCp*(pyrSO₃)Cl a monomer/dimer equilibrium was occurring. The sulfonate catalyst achieved a maximum turnover frequency of 0.54 mol Ce⁴⁺ [mol Ir]⁻¹s⁻¹ which was three times faster than for the carboxylate analog, and three times slower than a catalyst with a related alkoxide ligand. The authors also noted speciation of IrCp*(pyrSO₃)Cl when dissolved in neutral or acidic D₂O. From these data, they inferred that aquation of the iridium center and concurrent dissociation of the sulfonate moiety precedes water oxidation catalysis but the timescale at which this reaction occurs is not specified.



Yoshida et al. elaborated upon $[(\text{terpy})(\text{bipy})\text{Ru}(\text{OH}_2)]^{2+}$ (**2.12**) by incorporating pendant methylene sulfonates in the 5 and 5' positions of the bipyridine ligand (bpym = 2,2'-bipyridine-5,5'-bis(methanesulfonate)),¹⁹ forming **2.11**. The sulfonates reside in the second coordination sphere of the metal and neither coordinate to the metal nor displace a coordinated H₂O. The electrochemistry of the complexes was similar:

Table 2. 1 Comparison of redox couples of **2.11** and **2.12**

	Ru ^{2+/3+}	Ru ^{3+/4+}	cat.
$[(\text{terpy})(\text{bipy})\text{Ru}(\text{OH}_2)]^{2+}$ (2.12)	0.81 V	1.12 V	~1.3 V
$[(\text{terpy})(\text{bpym})\text{Ru}(\text{OH}_2)]^{2+}$ (2.11)	0.82 V	1.18 V	~1.3 V

The almost identical redox behavior would suggest that methylene sulfonate substitution does not significantly affect the electronic environment of the metal. However, testing of catalytic activity with CAN as the sacrificial oxidant revealed some interesting differences. In the presence of 25 mM CAN, **2.11** and **2.12** exhibited similar catalytic performance and both species reached over 90% yield of O₂ within 2 h. However, in the presence of 4 mM CAN, the sulfonate system outperformed the parent system by about 50% (3 turnovers vs. 4.5 turnovers). The authors attribute this difference to the ability of the sulfonates to coordinate Ce⁴⁺ ions but reactivity differences and catalytic performance are modest. Nonetheless, Ce-catalyst interaction is shown a crystal structure of their complex in which the methylene sulfonates are bound to Ce⁴⁺ ions forming a coordination polymer. Two ruthenium centers are linked via μ_2 -oxo moieties.

2.3 Motivation

Transition metal carboxylate intermediates are known to lose $\text{CO}_2^{20,21}$ both in closed-shell and odd-electron species, and electrochemical oxidation of carboxylate anions forms radicals that readily lose CO_2 , the basis of the Kolbe electrolysis. We considered sulfonate as an alternative pendant base to carboxylate that would be less basic, hence still available to help catalysis even under acidic conditions that protonate carboxylates or phosphonates, while possibly being more oxidatively stable. Given that $[(\text{terpyridine})(2,2'\text{-bipyridine})\text{Ru}(\text{H}_2\text{O})]^{2+}$ (**2.12**) is the most well studied platform for molecular water oxidation we chose it as the basis for synthetic elaboration. Thummel's replacement of 2,2'-bipyridine with 1,10-phenanthroline (Table 2.2) led to significant improvements in both rate and turnover number when using Ce^{4+} as the sacrificial oxidant.

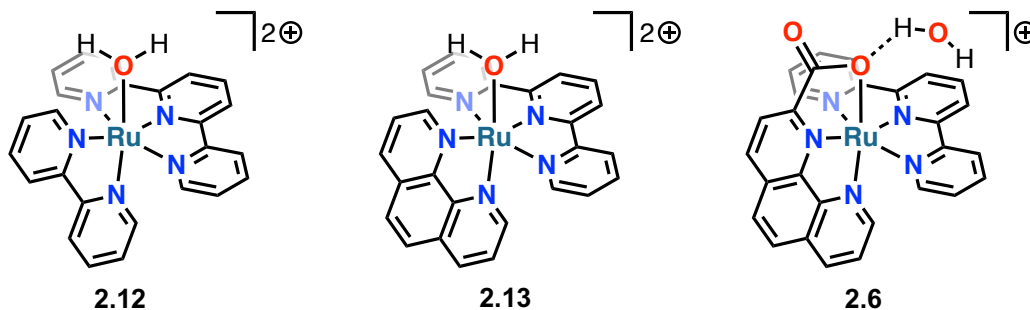


Table 2.2 Improvements upon the $[(\text{terpy})(\text{bipy})\text{Ru}(\text{OH}_2)]^{2+}$ platform

catalyst	$K_{\text{obs}} (\text{s}^{-1})$	TON
2.12	0.019	190
2.13	0.028	450
2.6	0.15	720

Furthermore, incorporation of a carboxylate pendant base increased turnover number by 60% compared with the parent phenanthroline complex **2.13**. We hypothesized that

a weaker pendant base might still facilitate H⁺ transfer without becoming protonated itself during catalysis. We aimed to find a suitable combination of pendant base and ligand scaffold which would increase the oxidative durability of the ligand. Thus we opted to retain the phenanthroline framework, noting that electro-oxidation potential of 1,10-phenanthroline is much higher (>2 V versus Ag/AgCl) than uncatalyzed H₂O oxidation potential (~1.5 V versus Ag/AgCl at pH 7 on glassy carbon)²². In order to complete our comparative study, we targeted both the phosphonate monoester and sulfonate derivatives of phenanthroline as ligands for the [(terpyridine)RuL₃]²⁺ fragment.

2.4 Synthesis and Characterization

Both ligands described herein are prepared from the synthon 2-chlorophenanthroline (**2.16**, Figure 2.1) which is prepared from a modified literature protocol. Briefly, 1,10-phenanthroline is *N*-alkylated with MeI and to afford *N*-methylphenanthroline. The iodide salt is then oxidized with KO^tBu in air to the *N*-methylphenanthrone in good yield²³. Dealkylation/halogenation with PCl₅ in POCl₃/xylenes affords the desired 2-chlorophenanthroline in very good yield (60.5% over three steps). The last step is a modification of literature procedures²⁴. In our hands even prolonged refluxing (>24 h) of *N*-methylphenanthrone in the presence of PCl₅ and POCl₃ resulted in only partial conversion of the starting material to product²⁴. Fortunately, addition of xylenes as a cosolvent and increasing the reaction temperature resulted in complete conversion. The purification was also quite simple requiring only filtration, washing with pentanes, and a basic aqueous workup.

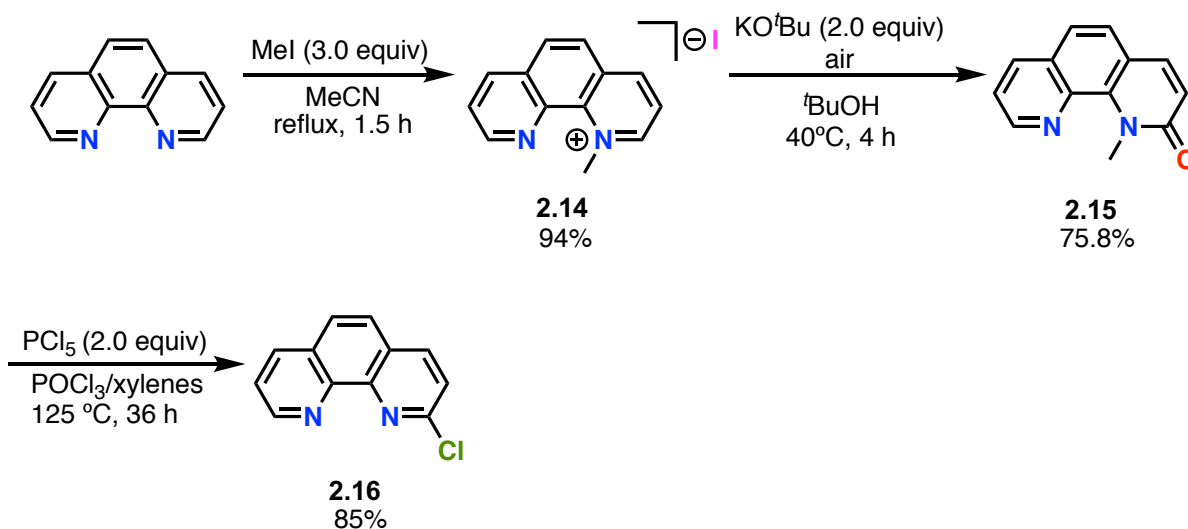


Figure 2.1 Improved synthesis of 2-chlorophenanthroline.

The phosphonate ligand is synthesized (Figure 2.2) in good yield by Hirao coupling of 2-chlorophenanthroline with diisopropyl phosphite²⁵. The product diisopropyl phosphonate is a pro-ligand that hydrolyzed in situ for metalation.

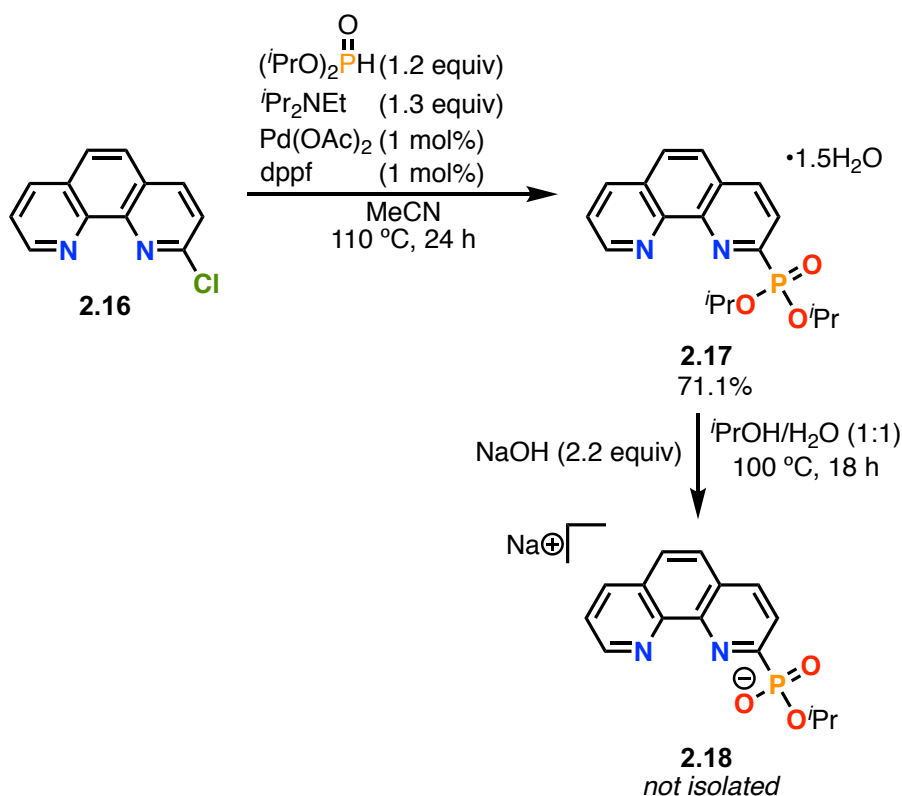


Figure 2.2 Synthetic scheme for diisopropyl (2-(1,10-phenanthroline-2-yl)phosphonate and its phosphonic acid sodium salt

As shown in Figure 2.3, the phosphonate complex is initially obtained as the chloride salt **2.20**. As coordination of chloride may lead to catalyst inactivation as well as itself be oxidized, rather than water, we chose to replace the chloride counterion with non-coordinating triflate by silver salt metathesis.

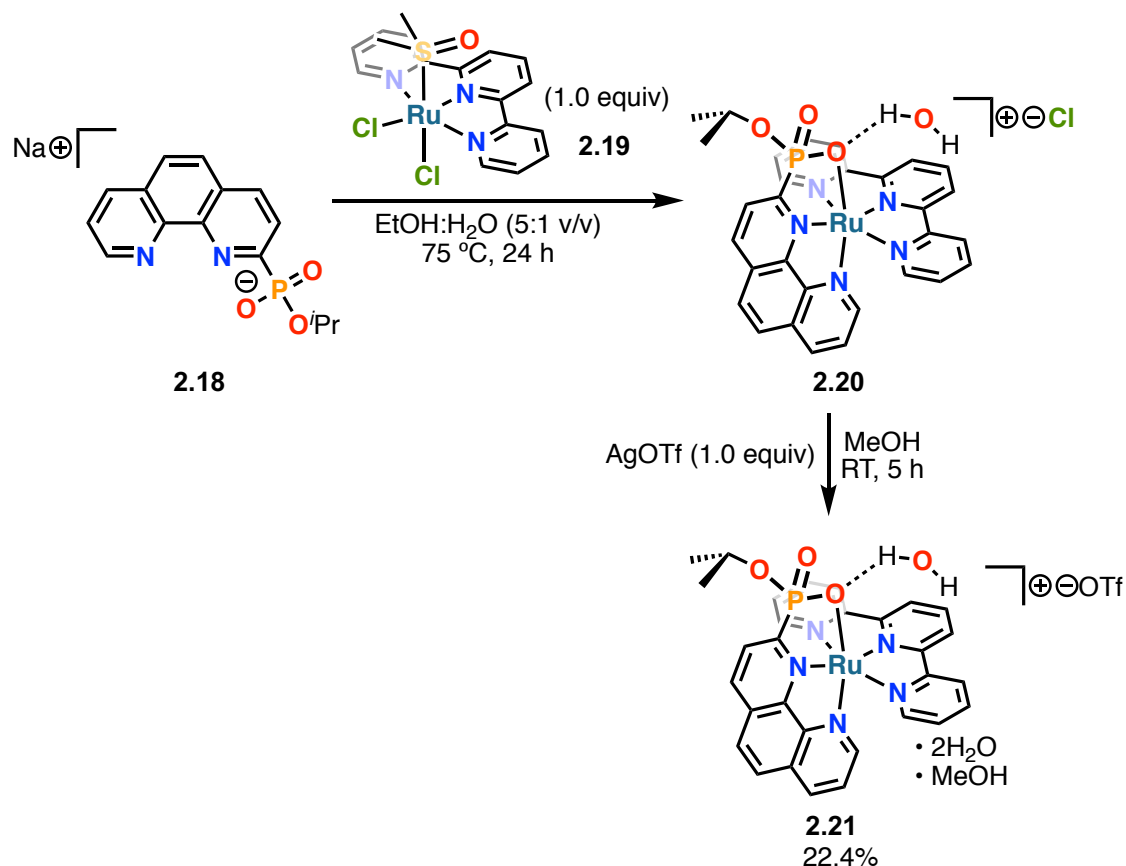


Figure 2.3 Synthesis of **2.21**. The complex was first isolated as its chloride salt and then converted to the triflate

As shown in Figure 2.4, the ligand and novel compound 1,10-phenanthroline-2-sulfonic acid (**2.23**) was prepared *via* modification of the Strecker alkyl sulfonate synthesis described by Besthorn et al. originally published in 1920²⁶. Thus, 2-chloro-1,10-phenanthroline was reacted with sodium sulfite in an ethanol/water mixture at pH 7.2 to yield the desired phenanthroline sodium salt. The zwitterion can be isolated by acidification to pH 1. Elemental analysis indicates the product is isolated as a dihydrate. It is freely soluble in trifluoroethanol or dmsO and slightly soluble in ethanol and water.

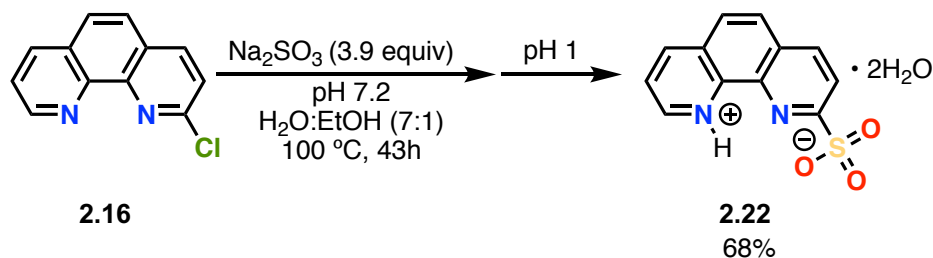


Figure 2.4 Synthesis of **2.22**

In Figure 2.5, **2.22** is neutralized with NaOH and reacted with a solution of putative species **2.23** in EtOH/H₂O to obtain the desired complex in 80% yield. **2.23** is prepared by treating **2.19** with 2 equivalents of AgOTf in EtOH/H₂O. The exact identity of L in **2.23** is not entirely clear. Gravimetric analysis of the AgCl produced in the reaction suggests that not all the chloride is abstracted upon treatment with AgOTf. Initial efforts at synthesizing **2.24** suffered from very low (<10%) yields. However when **2.19** was prepared and stored under strictly anoxic conditions²⁷ the yield of **2.24** increased dramatically.

2.21 is an air stable, red-orange microcrystalline solid which is moderately soluble in water, dichloromethane, and acetone. Combustion analysis was consistent with the presence of one methanol and two water molecules, which makes sense because the sample was crystallized from MeOH. The solid-state structure of a different salt revealed the complex to be a monohydrate (see below).

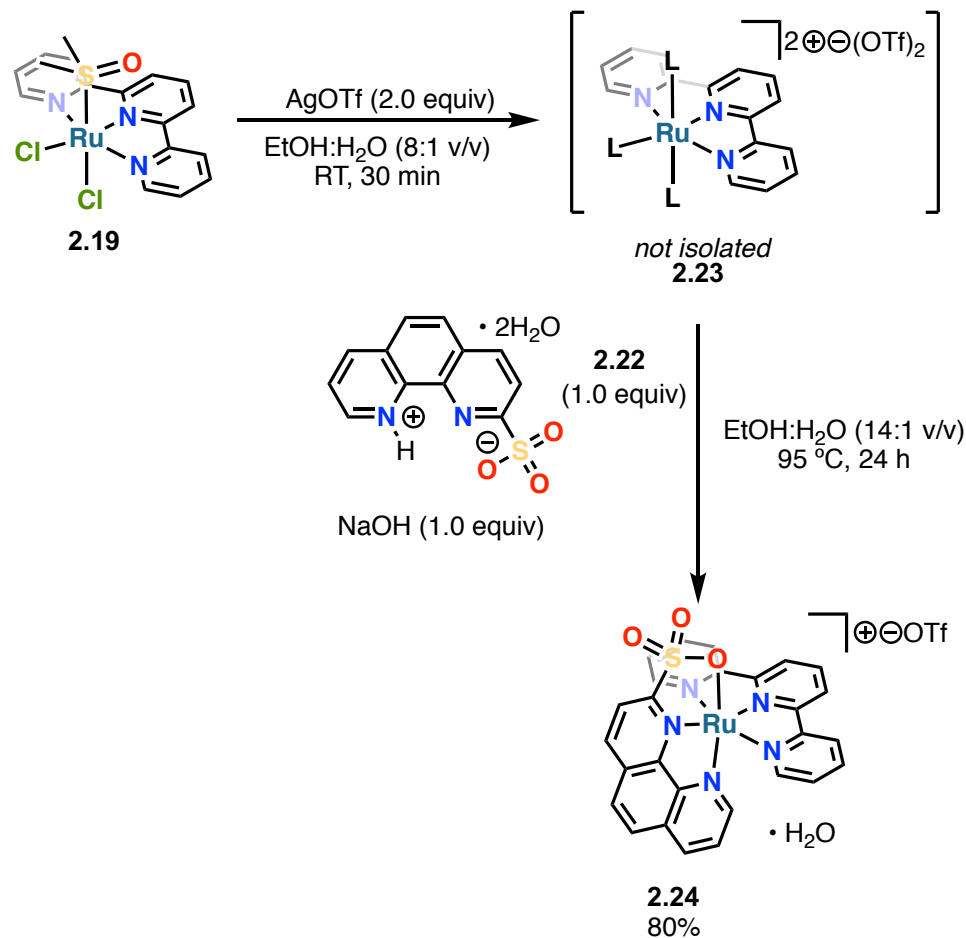


Figure 2. 5 Synthesis of **2.24**

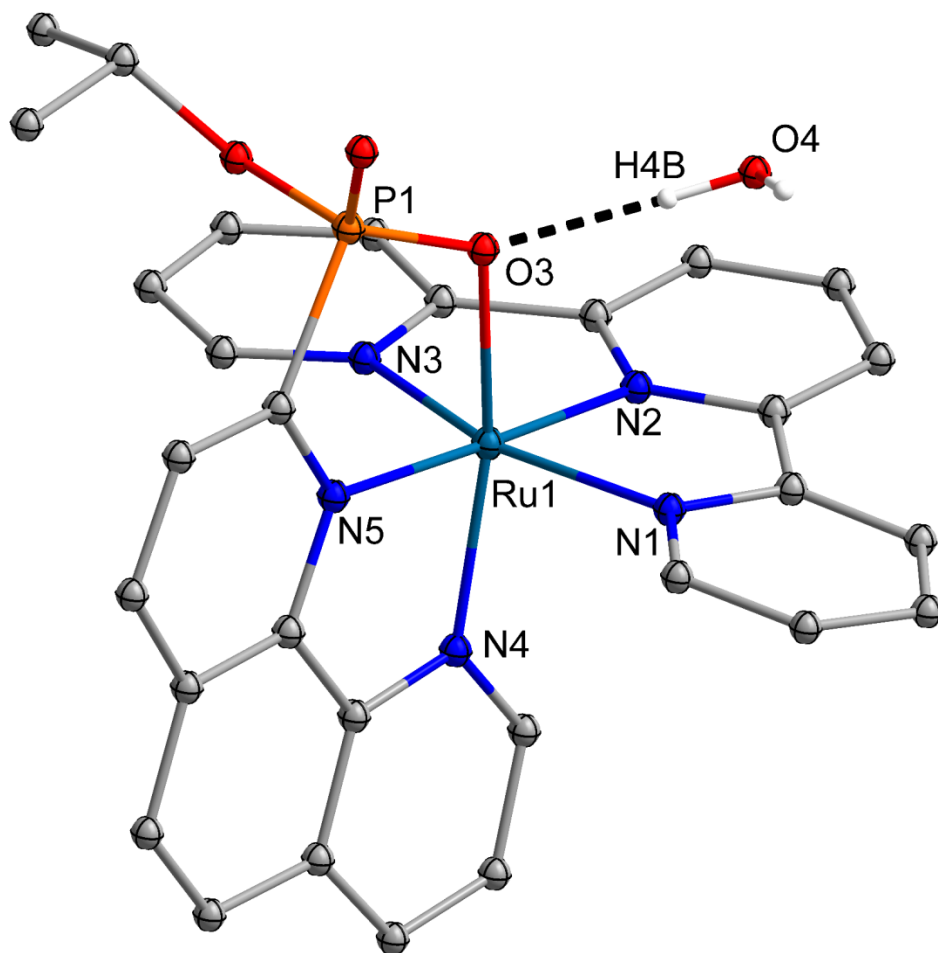
There was initial difficulty in obtaining diffraction quality crystals of the phosphonate complex as its triflate salt. We therefore turned to a more hydrophobic anion in the hope of obtaining higher quality crystals. Fortunately, the phosphonate complex was crystallized well as the tetrakis(pentafluorophenyl)borate salt.

The tetrakis(pentafluorophenyl)borate species was obtained by dissolving potassium tetrakis(pentafluorophenyl)borate and **2.21** together in MeOH and stirring at room temperature for 30 minutes. The solvent was evaporated, and the residue partitioned between with methylene chloride and water. The dark red organic phase was

dried over Na₂SO₄, filtered, and concentrated to a minimum volume. The saturated solution was then carefully layered with pentanes and allowed to stand for 48 h, during which time the complex crystallized as large red-orange blocks.

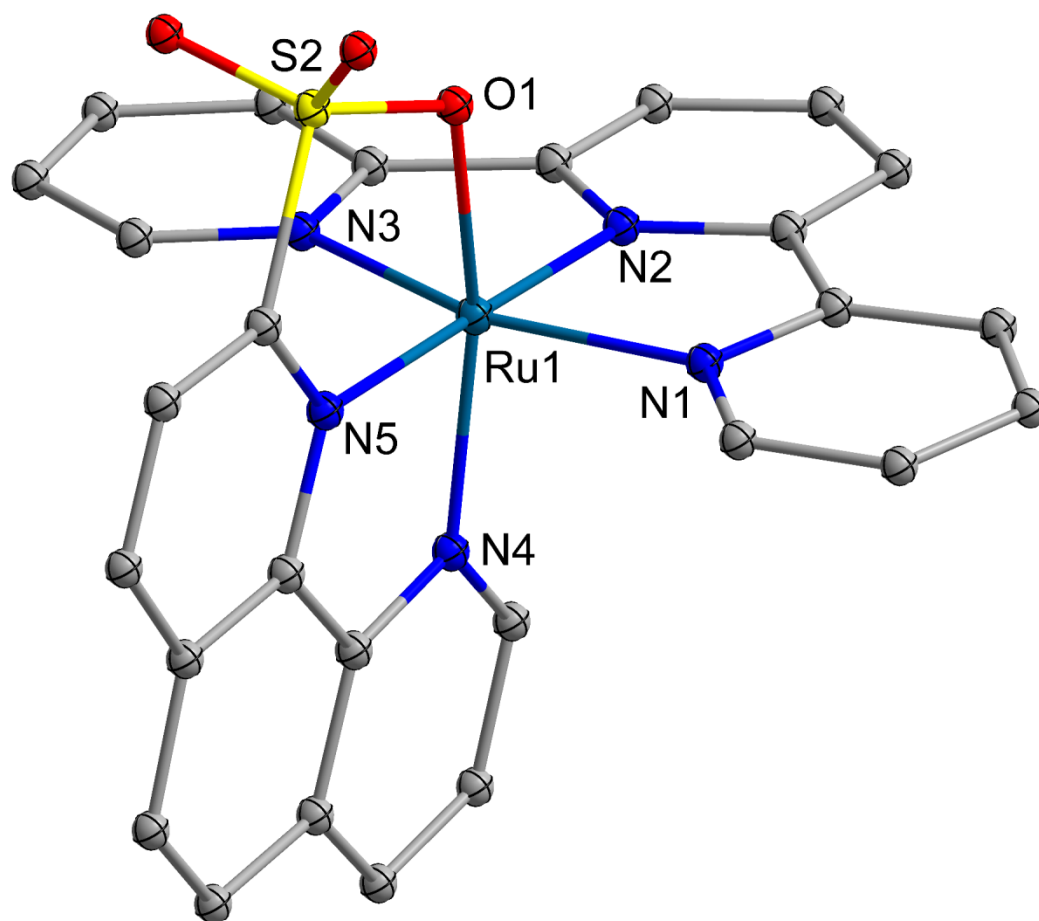
The solid-state structure of **2.21-BARF** (Figure 2.6) reveals a distorted octahedral geometry in which the sulfonate is bound to the ruthenium, *trans* to the unsubstituted pyridine ring of the phenanthroline. The ruthenium to O—P bond distance of 2.162 Å is slightly longer than 2.146 Å carboxylate oxygen-ruthenium of the Thummel complex **2.6**, perhaps because of the greater steric demand of the *i*PrO unit, or simply because bonds to P in **2.21-BARF** are longer than bonds to the carboxylate C in **2.6**. A water is hydrogen bonded (1.911 Å) to the metal bound P-O moiety suggesting the ability of the phosphonate oxygen to act as a pendant base.

The solid-state structure of **2.24** (Figure 2.7) has a similar coordination geometry to that of **2.21**. However, in **2.24** the Ru-O bond is longer (2.180 vs 2.162 Å) and possibly in compensation, the Ru-N(phenanthroline) bonds are slightly shorter: Ru1-N4 is 0.053 Å shorter and Ru1-N5 is 0.035 Å shorter. The structure was solved by using SQUEEZE and assigning electron density corresponding to 0.38 H₂O molecules; it is not possible to determine the location of the water. Future work may include growing new crystals under different conditions. We note that bulk sample from different preparations showed combustion analysis consistent with one water, either hydrogen bonded as in **2.21-BARF** or possibly coordinated.



Bond	Distance (Å)	Angle (°)	
N1-Ru1	2.088	N1-Ru-N2	79.11
N2-Ru1	1.983	N2-Ru-N3	79.64
N3-Ru1	2.080	N3-Ru1-N5	99.33
N4-Ru1	2.061	N5-Ru1-N1	101.93
N5-Ru1	2.030	O3-Ru1-N5	81.71
O3-Ru1	2.162	O3-Ru1-N2	97.30
O1-P1	1.601	N5-Ru1-N4	80.20
O2-P1	1.471	N4-Ru1-N2	100.86
O3-P1	1.544	O3-Ru1-N1	91.22
O3-H4B	1.911	O3-Ru1-N3	92.13
		N3-Ru1-N4	95.25
		N4-Ru1-N1	88.09

Figure 2. 6 Solid state structure of **2.21-BARF** with selected bond distances and angles. Thermal ellipsoids shown at 30% probability. $B(C_6F_5)_4^-$ counterion omitted for clarity



Bond	Distance (Å)
N1-Ru1	2.069
N2-Ru1	1.969
N3-Ru1	2.040
N4-Ru1	2.008
N5-Ru1	2.065
O1-Ru1	2.180
O1-S2	1.488
O2-S2	1.435
O3-S3	1.446

Angle (°)	
N1-Ru-N2	79.45
N2-Ru-N5	79.42
N5-Ru1-N4	100.68
N4-Ru1-N1	100.46
O1-Ru1-N4	79.08
O1-Ru1-N2	102.06
N4-Ru1-N3	80.55
N3-Ru1-N2	98.31
O1-Ru1-N5	96.49
N5-Ru1-N3	90.47
N3-Ru1-N1	93.18
N1-Ru1-O1	87.3

Figure 2. 7 Solid state structure of **2.24** with selected bond distances and angles. Thermal ellipsoids shown at 30% probability. Triflate counterion and uncoordinated water molecule omitted for clarity.

2.5 Testing with Sacrificial Oxidant

The experiments described herein were performed by graduate student colleague Colton Breyer. Initial screening of catalyst performance compared **2.6** to analogs **2.21** and **2.24** prepared in our laboratory. We measured pressure buildup as an indication of oxygen production. Thus, a solution of catalyst was injected into a custom-made manometry apparatus with temperature control, and the pressure monitored. Our initial screening compared results using $[\text{catalyst}]_0 = 20 \mu\text{M}$ in $[\text{CAN}]_0 = 0.200 \text{ M}$. HNO_3 was added to maintain pH 1 conditions and prevent decomposition of CAN. We found that **2.21** generated the least O_2 , reaching 3.3% of theoretical yield, 59 turnovers. The sulfonate however performed very well and reached 98.9% yield, 2424 turnovers.

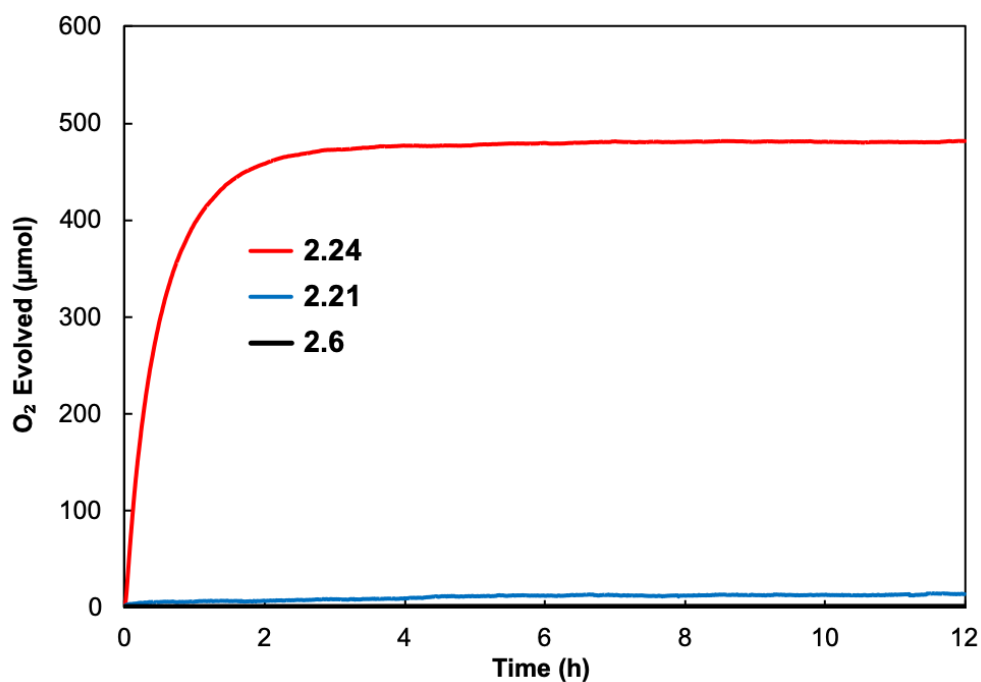
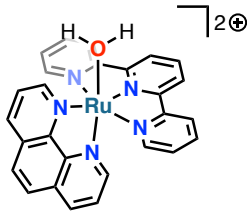
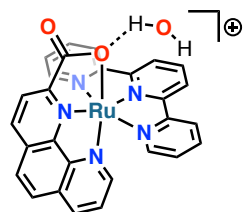
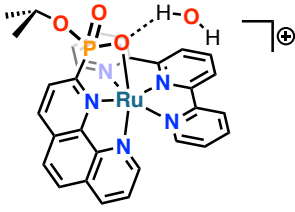
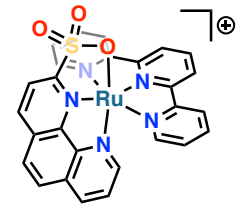


Figure 2.8 O_2 evolution traces determined by manometry for **2.6**, **2.21**, and **2.24**. $[\text{cat}]_0 = 20 \mu\text{M}$, $[\text{CAN}]_0 = 0.200 \text{ M}$, pH = 1

2.24 achieved even higher turnover numbers, reaching TON = 7402 with $[\text{catalyst}]_0 = 5 \mu\text{M}$ and $[\text{Ce}^{4+}]_0 = 0.200 \text{ M}$. Initial rate studies (Figures 2.9 and 2.10)

revealed a pseudo first order rate constant of 0.89 s^{-1} . Sulfonate complex **2.24** performs significantly better than other complexes in the mononuclear family of complexes of the type $[(\text{terpyridine})(\text{N}^{\wedge}\text{N})\text{RuL}]^{n+}$ as summarized in the table below:

Table 2.3 Comparison of catalytic performance and durability

catalyst	$K_{\text{obs}} (\text{s}^{-1})$	TON
 <p>2.13</p>	0.028	450
 <p>2.6</p>	0.15	720
 <p>2.21</p>	-	59
 <p>2.24</p>	0.88	2424

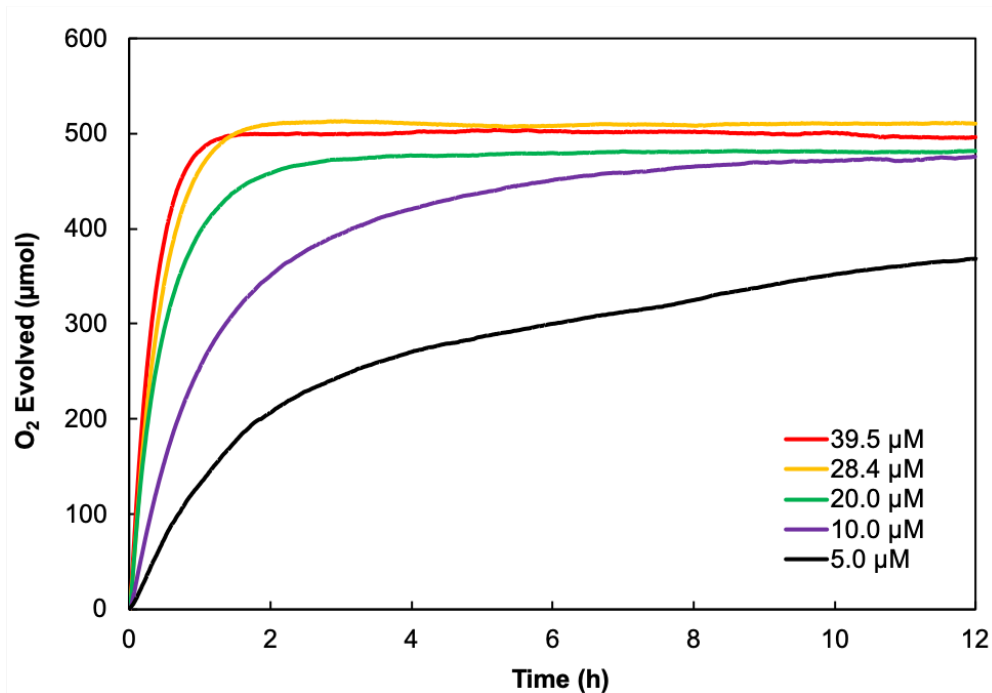


Figure 2.9 O_2 evolution over 12 h of catalysis at different concentrations of **2.24**. $[\text{CAN}]_0 = 0.200\text{M}$, $T = 30\text{ }^\circ\text{C}$

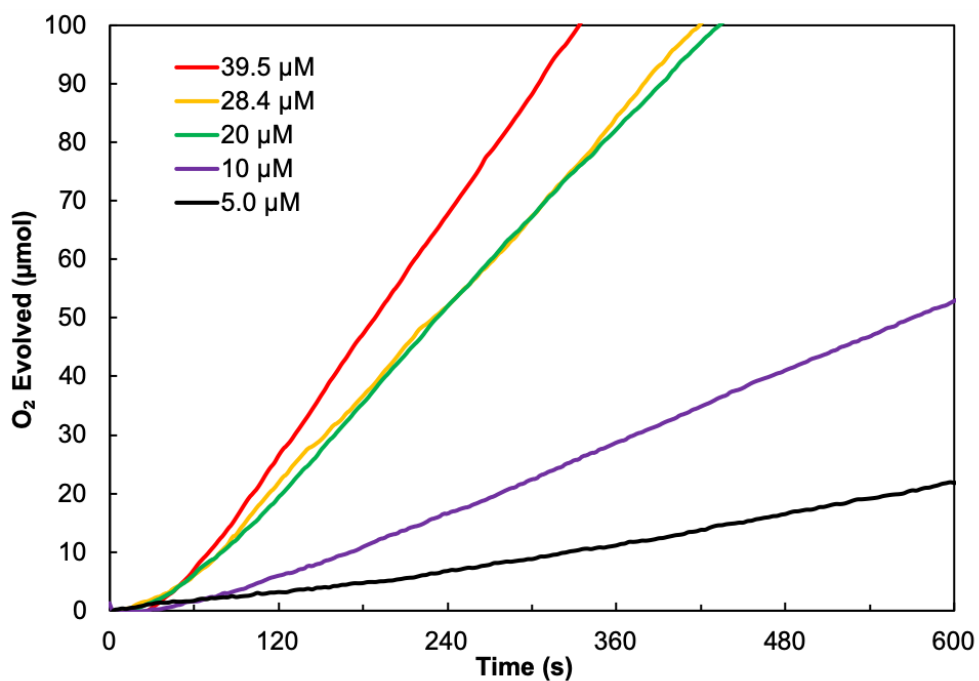


Figure 2.10 O_2 evolution within the first 10 minutes of catalysis at different concentrations of **2.24**. $[\text{CAN}]_0 = 0.200\text{ M}$, $T = 30\text{ }^\circ\text{C}$

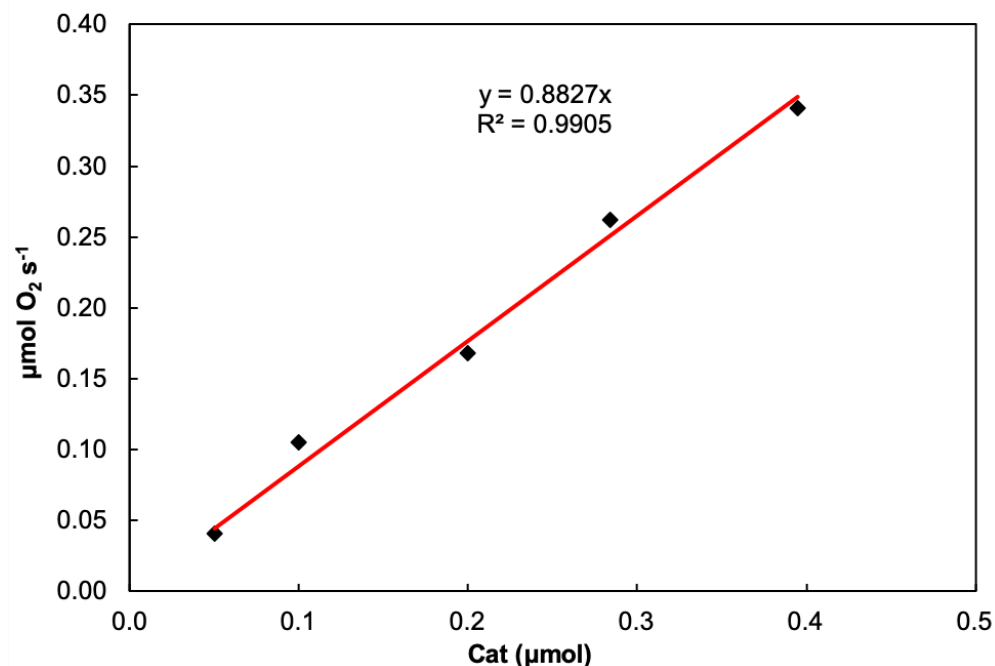


Figure 2.11 Determination of pseudo first-order rate constant of **2.24**. Note that the total amount of catalyst in μmol rather than $[\text{cat}]$ is plotted, to ensure agreement of units

2.6 Electrochemistry

Sulfonate **2.24** exhibits well behaved electrochemistry, undergoing a reversible 1-electron oxidation at 0.663 V vs. Ag/AgCl, which we assign as the $\text{Ru}^{2+/3+}$ couple, followed by an irreversible oxidation event at 1.104 V immediately preceding the onset of a catalytic wave (Figure 2.12). In contrast, **2.6** and **2.21** both show irreversible 2+/3+ couples. Moreover, **2.24** shows no crossover on the return wave if the catalyst is driven to 1.6 V suggesting that homogenous electrocatalysis is maintained. **2.6** and **2.21** do exhibit crossover on the return scan of the catalytic wave implying they are chemically altered in some way upon induction of catalysis²⁸. These phenomena are well documented in the case of phosphonate-containing complexes⁸. The maximum catalytic current developed at 1.6 V was similar for all three species.

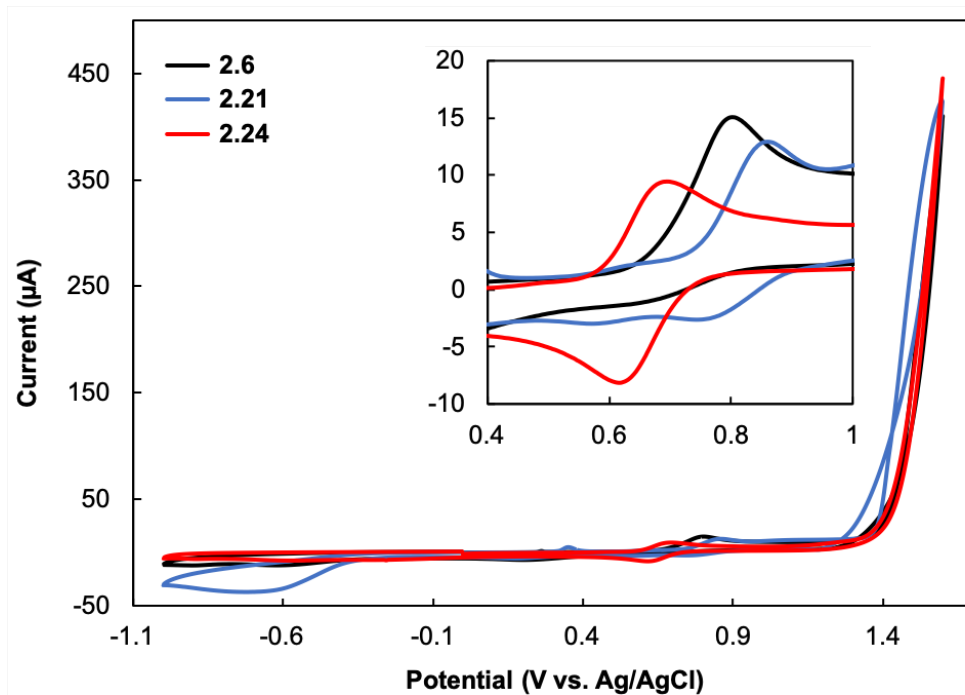


Figure 2. 12 Comparison of cyclic voltammograms of **2.6**, **2.21**, and **2.24** (pH 7 phosphate buffer, $\mu = 0.5$, 1 mM catalyst, 3 mm GCE)

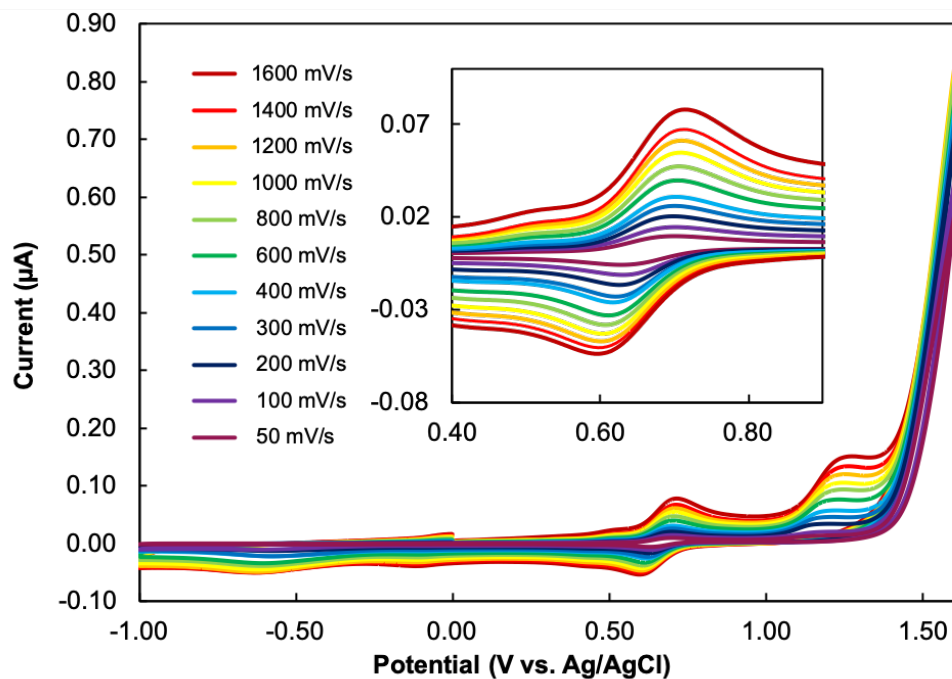


Figure 2. 13 Variable scan rate study of **2.24** from 50 – 1500 mV/S (pH 7 phosphate buffer, $\mu = 0.5$, 1 mM **2.24**, 3 mm GCE)

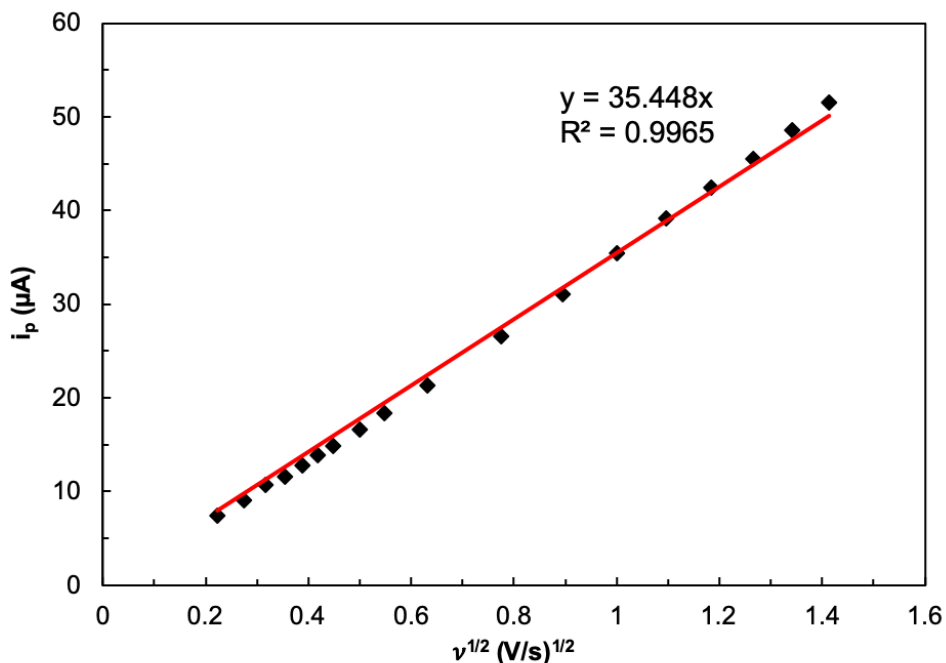


Figure 2. 14 Plot of peak current vs. square root of scan rate for **2.24**

In Figure 2.13, as the scan rate increases the $\text{Ru}^{2+/3+}$ couple of **2.24** remains reversible. However, the feature at 1.104 V becomes more pronounced and remains irreversible. Scan rate dependence (Figures 2.13 and 2.14) of the $\text{Ru}^{2+/3+}$ couple of **2.24** revealed a diffusion coefficient of $D = 3.3 \times 10^{-6} \text{ cm}^2/\text{s}$ as determined with the Randles-Sevcik equation. The most analogous complex for which there is data available is $[(\text{terpy})(\text{bpz})\text{Ru}(\text{OH}_2)]^{2+}$ (bpz = 2,2'-bipyrazine) for which $D = 1.1 \times 10^{-7} \text{ cm}^2/\text{s}$ is the diffusion coefficient derived from the $\text{Ru}^{2+/4+}$ couple. For reference $D = 7.3 \times 10^{-6} \text{ cm}^2/\text{s}$ for $[\text{Ru}(\text{NH}_3)_6]^{2+}$ in H_2O ($\mu = 0.5$, KNO_3)^{29,30}.

The Pourbaix diagram of the **2.24** is strikingly different from that of **2.12**³¹ (Figure 2.15). The diagram for **2.24** shows two pH dependent regions. A pK_a value of ~ 1.85 was calculated for the aquo complex in the $\text{Ru}(\text{III})$ state. It worth noting the relatively small number of points at pH values less than 2 for **2.24**. Challenges at low pH include

the difficulty in obtaining accurate pH measurements with a standard pH meter, and difficulty to buffer solutions. Above the $\text{Ru}^{3+}\text{-H}_2\text{O}$ complex $\text{pK}_a \approx 1.85$, the $E(\text{Ru}^{2+/3+})$ vs pH line has a slope of 54.2 mV/pH unit which is consistent with $1\text{H}^+/1\text{e}^-$ proton coupled electron transfer. The next oxidation appears to be pH-independent, which is usually ascribed to only ET occurring, but here may also result from intramolecular proton transfer, or, if the timescales of proton and electron transfer events are very different as in intramolecular proton transfer the slope of the line will be zero and the process will look like a 1e^- oxidation.

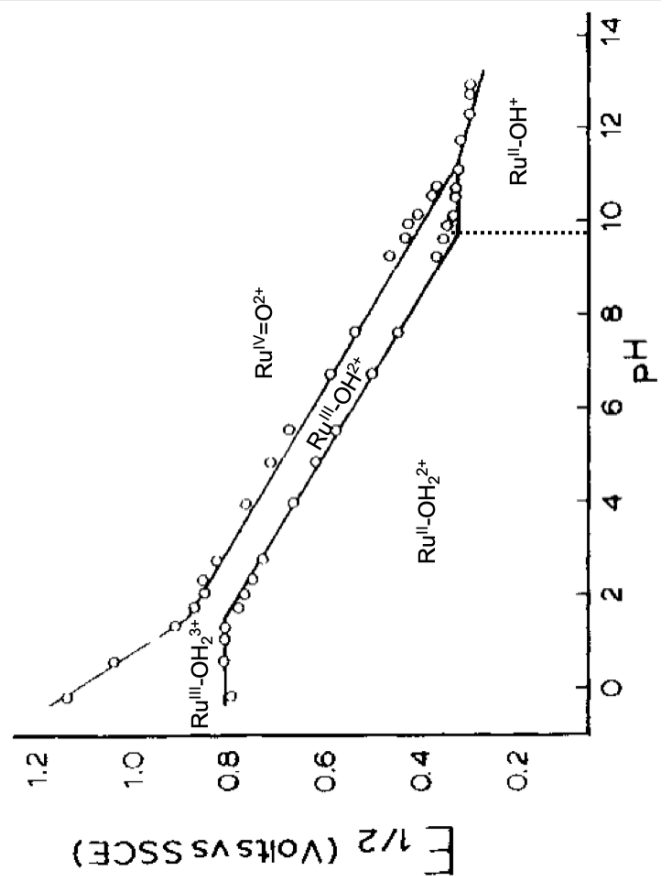
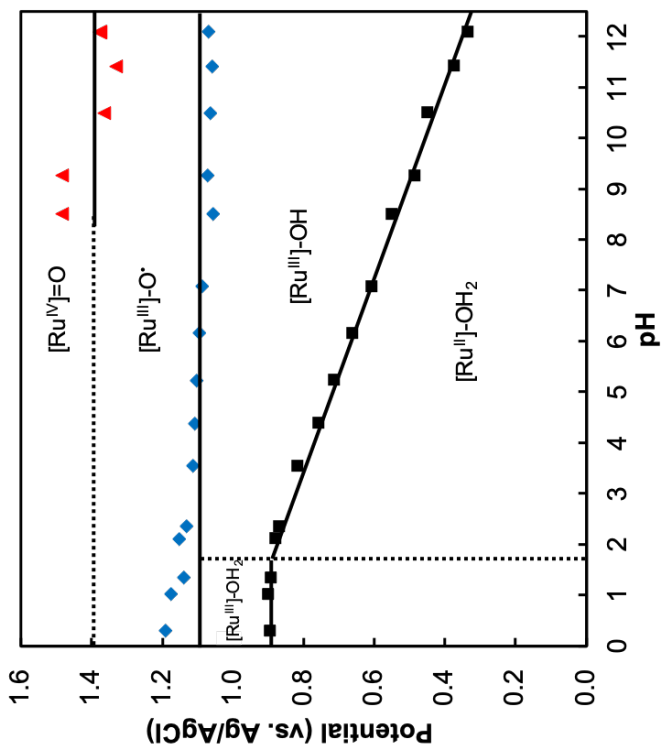


Figure 2.15 a. Pourbaix diagram of **2.12** ($\mu = 0.1$, $T = 23.0 (\pm 0.1) ^\circ\text{C}$ (E vs. SSCE) (adapted from ref. 25)
 b. Pourbaix diagram of **2.24** ($\mu = 0.5$, $T = \text{RT}$ (E vs Ag/AgCl))

2.7 Computational Results

We were interested in the mechanism by which **2.24** operated and turned to computations for insight. The following calculations were performed by Prof. Djamaladdin Musaev of the Center for Scientific Computation at Emory University.

The oxidative process is modeled as a series of discrete one- e^- or one- H^+ losses. The solid-state structure of **2.24** was used to generate an energy minimized structure. A water molecule was then introduced near the metal center and the geometry optimized. Several bonding motifs were compared, and the lowest energy structure **I** was found to exhibit a water ligated to the metal center, with each OH unit donating a hydrogen bond to one oxygen of the sulfonate. This structure was used as the basis for subsequent calculations.

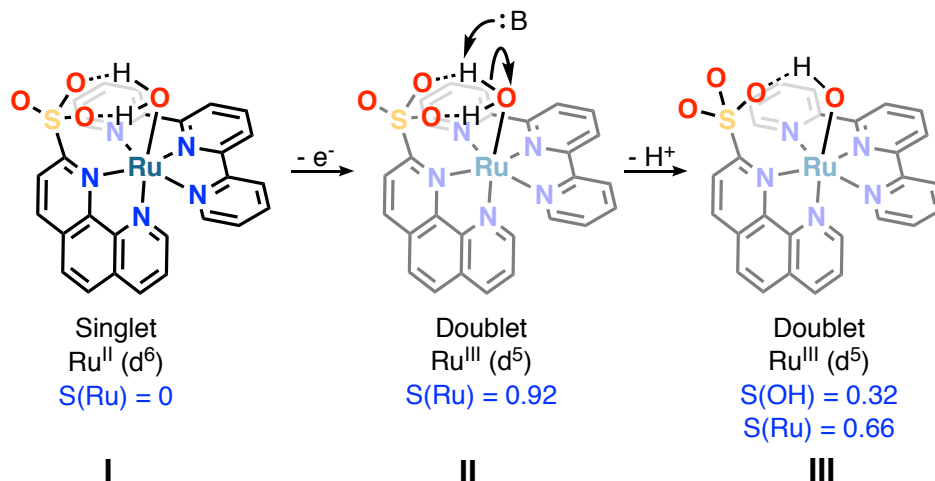


Figure 2.16 First PCET oxidation of **2.24**. Note that the deprotonation comes from solvent, not the sulfonate pendant base

One electron oxidation of **I** ($S = 0$, singlet) is predicted to afford species **II** that is formally Ru(III) ($S = 0.92$, doublet). Next, **II** is predicted to undergo deprotonation by

bulk water to yield a second doublet species **III** now exhibiting radical character on both the Ru ($S = 0.66$) and the newly formed hydroxo ligand ($S = 0.32$).

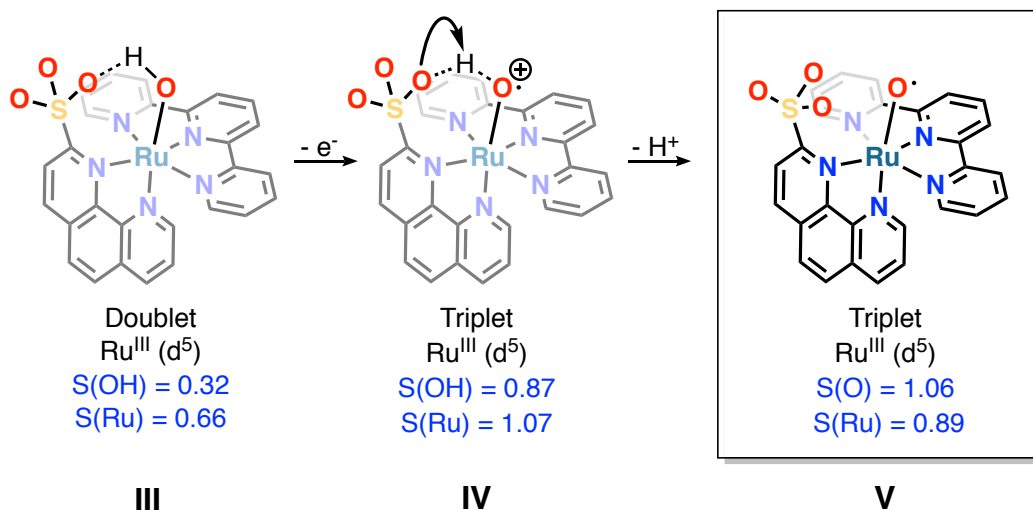


Figure 2. 17 Formation of the $\text{Ru}^{\text{III}}\text{-O}^\bullet$. Note the two unpaired spins on both **IV** and **V**. The sulfonate acts as an internal base in the last step.

To our surprise, calculations suggest that $1e^-$ oxidation of **III** results in diradical species **IV** ($S(\text{OH}) = 0.87$, $S(\text{Ru}) = 1.07$; triplet) and a proton transfer event wherein the proton is transferred to the sulfonate with the weakly basic sulfonate acting as a pendant base, deprotonating the oxidized hydroxo ligand. Note that such an intramolecular PCET is consistent with our Pourbaix diagram. The sulfonate is then predicted to transfer the proton to bulk water affording **V**, a Ru(III) oxyl ($S(\text{O}) = 1.06$, $S(\text{Ru}) = 0.89$; triplet). At this point the $\text{Ru}(\text{II})\text{-OH}_2$ starting material has lost $2e^-$ and 2H^+ .

After two sequential losses of electron and proton (possibly PCET, or not) the ruthenium center is formally in the $3+$ oxidation state, which is unusual. This finding implies that oxidation of **III** is taking place at the bound H_2O or hydroxide rather than the ruthenium center^{32,33}. Most proposed H_2O oxidation mechanisms invoke a formally Ru^{IV}

center after two PCET events at a Ru^{II} center. There is a single report of generation of Ru^{III}-O[•] from oxidation of a Ru^{II}-OH₂, but that species was a very poor H₂O oxidation catalyst, only reaching 6 turnovers^{34,35}, though the catalyst was good at C-H oxidation; the ligand environment was rather different compared to ours.

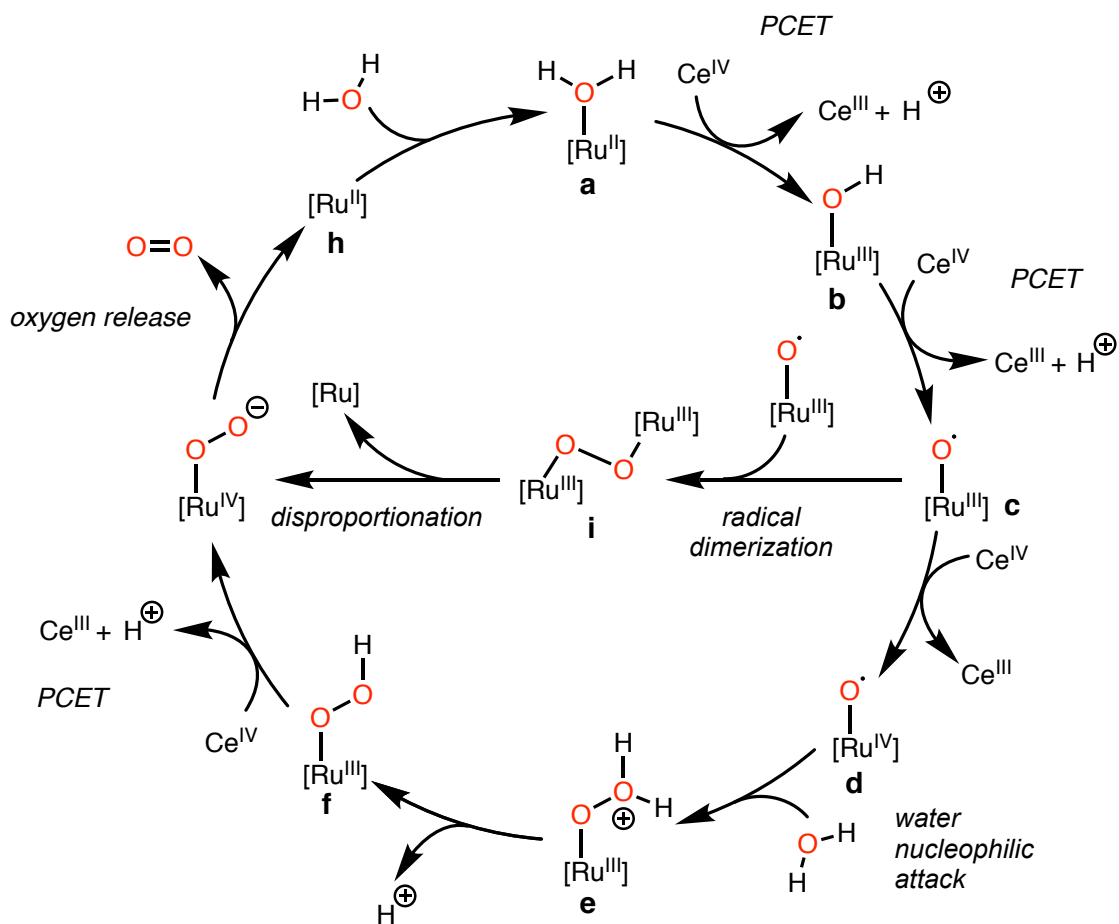


Figure 2. 18 Proposed catalytic cycle for the oxidation of water by **2.24**.

Specific reference is now made to the proposed catalytic cycle in Figure 2.18. From Ru(III) oxyl state **c** two pathways are possible. Oxyl **c** can be further oxidized by 1e⁻ at a cost of 12.9 kcal/mol to yield **d** that readily undergoes nucleophilic attack by water (-2.9 kcal/mol) to produce **e**, a protonated hydroperoxo complex. Then, **e** undergoes essentially barrierless proton loss (0.1 kcal/mol) yielding **f**, featuring a

terminal hydroperoxo ligand, which can then be oxidized by $1e^-$ and undergo an exothermic (-4.0 kcal/mol) proton loss to yield η^1 -peroxide. That peroxide exothermically releases oxygen to regenerate the catalyst.

Another pathway envisions exothermic dimerization (-16.1 kcal/mol) of two Ru-oxyl units to afford **i**, a μ_2 -O₂ dimer. Dimer **i** can then exothermically release oxygen (-8.4 kcal/mol) regenerating units of **a**. This process may in fact be disproportionation³⁶. The formal oxidation state and d-electron count of the ruthenium center in the later stages of catalysis are currently under study. Preliminary results suggest that oxidation past the [Ru^{III}]-O[•] state occurs at the sulfonate rather than the ruthenium center, but further work is needed to verify these processes.

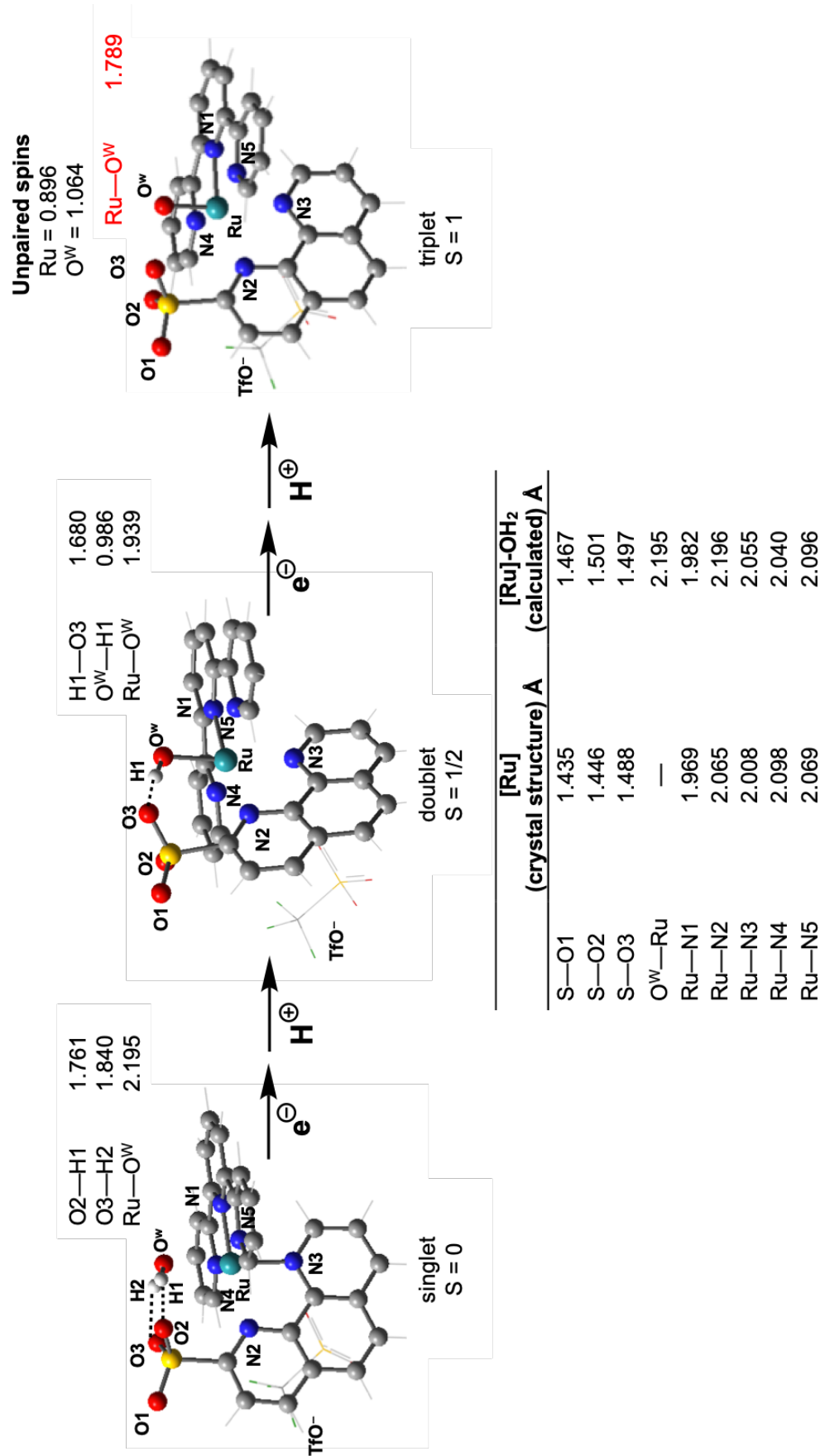
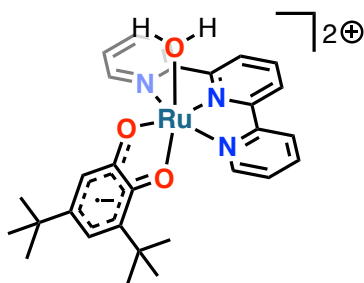


Figure 2.19 Computed bond distances for the first two oxidations of **2.24**. A comparison to the original crystal structure is provided in the table

2.8 EPR Results

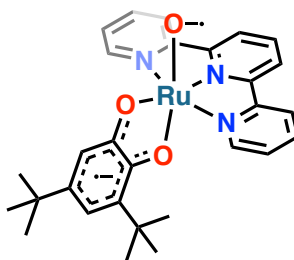
Our computational results motivated us to seek experimental verification of the spin state distribution of the ruthenium-oxygen moiety during catalysis. We turned to EPR spectroscopy to accomplish this task. There are two examples of EPR detection of terminal ruthenium oxyl species in the literature and both are reviewed below.

The first report of a ruthenium terminal oxyl came from Tanaka's group in 2003³⁷. They first prepared a complex of a benzosemiquinone ligand (3,5-di-*tert*-butyl-1,2-benzosemiquinone = Bu₂-SQ) with the [(terpy)Ru(LL)(H₂O)]²⁺ platform. Due to the non-innocent nature of the semiquinone ligand, the formal oxidation number should be regarded as a Ru^{III} center as indicated in **2.25** below (note that Bu₂-SQ is monoanionic):



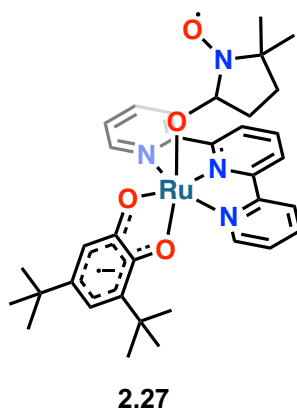
2.25

The authors then subjected **2.25** to sequential deprotonations. The first deprotonation with KO^tBu gives the expected metal hydroxido complex. However, upon addition of a second equivalent of base, an intramolecular charge transfer event from the oxygen to the ruthenium occurs, affording Ru^{II}-oxyl **2.26**:

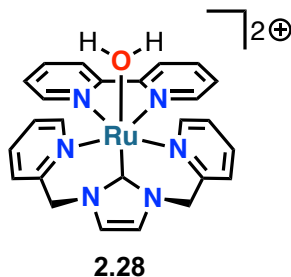


2.26

The aquo and oxyl complexes were characterized by x-ray diffraction, cyclic voltammetry and UV-visible spectroscopy. Confirming the radical character of the Ru-O moiety required EPR spectroscopy. After addition of 3 equivalents of KO^tBu to a CH₂Cl₂ solution of the aquo complex, a broad isotropic signal at $g = 2.054$ and a hyperfine structure consistent with an $S = 1$ triplet species was detected below 5 K. Addition of the spin trap DMPO (5,5-dimethyl-1-pyrroline N-oxide) gave a 12-line sharp signals centered at $g = 2.006$, strongly suggestive of the formation of a spin adduct **2.27** shown below:



The second example of a ruthenium oxyl came from Kojima's group in 2016³⁴. They prepared the ruthenium carbene complex **2.28** with the goal of stabilizing a Ru^{III}-O[•] center over the Ru^{IV}=O species. Unlike in the Tanaka paper they did not use a redox active ligand, instead relying on the strong σ -donating properties of the carbene *trans* to the Ru-O bond to encourage formation of the oxyl:



After adding one equivalent of CAN to an aqueous solution of **2.28**, an EPR signal could be detected below 5 K, exhibiting a signal at $g_{\perp} = 2.419$ and $g_{\parallel} = 1.586$ ($\langle g \rangle = 2.177$). The authors assert that a typical $\langle g \rangle$ values for Ru^{III} ($S = 1/2$) is about 2.2 and thus assigned an oxidation state of 3+ to the ruthenium center in this experiment, with the species being simply the Ru^{III} version of **2.28** for which they did have a crystal structure. To generate the Ru^{III}-oxyl, removal of a second electron was necessary, and because the redox potential was near that of Ce^{IV}/Ce^{III}, 10 equiv of Ce^{IV} were needed. Under these conditions, three features with g values of 4.31, 2.321, and 1.801 were seen (Figure 2.20). However, the authors did not discuss the data shown in Figure 2.20, but rather to confirm a Ru^{III}-O[•] assignment used XANES spectroscopy was used to make the assignment of a ruthenium oxyl. **2.28** was an active catalyst for C-H oxidation on a variety of substrates. The authors pointed to the ability of **2.28** to oxidize benzaldehyde as evidence of a Ru^{III}-O[•] over a Ru^{IV}=O species.

We performed EPR experiments in the Borovik laboratory at University of California, Irvine, with graduate student Jason Lee operating the instrument; I wish to acknowledge his essential contributions. All spectra were recorded at 77 K.

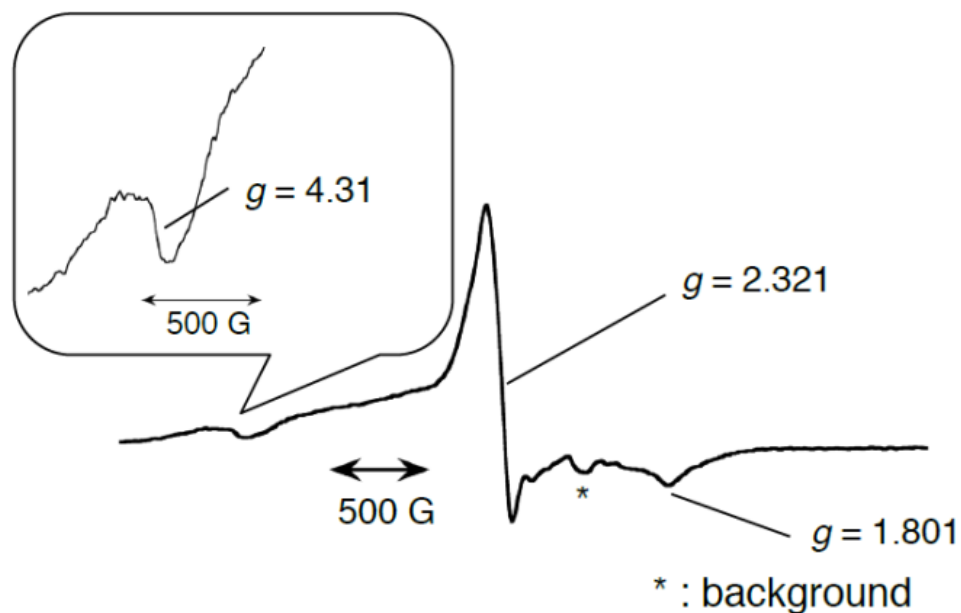


Figure 2. 20 EPR spectrum (10 K) of **2.29** + 10 equiv Ce^{4+} . Microwave frequency: 9.382 GHz, microwave power: 5.024 mW, modulation frequency: 100 kHz, modulation amplitude: 12.00 G (figure from ref. 32)

First, a 200 μL portion of a 2 mM solution of **2.24** was added to an EPR tube and then carefully frozen in liquid N_2 . The spectrum was recorded and the sample was EPR silent as expected (Figure 2.21a). The frozen solution was then allowed to thaw to room temperature. 20 μL of freshly prepared 20 mM aqueous CAN was added, the tube shaken and allowed to react for 5 minutes and then frozen in liquid N_2 . The EPR spectrum was recorded and a very weak signal was detected at approximately 375 mT (Figure 2.21b). The tube was again removed, allowed to thaw to room temperature, and a further 20 μL of CAN solution added. The tube was shaken and then allowed to react for 5 minutes, frozen, and the spectrum recorded. This time (Figure 2.21c) a broad signal was detected at $g_{\perp} = 2.4$ and a weak signal at $g_{\perp} = 4.3$. These data are similar to the results in the Kobayashi paper though their experiments were carried out in CH_2Cl_2 and at liquid helium temperatures. The first two features match 10 K data from Kojima's

group closely (reproduced in Figure 2.20), which is encouraging. In our case the signal was rather featureless with no apparent hyperfine coupling, which may be due to antiferromagnetic coupling of the oxyl oxygen and the ruthenium (III) center.

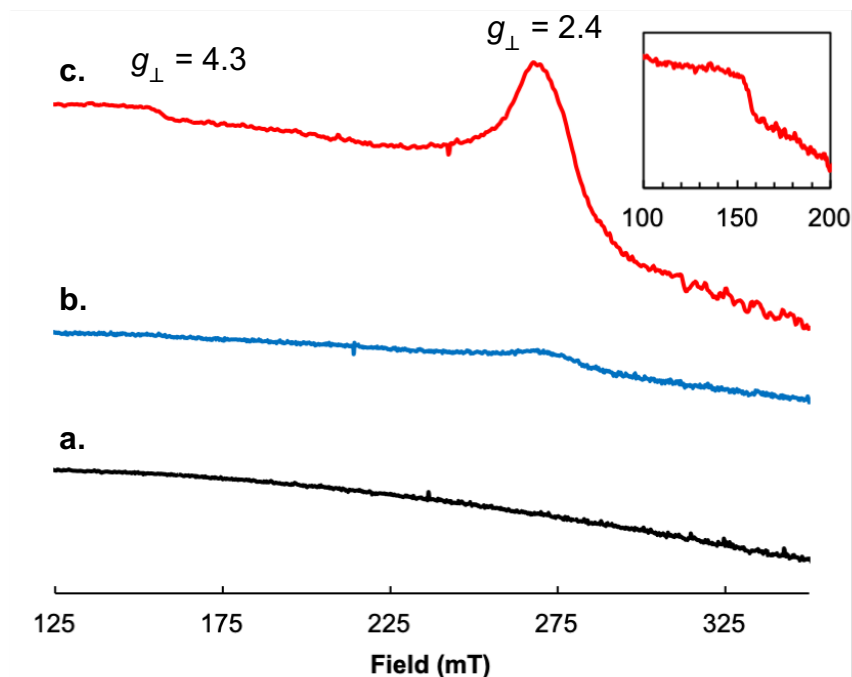
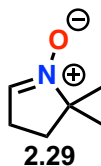


Figure 2. 21 EPR spectrum (77K) of (a) **2.24**, (b) **2.24** + 1 equiv Ce^{4+} , (c) **2.24** + 2 equiv Ce^{4+}

The tube was again allowed to thaw to room temperature and 20 μL of a freshly prepared 2mM solution of 5,5-dimethyl-1-pyrroline N-oxide (DMPO, **2.29**) was added.



The solution was shaken and kept at room temperature and the spectrum acquired. A new signal appeared with $g_{\perp} = 2.01$. The spectrum appears to show two sets of hyperfine couplings, one from an $I = 1$ nucleus (giving rise to 3 lines), one from an $I =$

3/2 nucleus giving rise to 4 lines. Both signals show hyperfine constants of approximately 21 MHz.

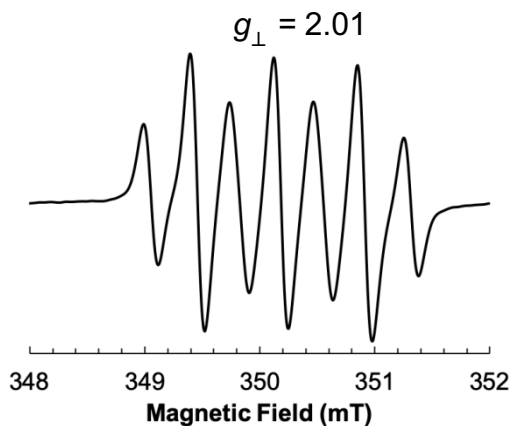


Figure 2. 22 EPR spectrum (RT) **2.24** + 2 equiv Ce⁴⁺ + 1 equiv DMPO

Clearly, our results were different from that reported by Kobayashi et al. However, we noted a report from Ueda et al³⁸ in which DMPO was used to attempt to trap reactive Fe^{III}-OH intermediates. The authors contend that trapped DMPO-OH can be further oxidized by simultaneously generated Fe^{IV}=O species. After one hydroxylation and two PCET events, the final product is DMPO=O. Indeed, the spectra we obtained in our experiment closely resembles the simulated spectrum of DMPO=O (see figure 2.23).

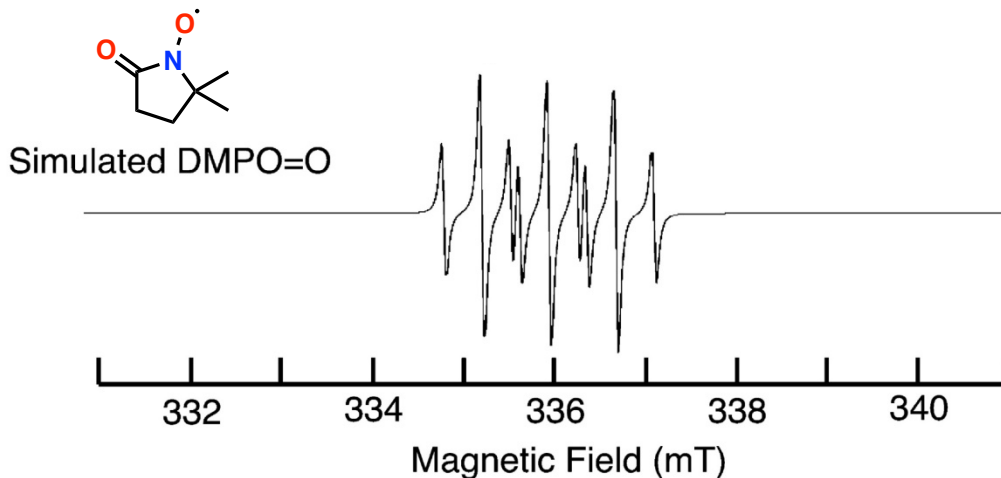


Figure 2. 23 Simulated spectrum of DMPO=O ($a_H = 0.41$ T, $a_N = 0.72$ T)
(adapted from ref.38)

One can envision a process in which a $\text{Ru}^{\text{III}}\text{-O}^\bullet$ unit reacts with DMPO to generate a spin adduct. An intramolecular PCET event leads to release of an O atom transfer product that is subsequently oxidized by $1e^-$ to afford DMPO=O (see figure 2.24):

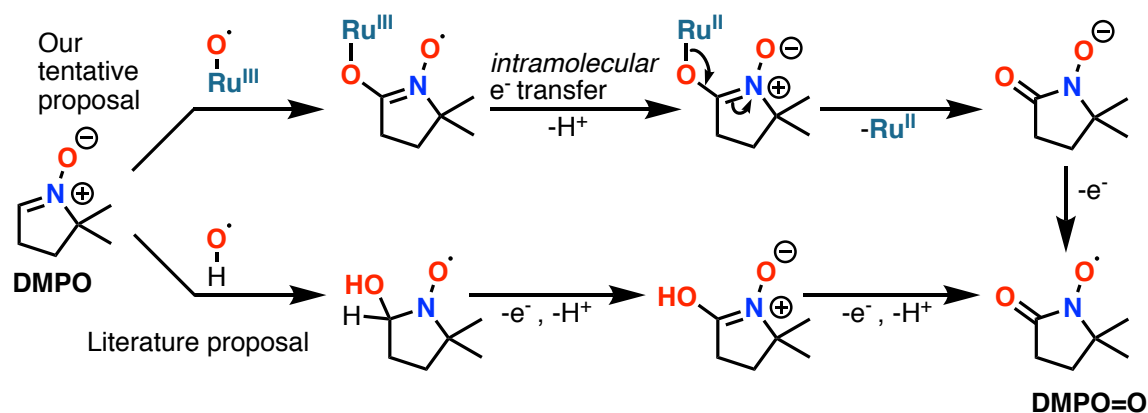


Figure 2. 24 A plausible mechanism for the formation of DMPO=O by **2.24** compared to a mechanism proposed in literature.

Mass spectrometric studies of the same reaction sequence (**2.24** + 2 equiv Ce^{4+} + 1 equiv DMPO) are underway in order to observe the molecular ion of the spin adduct.

2.9 Conclusions and Future Work

Two analogs of carboxylate complex **2.6**, containing phosphonate monoester (**2.21**) and sulfonate (**2.24**) pendant bases respectively were synthesized and characterized by combustion analysis, NMR spectroscopy, and x-ray crystallography. **2.21** performed poorly under chemical oxidation conditions with CAN whereas **2.24** performed very well demonstrating TOF = 0.88 s^{-1} and TON as high as 7402. Both complexes displayed electrocatalytic waves but **2.24** was particularly well-behaved electrochemically. A Pourbaix diagram, DFT studies, and EPR experiments suggest the intermediacy of a ruthenium (III) oxyl and facilitation of H^+ transfer by the sulfonate during in catalysis by **2.24**, which are new findings in molecular ruthenium-catalyzed water oxidation.

There are several avenues for further study of the sulfonate system. The durability of **2.24** should be tested by serial addition of CAN after the theoretical limit of oxygen is reached. Continued O_2 production after the initial reservoir of CAN is depleted would attest to catalyst durability.

Cyclic voltammetry of **2.24** revealed a catalytic wave that had not yet peaked and so driving the catalyst beyond 1.6 V might exhibit even higher catalytic current; if the current maximum can be reached an estimate of the electrocatalytic rate constant can be obtained. Bulk electrolysis of **2.24** would provide electrocatalytic TON and should be performed.

EPR studies of **2.24** under serial addition of CAN suggest the presence of ruthenium-oxygen radical species. The continuous wave EPR system we used did not allow assignment of spin density on either the metal or oxygen. Very low temperature

(<5 K), pulsed EPR instrumentation, and H₂¹⁷O isotope labeling experiments will likely offer further insight into the nature of the Ru-O bond of oxidized species derived from

2.24.

Finally, the use of an oxygen atom transfer (OAT) reagent in both aqueous and non-aqueous milieu may allow isolation of the proposed Ru^{III}-O[•] intermediate. If the oxyl species can be generated in bulk and characterized by UV-visible spectroscopy then stopped flow kinetics analysis may present an attractive option for studying **2.24** under sacrificial oxidant conditions.

There are also opportunities to elaborate upon the framework of **2.6**. The phenanthroline ligand framework offers rich site for synthetic elaboration. One insightful suggestion comes from Kang et al³⁹ and Shimoyama et al³⁵ who suggest that positioning a strongly σ donating ligand such as a carbanion or a carbene will increase the radical character of the ruthenium-oxygen moiety. As shown in Figure 2.25, a carbanionic ligand such as benzo[h]quinoline-2-carboxylic acid **2.30** presents an attractive target as a C,N,O analog of **2.6**.

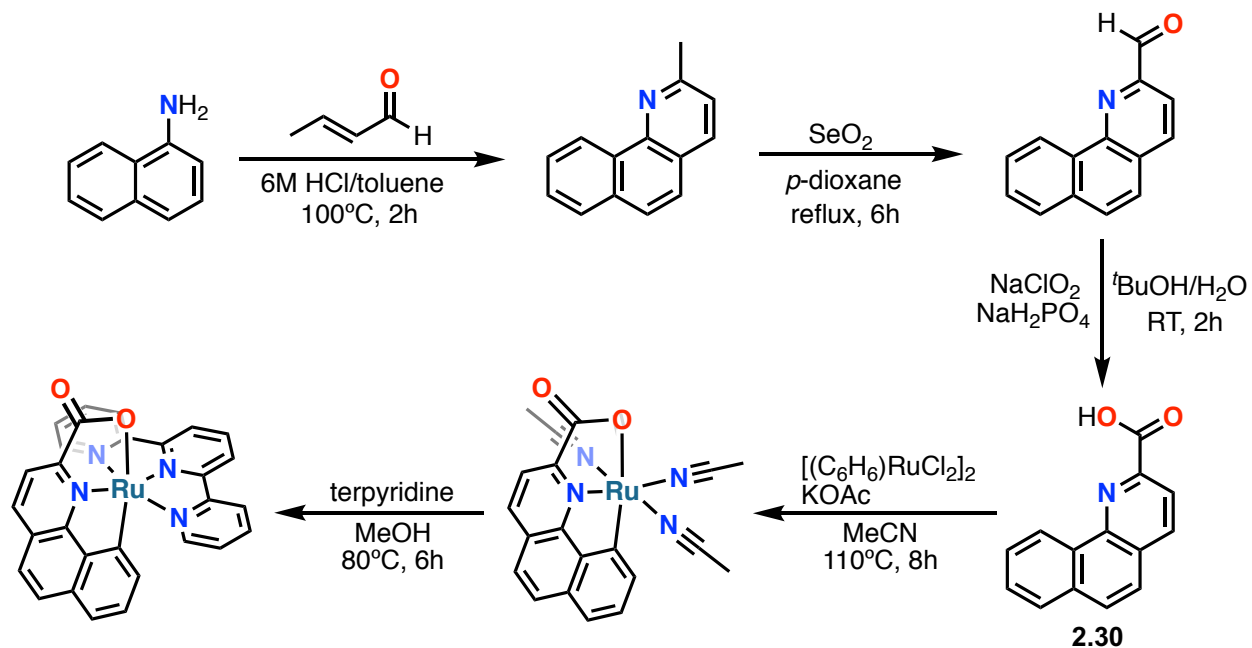


Figure 2. 25 Proposed synthesis for C,N,O analog of 2.6

The carbene containing ligand is more challenging to prepare, but fortunately there already exists literature precedent for its synthesis^{40–43}.

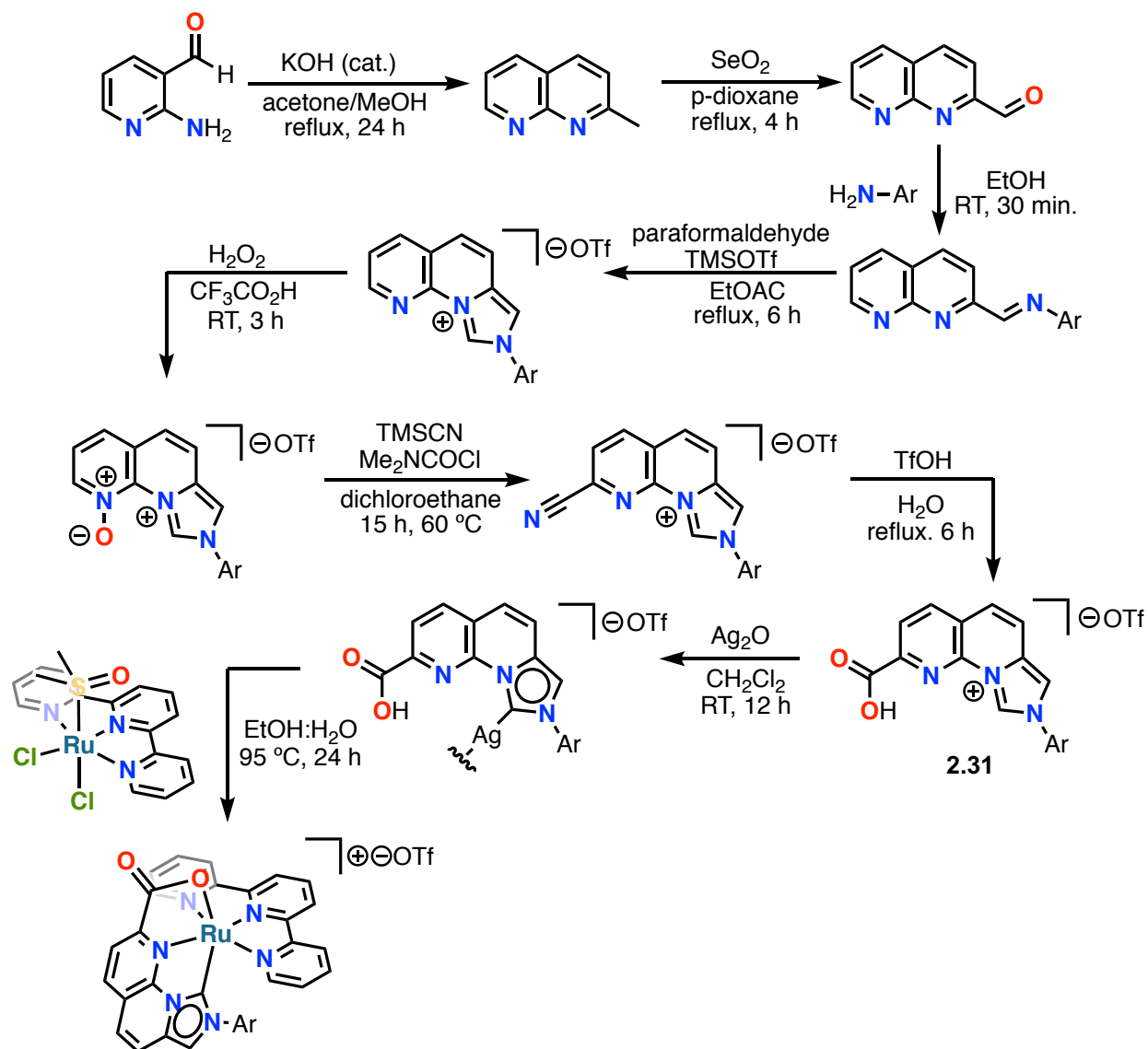
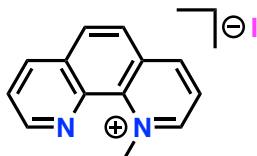


Figure 2. 26 Proposed synthesis for carbene analog of 2.6

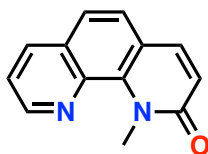
The carbene complex is monocationic and thus may have favorable aqueous solubility over the carbanionic congener. Sulfonate and phosphonate monoester analogs of **2.30** and **2.31** also present attractive targets and may be prepared in a manner similar to the synthesis of **2.18** and **2.22** respectively.

2.10 Experimental Details

The syntheses detailed below were performed by Aaron Nash or by undergraduate student Brett Vincenzini under the supervision of Aaron Nash.

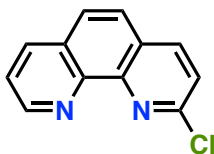


***N*-Methyl-1,10-phenanthroline iodide (2.14):** Into a 150 mL screwcap pressure vessel charged with a stir bar was added 1,10 phenanthroline (20.0130 g, 111.1 mmol, 1.00 equiv) followed by MeCN (100 mL). The suspension was then degassed with N₂ for 30 minutes. Under flowing N₂, MeI (45.600 g, 20 mL) was added dropwise via syringe. The vessel was sealed and then heated at 85 °C for 1.5 h, during which time a large amount of yellow crystalline solid precipitated from a red-orange solution. The mixture was then cooled to room temperature and filtered over a medium porosity glass frit. The collected solids were washed with MeCN (3 x 10 mL) and then Et₂O (3 x 10 mL) to afford a bright yellow crystalline product which was dried in a vacuum oven (60 °C) for 2 h. Yield = 33.4093 g, 94.3%. The ¹H and ¹³C NMR spectra matched those previously published⁴⁴.



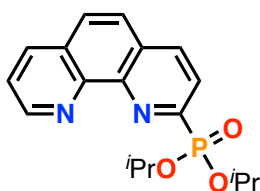
***N*-Methyl-1,10-phenanthrone (2.15):** Into a 250 mL 2 neck roundbottom flask with a stir bar was added *N*-methyl-1,10-phenanthroline iodide (5.0441g, 15.66 mmol,

1.00 equiv), followed by ^tBuOH (67 mL). The vessel was then heated to 40 °C with stirring. KO^tBu (3.4928 g, 31.13 mmol, 1.99 equiv) was then added in 4 portions over 8 minutes. A gentle stream of air was then introduced into the mixture. Stirring and heating was maintained at 40 °C for 4.5 h, over which time the suspension changed in color from a bright yellow to tan. The solvent was then removed via rotary evaporation, and the resulting solids were dry loaded onto SiO₂ (8.0 g) using CH₂Cl₂ as the solvent. The crude product was then subject to flash chromatography (SiO₂, 100.0 g) using hexanes/EtOAc as the gradient (50:50 to 100% EtOAc). The fractions containing pure product (R_f = 0.73) were combined, the solvent removed, and the solids dried in a vacuum oven for 24 h to afford a tan solid. Yield = 2.27 g, 69.0%. The ¹H and ¹³C NMR spectra matched those previously published⁴⁵.



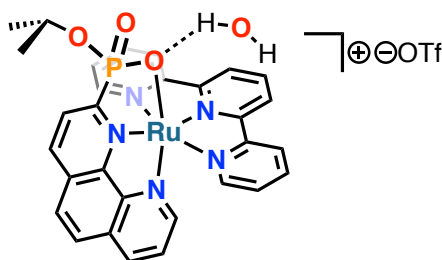
2-chloro-1,10-phenanthroline (2.16): Into a 150 mL pressure vessel charged with a stir bar was added *N*-methyl-1,10-phenanthrone (0.9395 g, 4.469 mmol, 1.00 equiv), followed by POCl₃ (15 mL), xylenes (10 mL), and finally PCl₅ (1.8637 g, 8.950 mmol, 2.00 equiv). The headspace was then flushed with N₂, the vessel sealed, and the mixture heated to 125 °C with stirring for 41 h. The suspension slowly darkened from tan to light grey-brown during this time. The mixture was then removed from heating and allowed to cool to room temperature. The suspension was filtered over a medium porosity glass frit, washed with xylenes (3 x 5 mL), and dried on house vacuum for 30 min. The grey- brown solids were then transferred to a 500 mL Erlenmeyer flask

containing a slurry of ice and 6M NaOH (30 mL). The mixture was stirred until the ice melted and the slight exotherm ceased. CH₂Cl₂ (100 mL) was added to the suspension and the solution gently stirred until all the solids dissolved. The biphasic mixture was then transferred to a separatory funnel and the mixture vigorously shaken. The phases were separated, and the organic layer washed with deionized H₂O (150 mL). The organic phase was dried over Na₂SO₄, filtered over a medium porosity glass frit, and the solvent removed via rotary evaporation. The resultant solids were dried under oil pump vacuum for 24 h to afford a tan solid. Yield = 0.8193 g (85.4%). The ¹H and ¹³C NMR spectra matched those previously published²⁴.



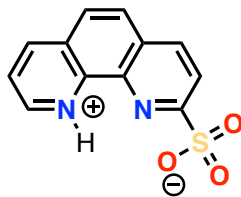
Diisopropyl(1,10-phenanthroline-2-yl)phosphonate (2.17): In an N₂-filled glovebox into a screwcap 48 mL pressure vessel charged with a stir bar was added 2-chloro-1,10-phenanthroline (0.5042g, 2.349 mmol, 1.00 equiv) followed by Pd(OAc)₂ (0.0054 g, 0.0241 mmol, 0.01 equiv), dppf (0.0131g, 0.0236 mmol, 0.01equiv), MeCN (12 mL), diisopropylphosphite (0.4825 g, 2.904 mmol, 1.24 equiv), and ⁱPr₂NEt (0.4013 g, 3.105 mmol, 1.32 equiv). The vessel was sealed and the mixture heated to 110 °C with stirring for 22.5 h. The vessel was then removed from heating and the solvent removed via rotary evaporation. The brown solids so obtained were dry loaded onto SiO₂ (1.5 g) using CH₂Cl₂ (25 mL) as the solvent. The crude product was then subjected to flash chromatography (SiO₂, 20.0 g) using 3% MeOH: CH₂Cl₂ as the mobile phase.

Fractions with $R_f = 0.15$ contained the product. The combined fractions were subject to rotary evaporation to afford the product as a viscous light brown oil that slowly crystallized at room temperature over several months. Yield = 0.6205 g, 71.1%. Elem. anal. calculated for $C_{18}H_{21}N_2O_3P$ (344.35) C 62.78, H 6.15, N 8.14; found: C 58.94, H 7.17, N 7.69. Calculated for $C_{18}H_{21}N_2O_3P + 1.5H_2O$ (371.38): C 58.22, H 6.51, N 7.54. See Table 2.4 for NMR data.

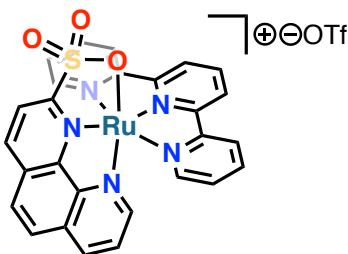


[(terpy)(1,10-phen-2-P(*i*PrO)O₂-κ²N, κO)Ru](OTf) (2.21): In an N₂-filled glovebox into a 150 mL screwcap pressure vessel charged with a stir bar was added diisopropyl(1,10-phenanthroline-2-yl)phosphonate (0.2897 g, 0.867 mmol, 1.00 equiv) followed by NaOH (0.0819 g, 2.048 mmol, 2.36 equiv). Water (9.7 mL) and *i*PrOH (12.8 mL) were added and the vessel sealed and removed from the glovebox. The mixture was heated at 100 °C for 24 h. At this stage NMR analysis of a 1 drop aliquot (¹H, ³¹P in DMSO-*d*₆) showed complete loss of one isopropyl group. The solvent was then removed via rotary evaporation and the pressure vessel taken back into the glovebox. [*cis*-(terpy)Ru(dmsO)Cl₂] (0.4200 g, 0.869 mmol, 1.00 equiv) was added to the residue, followed by EtOH (24.1 mL) and H₂O (5 mL). The vessel was sealed, removed from the glovebox and heated at 75 °C for 24 h. The deep red-brown mixture was then removed from heating and allowed to cool to room temperature. The solvent was removed via

rotary evaporation and the residue dry loaded onto neutral alumina (1.5 g) using CH_2Cl_2 as the solvent. The crude product was then subject to flash chromatography (neutral alumina, 25.0 g) using a $\text{MeOH}:\text{CH}_2\text{Cl}_2$ as the mobile phase. The column was first eluted with 100% CH_2Cl_2 , followed by 3-4% $\text{MeOH}:\text{CH}_2\text{Cl}_2$ gradient (step size 1%). Fractions with $R_f = 0.14$ contained the product. The combined fractions were then subject to rotary evaporation to afford a maroon solid. The solids were then dissolved in MeOH (3 mL) and recrystallized via vapor diffusion (Et_2O into a saturated MeOH solution). After 24h dark red crystals formed which were collected via filtration over a fine glass frit. The crystalline material was then dried in a vacuum oven (60 °C) for 12 h. At this stage 0.1614 g (26.1%) of pure chloride salt was obtained. In an N_2 glovebox the complex was added to a roundbottom flask and then dissolved in MeOH (6 mL). AgOTf (0.0576 g, 0.224 mmol, 1.00 equiv based on the Cl^- complex) was added and the flask was sealed. The mixture was protected from light with a aluminum foil and stirred for 5h at room temperature. The mixture was then filtered over a fine frit and the precipitate washed with MeOH (3 mL). The filtrate was transferred to a 20 mL scintillation vial and the solvent removed via rotary evaporation to afford the pure triflate salt. Yield = 0.1654 g, 22.4%. Elem. anal. calculated for $\text{C}_{31}\text{H}_{25}\text{F}_3\text{N}_5\text{O}_6\text{PRuS}$ (784.76): C 47.45, H 3.21, N 8.93, S 4.09. Found: C 45.04, H 3.87, N 8.63, S 3.35. Calculated for $\text{C}_{31}\text{H}_{25}\text{F}_3\text{N}_5\text{O}_6\text{PRuS} + \text{MeOH} + 2\text{H}_2\text{O}$ (852.74): C, 45.07, H, 3.90, N 8.21, S 3.76. See Table 2.5 for NMR data.



1,10-phenanthroline-2-sulfonate (2.22): Into a 48 mL screwcap pressure vessel charged with a stir bar was added Na₂SO₃ (0.6954 g, 5.517 mmol, 3.94 equiv) and H₂O (3 mL) and stirring until dissolution occurred. The resulting solution was adjusted to pH 7.25 using 6 M HCl and a measured with a pH probe. To this slightly alkaline solution was added 2-chloro-1,10-phenanthroline (0.3004 g, 1.399 mmol, 1.00 equiv) and EtOH (0.5 mL). The pressure vessel was sealed, and the mixture heated at 100 °C with stirring for 42.5 h during which time beige solids precipitated. The mixture was then cooled to room temperature and the pH adjusted to pH 1 with 6 M HCl and pH paper. The mixture was filtered over a fine porosity glass frit, and the collected solids washed with ice cold 6 M HCl. The solids were dried for 24 h on oil pump vacuum to afford the product as tan solid. Yield = 0.2842 g (68%). Elem. anal. Calculated for C₁₂H₈N₂O₃S (260.27): C 55.38, H 3.10, N, 10.76, S 12.32; found C 48.48, H 3.56, N, 9.41, S 10.76. Calculated for C₁₂H₈N₂O₃S + 2H₂O (296.30): C 48.64, H 4.08, N 9.45, S 10.82. See Table 2.6 for NMR data.



[(terpy)(1,10-phen-2-SO₃-κ²N, κO)Ru](OTf) (2.24): In an N₂-filled glovebox into a roundbottom flask charged with a stir bar was added [*cis*-(terpy)Ru(dmsO)Cl₂] (0.1519 g, 0.314 mmol, 1.00 equiv) and AgOTf (0.1643 g, 0.639 mmol, 2.04 equiv) followed by EtOH (8.0 mL) and H₂O (1.0 mL) and the resulting mixture was stirred at room temperature for 30 minutes. The orange-yellow mixture was then filtered through a fine porosity glass frit and the filtrate transferred into a 48 mL screwcap pressure vessel charged with a stir bar. The precipitate was washed thoroughly with EtOH (6 x 1 mL) until the filtrate was almost colorless, and each portion of filtrate was transferred to the pressure vessel. To the orange-yellow solution obtained was added 1,10-phenanthroline-2-sulfonate (0.0953 g, 0.322 mmol, 1.02 equiv) and NaOH (0.0124 g, 0.310 mmol, 0.99 equiv). The pressure vessel was sealed, the vessel brought out of the glovebox, and heated with stirring at 95 °C for 24 h. Over the course of the reaction the color changed from orange-yellow to deep red-orange. The solution was allowed to cool to room temperature, then stored at 4 °C for 19 h. The mixture was then cooled to -20 °C for 1.5 h and filtered in open atmosphere over a medium frit. The red-orange crystalline solids were dried in a 60 °C vacuum oven for 23 h. The now dry solids were washed thoroughly with acetone (10 x 5 mL) until the filtrate was virtually colorless and the filtrate retained. The filtrate was then subject to rotary evaporation to afford a

brick red solid material. The solids so obtained were dried over P_4O_{10} under oil pump vacuum for 26 h to afford pure product as a maroon solid. Yield = 0.1912 g, 80%.

Elem. anal. calculated for $C_{31}H_{25}F_3N_5O_6RuS_2$ (760.69): C 45.28, H 2.44, N 9.43, S 8.63; found C 44.35, H 2.90, N 8.95, S 8.12. Calculated $C_{31}H_{25}F_3N_5O_6RuS_2 + H_2O$ (803.77): C 44.21, H 2.65, N 9.21, S 8.43. IR (ATF): 3547.4, 3463.3 cm^{-1} See Table 2.7 for NMR data.

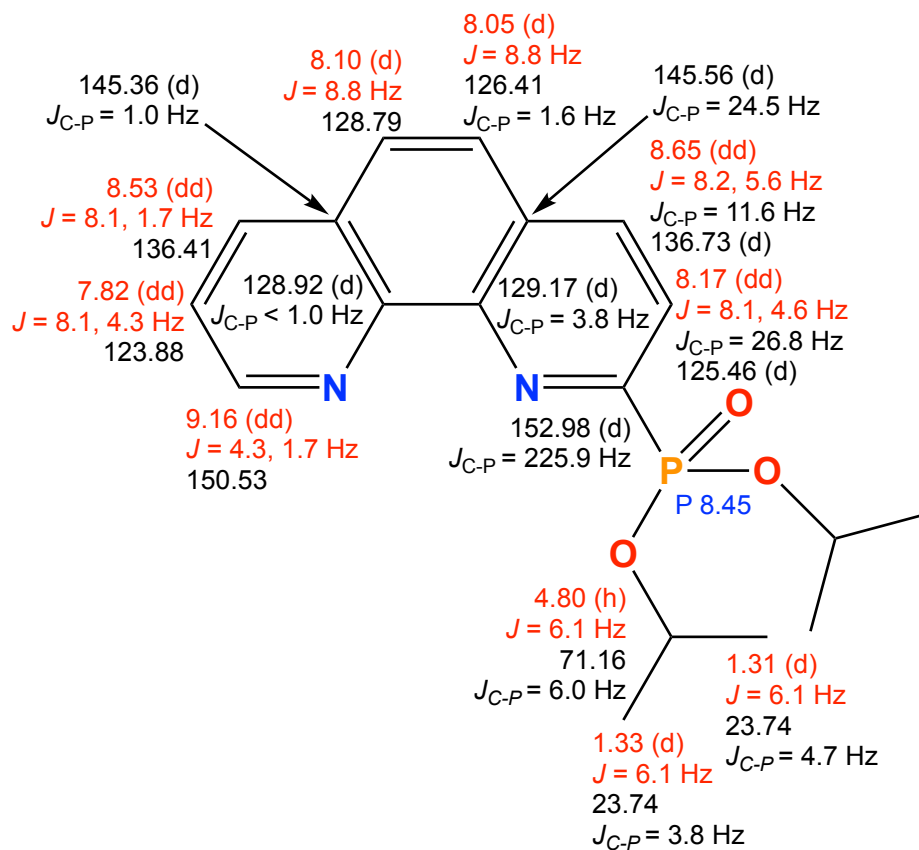


Table 2. 4 2D NMR data for 2.17

gCOSY	gHSQC	
	^1H	^{13}C
9.16 ↔ 7.82	9.16	150.53
9.16 ↔ 8.53	8.65	136.73 (d)
8.65 ↔ 8.17	8.53	136.41
8.53 ↔ 7.82	8.1	128.79
8.10 ↔ 8.05	8.05	126.41
4.80 ↔ 1.33	8.17	125.46 (d)
4.80 ↔ 1.31	7.82	123.88
	4.8	71.16 (d)
	1.33	23.87 (d)
	1.31	23.62 (d)

Table 2.4 (contin.) 2D NMR data for **2.17**

gHMBC		
¹ H	Bonds	¹³ C
9.16	2	123.88
9.16	3	128.92 (d)
9.16	3	136.41
9.16	4	145.36 (d)
8.65	3	126.41
8.65	3	129.17 (d)
8.65	2	145.56 (d)
8.65	3	152.98 (d)
8.53	3	128.92 (d)
8.53	3	128.79
8.53	2	145.36 (d)
8.53	3	150.53
8.17	4	129.17 (d)
8.17	3	145.56 (d)
8.17	2	152.98 (d)
8.1	4	129.17 (d)
8.1	3	128.92 (d)
8.1	3	136.41
8.1	3	145.56 (d)
8.1	2	145.36 (d)
8.05	3	129.17 (d)
8.05	4	128.92 (d)
8.05	3	136.73 (d)
8.05	2	145.56 (d)
8.05	3	145.36 (d)
7.82	4	128.92 (d)
7.82	3	145.36 (d)
7.82	2	150.53
7.82	2	136.41

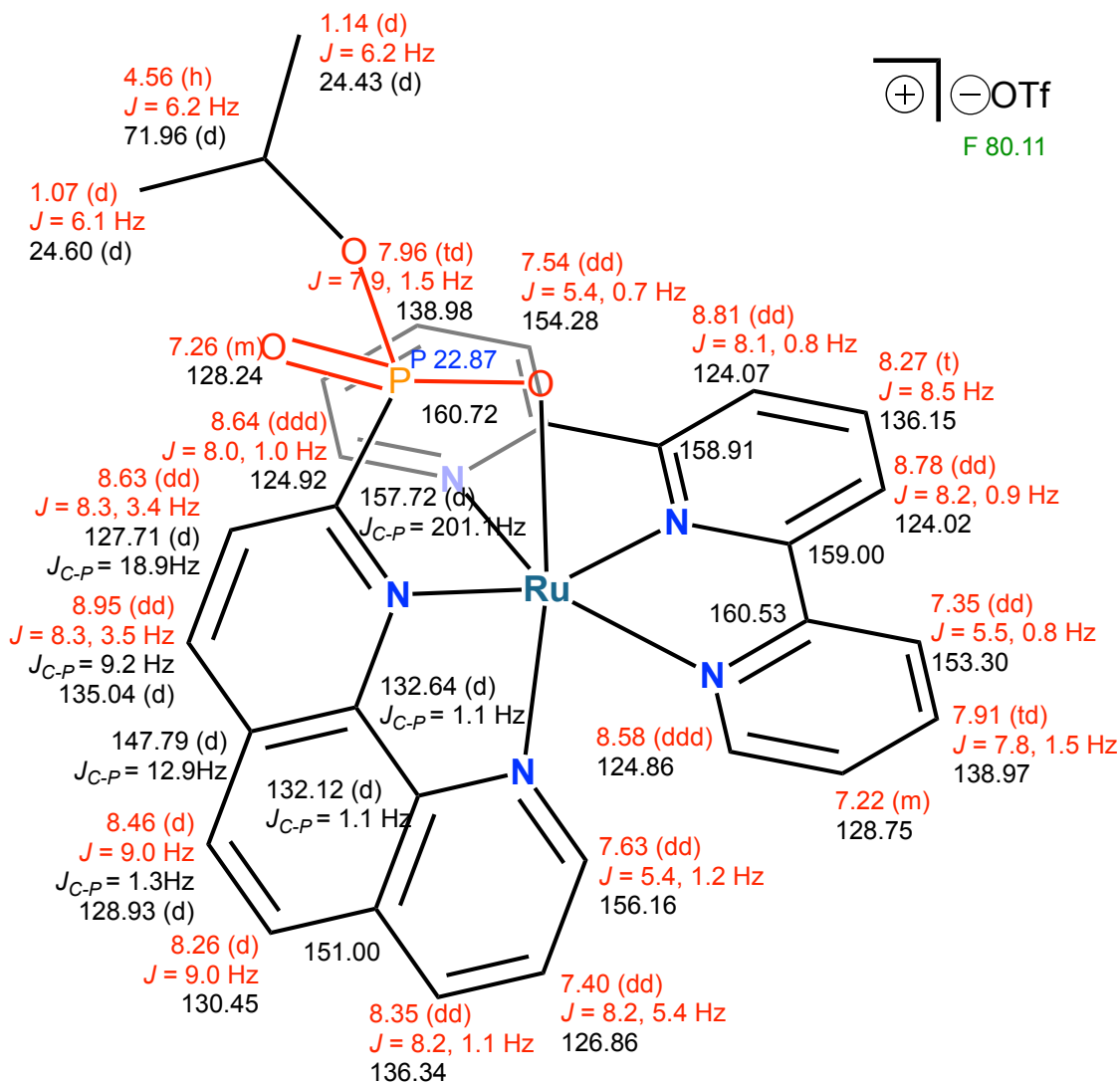


Table 2.5 2D NMR data for 2.21

gCOSY	gCOSY (cont.)	gHSQC		gHSQC (contin.)	
		¹ H	¹³ C	¹ H	¹³ C
8.95 ↔ 8.63	8.35 ↔ 7.63	8.95	135.04 (d)	7.91	138.97
8.81 ↔ 8.27	8.35 ↔ 7.40	8.81	124.07	7.63	156.16
8.81 ↔ 8.78	7.96 ↔ 7.54	8.78	124.02	7.54	154.28
8.78 ↔ 8.27	7.96 ↔ 7.26	8.64	124.92	7.4	126.86
8.64 ↔ 7.96	7.91 ↔ 7.35	8.63	127.71 (d)	7.35	153.3
8.64 ↔ 7.54	7.91 ↔ 7.22	8.58	124.86	7.26	128.24
8.64 ↔ 7.26	7.63 ↔ 7.40	8.46	128.93 (d)	7.22	128.75
8.58 ↔ 7.91	7.54 ↔ 7.26	8.35	136.34	4.54	71.96 (d)
8.58 ↔ 7.35	7.35 ↔ 7.22	8.27	136.15	1.12	24.39 (d)
8.58 ↔ 7.22		8.26	130.45	1.05	24.60 (d)
8.46 ↔ 8.26		7.96	138.98		

Table 2.5 (contin.) 2D NMR data for 2.21

gHMBC			gHMBC (contin.)		
¹ H	Bonds	¹³ C	¹ H	Bonds	¹³ C
8.95	2	147.79 (d)	8.26	3	147.79 (d)
8.95	3	157.72 (d)	8.26	2	151
8.81	3	124.02	7.96	2	154.28
8.81	2	158.91	7.96	3	160.72
8.81	4	159	7.91	2	153.3
8.81	5	160.53	7.91	3	160.53
8.81	3	160.72	7.63	2	126.86
8.78	3	124.07	7.63	3	136.34
8.78	4	158.91	7.63	4	151
8.78	2	159	7.54	3	128.24
8.78	3	160.53	7.54	2	138.98
8.78	5	160.72	7.54	2	160.72
8.64	2	128.24	7.4	4	132.12 (d)
8.64	4,6	158.91	7.4	3	151
8.64	3,5	160.72	7.4	2	156.16
8.63	4	128.93 (d)	7.35	3	128.75
8.63	4	132.64	7.35	2	138.97
8.63	2	157.72 (d)	7.35	2	160.53
8.58	2	128.75	7.26	2	124.92
8.58	4,6	159	7.26	3	154.28
8.58	3,5	160.53	7.22	2	124.86
8.46	2	130.45	7.22	3	153.3
8.46	4	132.12 (d)	1.12	3	24.6
8.46	3	135.04 (d)	1.12	2	71.96 (d)
8.46	2	147.79 (d)	1.05	3	24.39
8.46	3	151	1.05	2	71.96 (d)
8.35	3	130.45			
8.35	3	132.12 (d)			
8.35	2	151			
8.35	3	156.16			
8.27	2	124.02			
8.27	2	124.07			
8.27	3	158.91			
8.27	3	159			
8.27	4	160.53			
8.27	4	160.72			
8.26	2	128.93 (d)			
8.26	3,5	132.12 (d)			
8.26	4	132.64 (d)			
8.26	3	136.34			

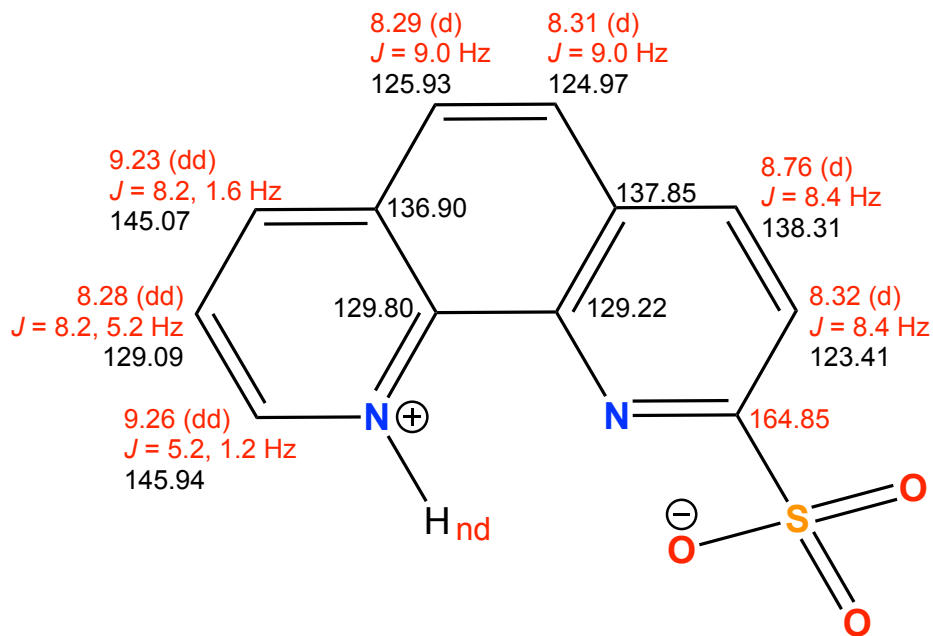


Table 2. 6 2D NMR data for **2.22**

gCOSY	gHSQC	
	^1H	^{13}C
9.14 ↔ 8.68	9.14	136.16
8.97 ↔ 8.43	8.97	124.16
8.74 ↔ 7.32	8.74	124.81
8.74 ↔ 8.03	8.68	122.44
8.60 ↔ 8.37	8.6	128.62
8.48 ↔ 7.50	8.48	136.43
8.03 ↔ 7.32	8.43	136.43
7.79 ↔ 7.50	8.37	130.27
7.70 ↔ 7.32	8.03	138.98
	7.79	156.87
	7.70	154.44
	7.50	126.84
	7.32	128.23

Table 2.6 (contin.) 2D NMR data for **2.22**

gHMBC			gHMBC (contin.)		
¹H	Bonds	¹³C	¹H	Bonds	¹³C
9.14	2	122.44	7.7	3	128.23
9.14	3	161.03	7.7	3	158.87
9.14	2	154.46	7.7	4	124.81
9.14	3	132.08	7.5	2	156.87
8.97	2	136.43	7.5	2	136.43
8.97	2	158.87	7.5	3	150.61
8.97	3	160.08	7.5	4	131.74
8.74	2	128.23	7.32	2	138.98
8.74	3	138.98	7.32	2	124.81
8.74	4	154.44	7.32	3	154.44
8.68	2	161.03	7.32	4	160.08
8.68	2	136.16			
8.68	3	154.46			
8.68	4	132.08			
8.60	2	154.46			
8.60	2	130.27			
8.60	3	132.08			
8.60	3	150.61			
8.60	4	131.74			
8.48	2	150.61			
8.48	2	126.84			
8.48	3	156.87			
8.48	3	131.74			
8.43	2	124.16			
8.43	3	158.87			
8.43	4	160.08			
8.37	2	150.61			
8.37	2	128.62			
8.37	3	131.74			
8.37	3	154.46			
8.37	4	132.08			
8.03	2	154.44			
8.03	2	128.23			
8.03	3	124.81			
8.03	3	160.08			
7.79	2	126.84			
7.79	3	136.43			
7.79	4	150.61			
7.79	5	131.74			
7.70	2	160.08			
7.70	2	138.98			

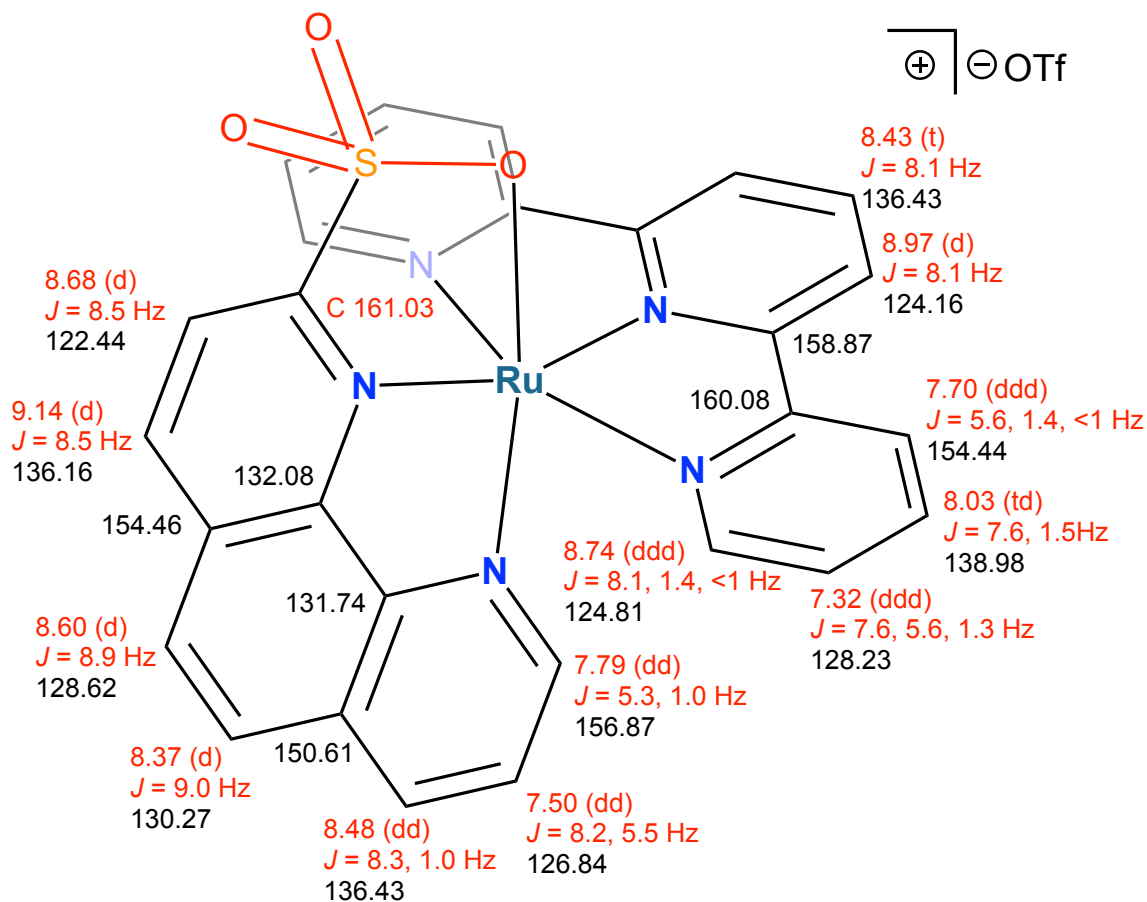


Table 2.7 2D NMR data for **2.24**

gCOSY		gHSQC	
		^1H	^{13}C
9.14	↔	8.68	136.16
8.97	↔	8.43	124.16
8.74	↔	7.32	124.81
8.74	↔	8.03	122.44
8.60	↔	8.37	128.62
8.48	↔	7.50	136.43
8.03	↔	7.32	136.43
7.79	↔	7.50	138.98
7.70	↔	7.32	128.23

Table 2.7 (contin.) 2D NMR data for 2.24

gHMBC			gHMBC (contin.)		
¹ H	Bonds	¹³ C	¹ H	Bonds	¹³ C
9.14	2	122.44	7.70	2	138.98
9.14	3	161.03	7.70	3	128.23
9.14	2	154.46	7.70	3	158.87
9.14	3	132.08	7.70	4	124.81
8.97	2	136.43	7.50	2	156.87
8.97	2	158.87	7.50	2	136.43
8.97	3	160.08	7.50	3	150.61
8.74	2	128.23	7.50	4	131.74
8.74	3	138.98	7.32	2	138.98
8.74	4	154.44	7.32	2	124.81
8.68	2	161.03	7.32	3	154.44
8.68	2	136.16	7.32	4	160.08
8.68	3	154.46			
8.68	4	132.08			
8.60	2	154.46			
8.60	2	130.27			
8.60	3	132.08			
8.60	3	150.61			
8.60	4	131.74			
8.48	2	150.61			
8.48	2	126.84			
8.48	3	156.87			
8.48	3	131.74			
8.43	2	124.16			
8.43	3	158.87			
8.43	4	160.08			
8.37	2	150.61			
8.37	2	128.62			
8.37	3	131.74			
8.37	3	154.46			
8.37	4	132.08			
8.03	2	154.44			
8.03	2	128.23			
8.03	3	124.81			
8.03	3	160.08			
7.79	2	126.84			
7.79	3	136.43			
7.79	4	150.61			
7.79	5	131.74			
7.70	2	160.08			

Table 2. 8 Crystallographic information for **2.21-BARF**

Empirical Formula	C ₅₄ H ₂₇ B F ₂₀ N ₅ O ₄ P Ru	
Formula weight	1332.65	
Temperature (K)	100.15	
Wavelength (Å)	1.54184	
Space group	C 2/c (no. 15)	
Unit cell dimensions	a (Å) = 35.06(5)	α (°) = 90
	b (Å) = 10.938(18)	β (°) = 121.29(2)
	c (Å) = 34.60(5)	γ (°) = 90
Volume (Å³)	11340(28)	
Z	8	
Density (calculated) Mg/m ³	1.561	
μ (mm ⁻¹)	3.551	
F(000)	5296	
Crystal size mm ³	0.29 x 0.1 x 0.08	
Theta range for data collection	2.911 to 68.031°.	
Index ranges	-40 ≤ h ≤ 42	
	-12 ≤ k ≤ 11	
	-41 ≤ l ≤ 41	
Reflections collected	43423	
Independent reflections	10254 [R(int) = 0.0624]	
Completeness to theta = 25.242°	99.70%	
Absorption correction	Semi-empirical from equivalents	
Max. and min. transmission	0.7531 and 0.5891	
Refinement method	Full-matrix least-squares on F ²	
Data / restraints / parameters	10254 / 0 / 780	
Goodness-of-fit on F²	1.042	
Final R indices [I>2σ(I)]	R1 = 0.0523, wR2 = 0.1246	
R indices (all data)	R1 = 0.0704, wR2 = 0.1337	
Extinction coefficient	n/a	
Largest diff. peak and hole	1.526 and -0.624	
SQUEEZE	Found: 264e/uc. (likely eight CH ₂ Cl ₂)	

Table 2. 9 Atomic coordinates ($\times 10^4$) and equivalent isotropic displacement parameters ($\text{\AA}^2 \times 10^3$) for **2.21-BARF**. $U(\text{eq})$ is defined as one third of the trace of the orthogonalized U^{ij} tensor.

	x	y	z	U(eq)
Ru(1)	7262(1)	4553(1)	3943(1)	26(1)
P(1)	6779(1)	2344(1)	3291(1)	33(1)
F(5)	4084(1)	9126(2)	3350(1)	32(1)
F(1)	5581(1)	10600(2)	4153(1)	32(1)
F(14)	4861(1)	4160(2)	3119(1)	35(1)
F(15)	5061(1)	5621(2)	3826(1)	31(1)
F(2)	5277(1)	12866(2)	3999(1)	35(1)
F(11)	4515(1)	9045(2)	2832(1)	34(1)
F(13)	4466(1)	5107(2)	2266(1)	36(1)
F(3)	4375(1)	13343(2)	3547(1)	37(1)
F(20)	5670(1)	6861(2)	4730(1)	37(1)
F(6)	5348(1)	9111(2)	4752(1)	35(1)
F(4)	3787(1)	11426(2)	3218(1)	37(1)
F(10)	4199(1)	6559(2)	3642(1)	38(1)
F(16)	5518(1)	9030(2)	3465(1)	34(1)
F(12)	4295(1)	7562(2)	2138(1)	40(1)
F(17)	6394(1)	8756(3)	3797(1)	44(1)
F(19)	6540(1)	6737(2)	5076(1)	43(1)
F(18)	6923(1)	7644(3)	4620(1)	51(1)
F(7)	5081(1)	8569(3)	5326(1)	54(1)
O(3)	7173(1)	2633(3)	3771(1)	34(1)
F(9)	3919(1)	6102(3)	4206(1)	60(1)
O(1)	6353(1)	2244(3)	3343(1)	38(1)
F(8)	4348(1)	7082(3)	5057(1)	65(1)
N(5)	6869(1)	4726(3)	3262(1)	27(1)
O(2)	6824(1)	1299(3)	3049(1)	41(1)
N(2)	7636(1)	4353(3)	4609(1)	28(1)
N(3)	6771(1)	4518(3)	4109(1)	31(1)
N(4)	7265(1)	6428(3)	3886(1)	30(1)
N(1)	7900(1)	4533(3)	4036(1)	34(1)
C(36)	4398(1)	10034(4)	3516(1)	27(1)
C(52)	4574(1)	5852(4)	2620(1)	29(1)
C(50)	4871(1)	6150(4)	3410(1)	25(1)
C(34)	4529(1)	12192(4)	3607(1)	28(1)
C(33)	4978(1)	11942(3)	3834(1)	27(1)
C(31)	4849(1)	9715(3)	3744(1)	25(1)

Table 2.9 (contin.) Atomic coordinates ($\times 10^4$) and equivalent isotropic displacement parameters ($\text{\AA}^2 \times 10^3$) for **2.21-BARF**. $U(\text{eq})$ is defined as one third of the trace of the orthogonalized U^{ij} tensor.

	x	y	z	U(eq)
C(49)	4796(1)	7405(3)	3372(1)	24(1)
C(54)	4603(1)	7842(4)	2929(1)	29(1)
C(27)	6809(1)	5887(4)	3103(1)	27(1)
C(10)	7422(2)	4200(3)	4841(1)	31(1)
C(32)	5128(1)	10736(4)	3900(1)	27(1)
C(26)	7022(1)	6817(4)	3441(1)	28(1)
C(19)	6683(1)	3786(4)	2976(1)	31(1)
C(53)	4490(1)	7091(4)	2558(1)	29(1)
C(35)	4234(1)	11212(4)	3448(1)	27(1)
C(22)	6563(1)	6167(4)	2643(1)	29(1)
C(37)	4801(1)	7833(4)	4169(1)	29(1)
C(42)	4994(2)	8331(4)	4604(1)	33(1)
C(11)	6932(2)	4312(3)	4558(1)	29(1)
C(43)	5544(1)	8022(3)	4088(1)	26(1)
C(21)	6377(1)	5169(4)	2341(1)	32(1)
C(47)	6214(2)	8312(4)	4029(2)	34(1)
C(5)	8234(1)	4465(4)	4485(2)	36(1)
C(44)	5826(1)	7410(4)	4488(1)	29(1)
C(51)	4770(1)	5368(4)	3052(1)	28(1)
C(30)	7489(1)	7283(4)	4204(1)	33(1)
C(38)	4436(2)	7088(4)	4057(1)	32(1)
C(6)	8086(1)	4283(3)	4809(2)	31(1)
C(23)	6521(1)	7440(4)	2518(2)	34(1)
C(25)	6992(1)	8048(4)	3312(2)	31(1)
C(20)	6440(1)	3991(4)	2508(1)	32(1)
C(48)	5758(1)	8439(4)	3864(1)	31(1)
C(9)	7671(2)	3933(4)	5305(1)	34(1)
C(12)	6644(2)	4210(4)	4722(2)	36(1)
C(46)	6478(2)	7755(4)	4443(2)	38(1)
C(45)	6286(2)	7302(4)	4672(1)	34(1)
C(24)	6725(1)	8337(4)	2837(2)	35(1)
C(28)	7233(2)	8912(4)	3661(2)	36(1)
C(8)	8130(2)	3850(4)	5513(2)	36(1)
C(7)	8342(2)	4025(4)	5272(2)	38(1)
C(29)	7478(2)	8516(4)	4096(2)	38(1)
C(13)	6186(2)	4343(4)	4424(2)	40(1)

Table 2.9 (contin). Atomic coordinates ($\times 10^4$) and equivalent isotropic displacement parameters ($\text{\AA}^2 \times 10^3$) for **2.21-BARF**. $U(\text{eq})$ is defined as one third of the trace of the orthogonalized U^{ij} tensor.

	x	y	z	U(eq)
C(15)	6326(2)	4663(4)	3830(2)	37(1)
C(1)	8010(2)	4678(4)	3722(2)	43(1)
C(41)	4859(2)	8077(4)	4905(2)	40(1)
C(14)	6025(2)	4567(4)	3978(2)	42(1)
C(17)	5957(2)	1471(4)	3068(2)	40(1)
C(18)	5744(2)	1759(4)	2571(2)	45(1)
C(16)	5646(2)	1752(5)	3241(2)	48(1)
C(39)	4281(2)	6824(4)	4343(2)	42(1)
C(4)	8682(2)	4576(4)	4613(2)	45(1)
C(40)	4498(2)	7317(5)	4774(2)	47(1)
C(3)	8791(2)	4737(5)	4288(2)	54(1)
B(02D)	4993(2)	8245(4)	3838(2)	25(1)

Table 2. 10 Bond lengths [Å] for **2.21-BARF**

Ru(1)-O(3)	2.161(4)
Ru(1)-N(5)	2.030(4)
Ru(1)-N(2)	1.983(4)
Ru(1)-N(3)	2.080(4)
Ru(1)-N(4)	2.061(5)
Ru(1)-N(1)	2.088(5)
P(1)-O(3)	1.545(3)
P(1)-O(1)	1.602(4)
P(1)-O(2)	1.472(4)
P(1)-C(19)	1.845(5)
F(5)-C(36)	1.369(5)
F(1)-C(32)	1.366(5)
F(14)-C(51)	1.351(5)
F(15)-C(50)	1.362(5)
F(2)-C(33)	1.349(5)
F(11)-C(54)	1.354(5)
F(13)-C(52)	1.353(5)
F(3)-C(34)	1.344(5)
F(20)-C(44)	1.356(5)
F(6)-C(42)	1.367(5)
F(4)-C(35)	1.360(5)
F(10)-C(38)	1.361(5)
F(16)-C(48)	1.351(5)
F(12)-C(53)	1.345(5)
F(17)-C(47)	1.343(5)
F(19)-C(45)	1.355(5)
F(18)-C(46)	1.353(6)
F(7)-C(41)	1.355(6)
F(9)-C(39)	1.356(6)
O(1)-C(17)	1.475(6)
F(8)-C(40)	1.352(5)
N(5)-C(27)	1.356(5)
N(5)-C(19)	1.338(5)
N(2)-C(10)	1.365(6)
N(2)-C(6)	1.356(6)
N(3)-C(11)	1.366(6)
N(3)-C(15)	1.352(6)

Table 2.10 (contin.) Bond lengths [Å] for **2.21-BARF**

C(5)-C(4)	1.397(7)
C(44)-C(45)	1.398(6)
C(30)-C(29)	1.394(7)
C(38)-C(39)	1.384(6)
C(6)-C(7)	1.402(6)
C(23)-C(24)	1.368(7)
C(25)-C(24)	1.442(6)
C(25)-C(28)	1.417(6)
C(9)-C(8)	1.383(7)
C(12)-C(13)	1.394(7)
C(46)-C(45)	1.372(7)
C(28)-C(29)	1.361(7)
C(8)-C(7)	1.387(7)
C(13)-C(14)	1.364(7)
C(15)-C(14)	1.394(7)
C(1)-C(2)	1.401(8)
C(41)-C(40)	1.380(8)
C(17)-C(18)	1.511(7)
C(17)-C(16)	1.522(7)
C(39)-C(40)	1.383(7)
C(4)-C(3)	1.375(8)
C(3)-C(2)	1.383(8)
N(4)-C(26)	1.383(6)
N(4)-C(30)	1.343(6)
N(1)-C(5)	1.378(6)
N(1)-C(1)	1.337(6)
C(36)-C(31)	1.394(6)
C(36)-C(35)	1.381(6)
C(52)-C(53)	1.380(6)
C(52)-C(51)	1.386(6)
C(50)-C(49)	1.391(6)
C(50)-C(51)	1.390(6)
C(34)-C(33)	1.373(6)
C(34)-C(35)	1.389(6)
C(33)-C(32)	1.394(6)
C(31)-C(32)	1.396(6)
C(31)-B(02D)	1.666(6)
C(49)-C(54)	1.398(6)

Table 2.10 (contin.) Bond lengths [Å] for **2.21-BARF**

C(49)-B(02D)	1.663(6)
C(54)-C(53)	1.397(6)
C(27)-C(26)	1.433(6)
C(27)-C(22)	1.396(6)
C(10)-C(11)	1.476(6)
C(10)-C(9)	1.404(6)
C(26)-C(25)	1.405(6)
C(19)-C(20)	1.402(6)
C(22)-C(21)	1.415(6)
C(22)-C(23)	1.443(6)
C(37)-C(42)	1.399(6)
C(37)-C(38)	1.392(6)
C(37)-B(02D)	1.664(6)
C(42)-C(41)	1.381(6)
C(11)-C(12)	1.397(6)
C(43)-C(44)	1.386(6)
C(43)-C(48)	1.404(6)
C(43)-B(02D)	1.677(6)
C(21)-C(20)	1.383(6)
C(47)-C(48)	1.398(6)
C(47)-C(46)	1.380(7)
C(5)-C(6)	1.472(7)

Table 2. 11 Bond angles [°] for **2.21-BARF**

N(5)-Ru(1)-N(3)	99.33(16)
N(5)-Ru(1)-N(4)	80.20(13)
N(5)-Ru(1)-N(1)	101.93(15)
N(2)-Ru(1)-O(3)	97.29(13)
N(2)-Ru(1)-N(5)	178.54(14)
N(2)-Ru(1)-N(3)	79.62(17)
N(2)-Ru(1)-N(4)	100.88(13)
N(2)-Ru(1)-N(1)	79.12(16)
N(3)-Ru(1)-O(3)	92.14(13)
N(3)-Ru(1)-N(1)	158.74(15)
N(4)-Ru(1)-O(3)	161.35(13)
N(4)-Ru(1)-N(3)	95.24(13)
N(4)-Ru(1)-N(1)	88.08(14)
N(1)-Ru(1)-O(3)	91.23(13)
O(3)-P(1)-O(1)	104.9(2)
O(3)-P(1)-C(19)	104.30(19)
O(1)-P(1)-C(19)	103.26(19)
O(2)-P(1)-O(3)	118.00(19)
O(2)-P(1)-O(1)	113.20(19)
O(2)-P(1)-C(19)	111.8(2)
P(1)-O(3)-Ru(1)	114.62(17)
C(17)-O(1)-P(1)	125.9(3)
C(27)-N(5)-Ru(1)	115.2(3)
C(19)-N(5)-Ru(1)	124.3(3)
C(19)-N(5)-C(27)	120.5(4)
C(10)-N(2)-Ru(1)	117.6(3)
C(6)-N(2)-Ru(1)	119.4(3)
C(6)-N(2)-C(10)	122.8(4)
C(11)-N(3)-Ru(1)	113.8(3)
C(15)-N(3)-Ru(1)	127.9(3)
C(15)-N(3)-C(11)	118.3(4)
C(26)-N(4)-Ru(1)	112.5(3)
C(30)-N(4)-Ru(1)	130.1(3)
C(30)-N(4)-C(26)	117.2(4)
C(5)-N(1)-Ru(1)	112.9(3)
C(1)-N(1)-Ru(1)	127.7(3)
C(1)-N(1)-C(5)	119.2(4)

Table 2.11 (contin.) Bond angles [°] for **2.21-BARF**

F(5)-C(36)-C(31)	119.0(4)
F(5)-C(36)-C(35)	115.5(4)
C(35)-C(36)-C(31)	125.4(4)
F(13)-C(52)-C(53)	120.9(4)
F(13)-C(52)-C(51)	119.8(4)
C(53)-C(52)-C(51)	119.3(4)
F(15)-C(50)-C(49)	118.9(3)
F(15)-C(50)-C(51)	116.0(4)
C(51)-C(50)-C(49)	125.1(4)
F(3)-C(34)-C(33)	121.7(4)
F(3)-C(34)-C(35)	120.3(4)
C(33)-C(34)-C(35)	118.0(4)
F(2)-C(33)-C(34)	120.0(4)
F(2)-C(33)-C(32)	119.7(4)
C(34)-C(33)-C(32)	120.3(4)
C(36)-C(31)-C(32)	112.3(4)
C(36)-C(31)-B(02D)	119.4(3)
C(32)-C(31)-B(02D)	128.1(4)
C(50)-C(49)-C(54)	113.6(3)
C(50)-C(49)-B(02D)	119.4(3)
C(54)-C(49)-B(02D)	126.5(4)
F(11)-C(54)-C(49)	121.5(3)
F(11)-C(54)-C(53)	115.0(4)
C(53)-C(54)-C(49)	123.4(4)
N(5)-C(27)-C(26)	115.4(4)
N(5)-C(27)-C(22)	122.8(4)
C(22)-C(27)-C(26)	121.8(4)
N(2)-C(10)-C(11)	113.8(4)
N(2)-C(10)-C(9)	119.6(4)
C(9)-C(10)-C(11)	126.5(4)
F(1)-C(32)-C(33)	115.0(3)
F(1)-C(32)-C(31)	120.6(4)
C(33)-C(32)-C(31)	124.4(4)
N(4)-C(26)-C(27)	116.6(4)
N(4)-C(26)-C(25)	123.4(4)
C(25)-C(26)-C(27)	119.9(4)
N(5)-C(19)-P(1)	110.6(3)

Table 2.11 (contin.) Bond angles [°] for **2.21-BARF**

N(5)-C(19)-C(20)	120.0(4)
C(20)-C(19)-P(1)	129.3(3)
N(2)-C(6)-C(5)	112.4(4)
N(2)-C(6)-C(7)	118.6(4)
C(7)-C(6)-C(5)	129.0(4)
C(24)-C(23)-C(22)	121.4(4)
C(26)-C(25)-C(24)	118.1(4)
C(26)-C(25)-C(28)	117.0(4)
C(28)-C(25)-C(24)	124.9(4)
C(21)-C(20)-C(19)	120.1(4)
F(16)-C(48)-C(43)	119.5(4)
F(16)-C(48)-C(47)	115.9(4)
C(47)-C(48)-C(43)	124.6(4)
C(8)-C(9)-C(10)	118.2(4)
C(13)-C(12)-C(11)	119.4(4)
F(18)-C(46)-C(47)	120.3(4)
F(18)-C(46)-C(45)	120.2(4)
C(45)-C(46)-C(47)	119.5(4)
F(19)-C(45)-C(44)	119.6(4)
F(19)-C(45)-C(46)	120.2(4)
C(46)-C(45)-C(44)	120.3(4)
C(23)-C(24)-C(25)	121.3(4)
C(29)-C(28)-C(25)	119.1(4)
C(9)-C(8)-C(7)	121.4(4)
C(8)-C(7)-C(6)	119.4(4)
C(28)-C(29)-C(30)	121.2(4)
C(14)-C(13)-C(12)	119.7(4)
N(3)-C(15)-C(14)	122.8(4)
N(1)-C(1)-C(2)	121.8(5)
F(7)-C(41)-C(42)	120.0(5)
F(7)-C(41)-C(40)	120.6(4)
C(40)-C(41)-C(42)	119.4(4)
C(13)-C(14)-C(15)	118.8(5)
O(1)-C(17)-C(18)	111.0(4)
O(1)-C(17)-C(16)	104.8(4)
C(18)-C(17)-C(16)	112.0(4)
F(9)-C(39)-C(38)	120.9(4)

Table 2.11 (contin.) Bond angles [°] for **2.21-BARF**

F(9)-C(39)-C(40)	119.6(4)
C(40)-C(39)-C(38)	119.4(5)
C(3)-C(4)-C(5)	119.8(5)
F(8)-C(40)-C(41)	120.8(5)
F(8)-C(40)-C(39)	120.2(5)
C(41)-C(40)-C(39)	119.0(4)
C(4)-C(3)-C(2)	119.3(5)
C(31)-B(02D)-C(43)	113.1(3)
C(49)-B(02D)-C(31)	114.4(3)
C(49)-B(02D)-C(37)	113.9(3)
C(49)-B(02D)-C(43)	101.9(3)
C(37)-B(02D)-C(31)	101.9(3)
C(37)-B(02D)-C(43)	112.1(3)
C(3)-C(2)-C(1)	119.2(5)

Symmetry transformations used to generate equivalent atoms:

Table 2. 12 Anisotropic displacement parameters ($\text{\AA}^2 \times 10^3$) for **2.21-BARF**. The anisotropic displacement factor exponent takes the form: $-2\pi^2[h^2a^{*2}U^{11} + \dots + 2hka^*b^*U^{12}]$

	U^{11}	U^{22}	U^{33}	U^{23}	U^{13}	U^{12}
Ru(1)	26(1)	23(1)	22(1)	1(1)	8(1)	-3(1)
P(1)	38(1)	25(1)	31(1)	2(1)	15(1)	1(1)
F(5)	30(1)	29(1)	33(1)	-3(1)	13(1)	-4(1)
F(1)	25(1)	30(1)	32(1)	-5(1)	7(1)	-3(1)
F(14)	44(2)	22(1)	34(1)	-4(1)	18(1)	0(1)
F(15)	39(1)	25(1)	25(1)	2(1)	13(1)	2(1)
F(2)	35(1)	26(1)	36(1)	-3(1)	12(1)	-7(1)
F(11)	49(2)	25(1)	26(1)	4(1)	18(1)	4(1)
F(13)	43(2)	34(1)	26(1)	-9(1)	15(1)	-3(1)
F(3)	42(2)	24(1)	39(1)	5(1)	18(1)	8(1)
F(20)	38(1)	36(1)	30(1)	5(1)	14(1)	5(1)
F(6)	42(1)	32(1)	25(1)	-8(1)	12(1)	-1(1)
F(4)	29(1)	36(1)	41(1)	6(1)	15(1)	4(1)
F(10)	40(1)	42(1)	35(1)	-7(1)	21(1)	-12(1)
F(16)	35(1)	36(1)	30(1)	1(1)	17(1)	-1(1)
F(12)	53(2)	40(1)	21(1)	4(1)	15(1)	4(1)
F(17)	35(2)	57(2)	46(2)	-8(1)	25(1)	-7(1)
F(19)	37(1)	45(2)	32(1)	0(1)	6(1)	9(1)
F(18)	28(1)	71(2)	44(2)	-8(1)	13(1)	4(1)
F(7)	82(2)	55(2)	29(1)	-1(1)	32(2)	13(2)
O(3)	42(2)	25(2)	33(2)	-5(1)	18(1)	-10(1)
F(9)	64(2)	64(2)	71(2)	2(2)	50(2)	-15(2)
O(1)	38(2)	34(2)	35(2)	-2(1)	16(1)	-4(1)
F(8)	94(3)	75(2)	57(2)	8(2)	61(2)	3(2)
N(5)	29(2)	26(2)	21(2)	4(1)	11(1)	2(1)
O(2)	48(2)	30(2)	40(2)	3(1)	18(2)	5(1)
N(2)	30(2)	18(2)	26(2)	2(1)	8(1)	-1(1)
N(3)	33(2)	29(2)	29(2)	-2(2)	16(2)	-4(2)
N(4)	31(2)	27(2)	26(2)	2(1)	11(2)	1(1)
N(1)	34(2)	26(2)	42(2)	3(2)	21(2)	1(2)
C(36)	33(2)	26(2)	25(2)	-3(2)	17(2)	-7(2)
C(52)	30(2)	34(2)	22(2)	-10(2)	14(2)	-6(2)
C(50)	24(2)	28(2)	20(2)	-2(2)	10(2)	-1(2)
C(34)	36(2)	23(2)	25(2)	3(2)	17(2)	2(2)
C(33)	36(2)	22(2)	21(2)	-3(2)	13(2)	-5(2)
C(31)	29(2)	25(2)	20(2)	-3(2)	12(2)	-3(2)

Table 2.12 (contin.) Anisotropic displacement parameters ($\text{\AA}^2 \times 10^3$) for **2.21-BARF**. The anisotropic displacement factor exponent takes the form: $-2\pi^2[h^2a^2U^{11} + \dots + 2hkab^*U^{12}]$

	U^{11}	U^{22}	U^{33}	U^{23}	U^{13}	U^{12}
C(49)	23(2)	26(2)	24(2)	-1(2)	12(2)	-5(2)
C(54)	30(2)	28(2)	27(2)	-1(2)	13(2)	-1(2)
C(27)	26(2)	26(2)	29(2)	2(2)	14(2)	2(2)
C(10)	40(2)	18(2)	30(2)	-1(2)	16(2)	-3(2)
C(32)	26(2)	33(2)	19(2)	-3(2)	10(2)	-1(2)
C(26)	26(2)	26(2)	30(2)	-2(2)	14(2)	-1(2)
C(19)	34(2)	23(2)	28(2)	2(2)	12(2)	-1(2)
C(53)	32(2)	31(2)	23(2)	1(2)	13(2)	-1(2)
C(35)	28(2)	30(2)	23(2)	2(2)	14(2)	3(2)
C(22)	26(2)	28(2)	29(2)	2(2)	12(2)	0(2)
C(37)	37(2)	25(2)	26(2)	3(2)	17(2)	5(2)
C(42)	42(3)	30(2)	27(2)	2(2)	17(2)	10(2)
C(11)	39(2)	17(2)	28(2)	-2(2)	15(2)	-2(2)
C(43)	28(2)	23(2)	26(2)	-7(2)	12(2)	0(2)
C(21)	32(2)	31(2)	26(2)	6(2)	11(2)	1(2)
C(47)	36(2)	34(2)	35(2)	-10(2)	19(2)	-4(2)
C(5)	30(2)	23(2)	44(3)	-1(2)	11(2)	-1(2)
C(44)	35(2)	24(2)	26(2)	-5(2)	15(2)	-2(2)
C(51)	27(2)	23(2)	30(2)	0(2)	13(2)	0(2)
C(30)	29(2)	34(2)	27(2)	-3(2)	9(2)	-2(2)
C(38)	36(2)	33(2)	27(2)	-2(2)	17(2)	0(2)
C(6)	31(2)	18(2)	34(2)	1(2)	9(2)	0(2)
C(23)	32(2)	31(2)	33(2)	9(2)	12(2)	4(2)
C(25)	28(2)	24(2)	40(2)	2(2)	17(2)	3(2)
C(20)	34(2)	30(2)	28(2)	-2(2)	13(2)	-3(2)
C(48)	32(2)	25(2)	29(2)	-7(2)	11(2)	-1(2)
C(9)	44(3)	23(2)	30(2)	-1(2)	15(2)	0(2)
C(12)	54(3)	23(2)	36(2)	-4(2)	27(2)	-4(2)
C(46)	30(2)	39(2)	39(3)	-14(2)	13(2)	-2(2)
C(45)	35(2)	29(2)	26(2)	-6(2)	6(2)	3(2)
C(24)	32(2)	26(2)	44(3)	9(2)	18(2)	4(2)
C(28)	36(2)	20(2)	48(3)	1(2)	19(2)	3(2)
C(8)	42(3)	27(2)	29(2)	-1(2)	11(2)	0(2)
C(7)	26(2)	26(2)	44(3)	-1(2)	5(2)	-1(2)
C(29)	35(2)	29(2)	41(3)	-10(2)	13(2)	-3(2)
C(13)	38(3)	32(2)	54(3)	-6(2)	25(2)	-7(2)
C(15)	33(2)	36(2)	35(2)	-1(2)	12(2)	-1(2)

Table 2.12 (contin.) Anisotropic displacement parameters ($\text{\AA}^2 \times 10^3$) for **2.21-BARF**. The anisotropic displacement factor exponent takes the form: $-2\pi^2[h^2a^*2U^{11} + \dots + 2hk a^*b^*U^{12}]$

	U^{11}	U^{22}	U^{33}	U^{23}	U^{13}	U^{12}
C(1)	42(3)	41(3)	50(3)	8(2)	26(2)	5(2)
C(41)	56(3)	40(3)	29(2)	4(2)	24(2)	14(2)
C(14)	34(2)	41(3)	49(3)	-2(2)	21(2)	-5(2)
C(17)	42(3)	29(2)	42(3)	5(2)	17(2)	-1(2)
C(18)	51(3)	35(2)	42(3)	-5(2)	18(2)	-10(2)
C(16)	47(3)	43(3)	55(3)	0(2)	27(3)	-15(2)
C(39)	52(3)	39(2)	47(3)	0(2)	34(2)	-5(2)
C(4)	32(2)	44(3)	56(3)	4(2)	20(2)	2(2)
C(40)	66(3)	50(3)	42(3)	12(2)	41(3)	10(3)
C(3)	36(3)	53(3)	68(4)	11(3)	25(3)	7(2)
B(02D)	27(2)	23(2)	24(2)	-1(2)	12(2)	0(2)
C(2)	62(4)	56(3)	64(4)	8(3)	45(3)	-1(3)
O(4)	50(2)	54(2)	48(2)	9(2)	25(2)	12(2)

Table 2. 13 Hydrogen coordinates ($\times 10^4$) and isotropic displacement parameters ($\text{\AA}^2 \times 10^3$) for **2.21-BARF**

	x	y	z	U(eq)
H(21)	6209	5308	2024	38
H(30)	7661	7039	4512	39
H(23)	6348	7660	2207	41
H(20)	6319	3319	2306	38
H(9)	7528	3812	5472	41
H(12)	6759	4051	5033	43
H(24)	6690	9168	2744	42
H(28)	7222	9757	3592	43
H(8)	8304	3670	5827	44
H(7)	8657	3971	5421	46
H(29)	7646	9089	4331	46
H(13)	5986	4279	4532	49
H(15)	6213	4838	3520	45
H(1)	7780	4724	3413	52
H(14)	5713	4655	3771	50
H(17)	6045	590	3122	48
H(18A)	5683	2638	2523	68
H(18B)	5463	1305	2399	68
H(18C)	5947	1520	2469	68
H(16A)	5809	1657	3571	71
H(16B)	5392	1186	3103	71
H(16C)	5537	2593	3161	71
H(4)	8909	4539	4923	54
H(3)	9094	4831	4373	64
H(2)	8527	4836	3608	66
H(4A)	8122	1313	4066	76
	7735	1810	4038	76

Table 2. 14 Crystallographic information for **2.24-OTf**

Empirical Formula	C ₂₈ H _{18.66} F ₃ N ₅ O _{6.38} Ru S ₂	
Formula weight	749.41	
Temperature (K)	100	
Wavelength (Å)	0.71073	
Space group	P-1 (no. 1)	
Unit cell dimensions	a (Å) = 9.0458(4)	α (°) = 112.1000(10)
	b (Å) = 13.2656(5)	β (°) = 92.3820(10)
	c (Å) = 14.0830(5)	γ (°) = 105.8770(10)
Volume (Å³)	1486.11(10)	
Z	2	
Density (calculated) Mg/m³	1.675	
μ (mm ⁻¹)	0.74	
F(000)	751	
Crystal size mm³	0.28 x 0.25 x 0.24	
Theta range for data collection	1.744 to 28.364°	
Index ranges	-12 ≤ h ≤ 12	
	-17 ≤ k ≤ 17	
	-18 ≤ l ≤ 17	
Reflections collected	26661	
Independent reflections	7415 [R(int) = 0.0339]	
Completeness to theta = 25.242°	100.00%	
Absorption correction	Semi-empirical from equivalents	
Max. and min. transmission	0.7457 and 0.6979	
Refinement method	Full-matrix least-squares on F ²	
Data / restraints / parameters	7415 / 0 / 415	
Goodness-of-fit on F²	1.028	
Final R indices [I > 2σ(I)]	R1 = 0.0304, wR2 = 0.0689	
R indices (all data)	R1 = 0.0373, wR2 = 0.0735	
Extinction coefficient	n/a	
Largest diff. peak and hole	0.647 and -0.954 e.Å ⁻³	
SQUEEZE	Found: 50e/uc (water?)	

Table 2. 15 Atomic coordinates ($\times 10^4$) and equivalent isotropic displacement parameters ($\text{\AA}^2 \times 10^3$) for **2.24**. $U(\text{eq})$ is defined as one third of the trace of the orthogonalized U^{ij} tensor.

	x	y	z	U(eq)
Ru(1)	6419(1)	7650(1)	3219(1)	19(1)
S(1)	-727(1)	3618(1)	1608(1)	28(1)
S(2)	7839(1)	7755(1)	5339(1)	21(1)
F(1)	-592(2)	3643(2)	3479(1)	54(1)
F(2)	-211(2)	5285(1)	3448(1)	39(1)
F(3)	1590(2)	4500(2)	3143(1)	68(1)
O(1)	8008(2)	8431(1)	4690(1)	22(1)
O(2)	9317(2)	7834(2)	5824(1)	30(1)
O(3)	6712(2)	7976(1)	6026(1)	27(1)
O(4)	-11(3)	4465(2)	1244(2)	65(1)
O(5)	-267(3)	2605(2)	1238(2)	74(1)
O(6)	-2373(2)	3397(2)	1589(1)	38(1)
N(1)	8366(2)	7727(2)	2495(1)	24(1)
N(2)	6542(2)	8978(2)	2880(1)	21(1)
N(3)	4977(2)	6406(2)	1908(1)	22(1)
N(4)	6270(2)	6278(2)	3536(1)	20(1)
N(5)	4539(2)	8095(2)	3827(1)	18(1)
C(1)	9234(2)	7013(2)	2292(2)	26(1)
C(2)	10514(3)	7152(2)	1789(2)	31(1)
C(3)	10935(3)	8060(3)	1500(2)	34(1)
C(4)	10059(3)	8807(2)	1707(2)	32(1)
C(5)	8768(3)	8619(2)	2195(2)	28(1)
C(6)	7722(3)	9336(2)	2405(2)	28(1)
C(7)	7819(3)	10264(3)	2156(2)	39(1)
C(8)	6685(3)	10804(2)	2384(2)	34(1)
C(9)	5475(3)	10422(2)	2867(2)	26(1)
C(10)	5440(2)	9506(2)	3124(2)	20(1)
C(11)	4300(2)	8997(2)	3668(2)	18(1)
C(12)	3080(2)	9407(2)	4019(2)	20(1)
C(13)	2062(2)	8879(2)	4525(2)	22(1)
C(14)	2290(2)	7957(2)	4674(2)	22(1)
C(15)	3540(2)	7592(2)	4318(2)	21(1)
C(16)	4277(2)	6484(2)	1090(2)	25(1)
C(17)	3264(3)	5515(2)	271(2)	28(1)
C(18)	2978(3)	4452(2)	273(2)	27(1)
C(19)	3718(2)	4331(2)	1109(2)	24(1)

Table 2.15 (contin.) Atomic coordinates ($\times 10^4$) and equivalent isotropic displacement parameters ($\text{\AA}^2 \times 10^3$) for **2.24**. $U(\text{eq})$ is defined as one third of the trace of the orthogonalized U^{ij} tensor.

	x	y	z	U(eq)
C(20)	3527(3)	3263(2)	1201(2)	28(1)
C(21)	4228(3)	3202(2)	2042(2)	28(1)
C(22)	5191(3)	4221(2)	2880(2)	24(1)
C(23)	5947(3)	4269(2)	3804(2)	26(1)
C(24)	6811(3)	5312(2)	4567(2)	24(1)
C(25)	6939(2)	6311(2)	4411(2)	20(1)
C(26)	5400(2)	5256(2)	2785(2)	21(1)
C(27)	4688(2)	5328(2)	1902(2)	22(1)
C(28)	54(3)	4282(2)	2987(2)	31(1)
O(OAA)	11367(5)	11362(4)	1972(3)	32(1)

Table 2. 16 Bond lengths [Å] for **2.24-OTf**

Ru(1)-O(1)	2.1800(14)
Ru(1)-N(1)	2.0691(17)
Ru(1)-N(2)	1.9691(18)
Ru(1)-N(3)	2.0401(19)
Ru(1)-N(4)	2.0031(18)
Ru(1)-N(5)	2.0648(16)
S(1)-O(4)	1.416(2)
S(1)-O(5)	1.431(2)
S(1)-O(6)	1.4341(17)
S(1)-C(28)	1.818(2)
S(2)-O(1)	1.4881(15)
S(2)-O(2)	1.4355(16)
S(2)-O(3)	1.4462(15)
S(2)-C(25)	1.793(2)
F(1)-C(28)	1.320(3)
F(2)-C(28)	1.337(3)
F(3)-C(28)	1.330(3)
N(1)-C(1)	1.348(3)
N(1)-C(5)	1.365(3)
N(2)-C(6)	1.354(3)
N(2)-C(10)	1.353(3)
N(3)-C(16)	1.343(3)
N(3)-C(27)	1.377(3)
N(4)-C(25)	1.330(2)
N(4)-C(26)	1.357(3)
N(5)-C(11)	1.366(3)
N(5)-C(15)	1.345(3)
C(1)-C(2)	1.388(3)
C(2)-C(3)	1.375(4)
C(3)-C(4)	1.388(4)
C(4)-C(5)	1.392(3)
C(5)-C(6)	1.481(3)
C(6)-C(7)	1.383(3)
C(7)-C(8)	1.387(3)
C(8)-C(9)	1.391(3)
C(9)-C(10)	1.386(3)
C(10)-C(11)	1.477(3)

Table 2.16 (contin.) Bond lengths [Å] for **2.24-OTf**

C(11)-C(12)	1.389(3)
C(12)-C(13)	1.388(3)
C(13)-C(14)	1.380(3)
C(14)-C(15)	1.388(3)
C(16)-C(17)	1.405(3)
C(17)-C(18)	1.364(4)
C(18)-C(19)	1.413(3)
C(19)-C(20)	1.436(3)
C(19)-C(27)	1.392(3)
C(20)-C(21)	1.360(3)
C(21)-C(22)	1.432(3)
C(22)-C(23)	1.415(3)
C(22)-C(26)	1.392(3)
C(23)-C(24)	1.379(3)
C(24)-C(25)	1.398(3)
C(26)-C(27)	1.424(3)

Table 2. 17 Bond angles [°] for **2.24-OTf**

N(1)-Ru(1)-O(1)	87.30(6)
N(2)-Ru(1)-O(1)	102.05(7)
N(2)-Ru(1)-N(1)	79.45(7)
N(2)-Ru(1)-N(3)	98.31(7)
N(2)-Ru(1)-N(4)	178.85(7)
N(2)-Ru(1)-N(5)	79.42(7)
N(3)-Ru(1)-O(1)	159.36(7)
N(3)-Ru(1)-N(1)	93.17(7)
N(3)-Ru(1)-N(5)	90.48(7)
N(4)-Ru(1)-O(1)	79.09(6)
N(4)-Ru(1)-N(1)	100.47(7)
N(4)-Ru(1)-N(3)	80.55(7)
N(4)-Ru(1)-N(5)	100.67(7)
N(5)-Ru(1)-O(1)	96.49(6)
N(5)-Ru(1)-N(1)	158.86(7)
O(4)-S(1)-O(5)	115.71(18)
O(4)-S(1)-O(6)	114.69(14)
O(4)-S(1)-C(28)	103.70(13)
O(5)-S(1)-O(6)	113.79(15)
O(5)-S(1)-C(28)	103.42(12)
O(6)-S(1)-C(28)	103.35(11)
O(1)-S(2)-C(25)	103.19(9)
O(2)-S(2)-O(1)	112.20(9)
O(2)-S(2)-O(3)	115.28(10)
O(2)-S(2)-C(25)	108.54(10)
O(3)-S(2)-O(1)	112.11(9)
O(3)-S(2)-C(25)	104.41(9)
S(2)-O(1)-Ru(1)	116.35(9)
C(1)-N(1)-Ru(1)	127.91(16)
C(1)-N(1)-C(5)	118.55(19)
C(5)-N(1)-Ru(1)	113.53(14)
C(6)-N(2)-Ru(1)	119.21(15)
C(10)-N(2)-Ru(1)	119.07(14)
C(10)-N(2)-C(6)	121.72(19)
C(16)-N(3)-Ru(1)	130.49(17)
C(16)-N(3)-C(27)	117.13(19)
C(27)-N(3)-Ru(1)	112.37(13)
C(25)-N(4)-Ru(1)	124.85(16)

Table 2.17 (contin.) Bond angles [°] for **2.24-OTf**

C(25)-N(4)-C(26)	119.66(19)
C(26)-N(4)-Ru(1)	115.48(13)
C(11)-N(5)-Ru(1)	113.65(13)
C(15)-N(5)-Ru(1)	128.06(14)
C(15)-N(5)-C(11)	118.27(17)
N(1)-C(1)-C(2)	122.4(2)
C(3)-C(2)-C(1)	119.2(2)
C(2)-C(3)-C(4)	119.3(2)
C(3)-C(4)-C(5)	119.4(2)
N(1)-C(5)-C(4)	121.2(2)
N(1)-C(5)-C(6)	115.45(18)
C(4)-C(5)-C(6)	123.4(2)
N(2)-C(6)-C(5)	112.3(2)
N(2)-C(6)-C(7)	119.9(2)
C(7)-C(6)-C(5)	127.8(2)
C(6)-C(7)-C(8)	119.2(2)
C(7)-C(8)-C(9)	120.3(2)
C(10)-C(9)-C(8)	118.7(2)
N(2)-C(10)-C(9)	120.21(19)
N(2)-C(10)-C(11)	112.47(18)
C(9)-C(10)-C(11)	127.32(19)
N(5)-C(11)-C(10)	115.32(17)
N(5)-C(11)-C(12)	121.45(18)
C(12)-C(11)-C(10)	123.21(19)
C(13)-C(12)-C(11)	119.5(2)
C(14)-C(13)-C(12)	119.12(19)
C(13)-C(14)-C(15)	119.0(2)
N(5)-C(15)-C(14)	122.7(2)
N(3)-C(16)-C(17)	121.7(2)
C(18)-C(17)-C(16)	120.7(2)
C(17)-C(18)-C(19)	119.2(2)
C(18)-C(19)-C(20)	124.8(2)
C(27)-C(19)-C(18)	117.0(2)
C(27)-C(19)-C(20)	118.21(19)
C(21)-C(20)-C(19)	122.2(2)
C(20)-C(21)-C(22)	120.4(2)
C(23)-C(22)-C(21)	125.5(2)

Table 2.17 (contin.) Bond angles [°] for **2.24-OTf**

C(25)-N(4)-C(26)	119.66(19)
C(26)-N(4)-Ru(1)	115.48(13)
C(11)-N(5)-Ru(1)	113.65(13)
C(15)-N(5)-Ru(1)	128.06(14)
C(15)-N(5)-C(11)	118.27(17)
N(1)-C(1)-C(2)	122.4(2)
C(3)-C(2)-C(1)	119.2(2)
C(2)-C(3)-C(4)	119.3(2)
C(3)-C(4)-C(5)	119.4(2)
N(1)-C(5)-C(4)	121.2(2)
N(1)-C(5)-C(6)	115.45(18)
C(4)-C(5)-C(6)	123.4(2)
N(2)-C(6)-C(5)	112.3(2)
N(2)-C(6)-C(7)	119.9(2)
C(7)-C(6)-C(5)	127.8(2)
C(6)-C(7)-C(8)	119.2(2)
C(7)-C(8)-C(9)	120.3(2)
C(10)-C(9)-C(8)	118.7(2)
N(2)-C(10)-C(9)	120.21(19)
N(2)-C(10)-C(11)	112.47(18)
C(9)-C(10)-C(11)	127.32(19)
N(5)-C(11)-C(10)	115.32(17)
N(5)-C(11)-C(12)	121.45(18)
C(12)-C(11)-C(10)	123.21(19)
C(13)-C(12)-C(11)	119.5(2)
C(14)-C(13)-C(12)	119.12(19)
C(13)-C(14)-C(15)	119.0(2)
N(5)-C(15)-C(14)	122.7(2)
N(3)-C(16)-C(17)	121.7(2)
C(18)-C(17)-C(16)	120.7(2)
C(17)-C(18)-C(19)	119.2(2)
C(18)-C(19)-C(20)	124.8(2)
C(27)-C(19)-C(18)	117.0(2)
C(27)-C(19)-C(20)	118.21(19)
C(21)-C(20)-C(19)	122.2(2)
C(20)-C(21)-C(22)	120.4(2)
C(23)-C(22)-C(21)	125.5(2)

Table 2.17 (contin.) Bond angles [°] for **2.24-OTf**

C(26)-C(22)-C(21)	117.5(2)
C(24)-C(23)-C(22)	119.8(2)
C(23)-C(24)-C(25)	119.27(19)
N(4)-C(25)-S(2)	111.56(16)
N(4)-C(25)-C(24)	121.6(2)
C(24)-C(25)-S(2)	126.69(16)
N(4)-C(26)-C(22)	122.64(19)
N(4)-C(26)-C(27)	114.77(19)
C(22)-C(26)-C(27)	122.6(2)
N(3)-C(27)-C(19)	124.13(19)
N(3)-C(27)-C(26)	116.78(19)
C(19)-C(27)-C(26)	119.1(2)
F(1)-C(28)-S(1)	112.24(19)
F(1)-C(28)-F(2)	106.4(2)
F(1)-C(28)-F(3)	109.2(2)
F(2)-C(28)-S(1)	111.10(16)
F(3)-C(28)-S(1)	111.05(17)
F(3)-C(28)-F(2)	106.6(2)

Symmetry transformations used to generate equivalent atoms:

Table 2. 18 Anisotropic displacement parameters ($\text{\AA}^2 \times 10^3$) for **2.24-OTf**. The anisotropic displacement factor exponent takes the form: $-2\pi^2[h^2a^{*2}U^{11} + \dots + 2hk a^*b^*U^{12}]$

	U^{11}	U^{22}	U^{33}	U^{23}	U^{13}	U^{12}
Ru(1)	17(1)	33(1)	13(1)	12(1)	6(1)	15(1)
S(1)	22(1)	42(1)	21(1)	11(1)	4(1)	16(1)
S(2)	17(1)	36(1)	15(1)	14(1)	6(1)	12(1)
F(1)	87(1)	59(1)	38(1)	34(1)	12(1)	36(1)
F(2)	45(1)	37(1)	31(1)	7(1)	2(1)	14(1)
F(3)	33(1)	130(2)	31(1)	12(1)	-2(1)	42(1)
O(1)	21(1)	35(1)	15(1)	13(1)	5(1)	12(1)
O(2)	21(1)	46(1)	27(1)	20(1)	-1(1)	11(1)
O(3)	27(1)	36(1)	20(1)	11(1)	13(1)	12(1)
O(4)	57(1)	91(2)	38(1)	39(1)	6(1)	-8(1)
O(5)	88(2)	90(2)	42(1)	-5(1)	-5(1)	73(2)
O(6)	22(1)	52(1)	30(1)	4(1)	3(1)	12(1)
N(1)	20(1)	44(1)	13(1)	14(1)	5(1)	18(1)
N(2)	18(1)	35(1)	16(1)	14(1)	5(1)	13(1)
N(3)	20(1)	38(1)	15(1)	12(1)	7(1)	18(1)
N(4)	19(1)	34(1)	14(1)	11(1)	6(1)	17(1)
N(5)	16(1)	28(1)	14(1)	9(1)	5(1)	10(1)
C(1)	21(1)	43(1)	16(1)	9(1)	4(1)	19(1)
C(2)	21(1)	54(2)	18(1)	7(1)	4(1)	20(1)
C(3)	21(1)	67(2)	21(1)	20(1)	10(1)	20(1)
C(4)	30(1)	58(2)	19(1)	22(1)	12(1)	20(1)
C(5)	21(1)	55(2)	21(1)	24(1)	9(1)	20(1)
C(6)	22(1)	53(2)	25(1)	27(1)	11(1)	19(1)
C(7)	29(1)	73(2)	46(2)	48(2)	20(1)	25(1)
C(8)	29(1)	53(2)	42(1)	37(1)	11(1)	19(1)
C(9)	23(1)	36(1)	24(1)	16(1)	4(1)	13(1)
C(10)	17(1)	30(1)	15(1)	10(1)	2(1)	10(1)
C(11)	16(1)	25(1)	12(1)	6(1)	1(1)	7(1)
C(12)	18(1)	24(1)	16(1)	5(1)	2(1)	8(1)
C(13)	16(1)	27(1)	18(1)	3(1)	3(1)	8(1)
C(14)	18(1)	30(1)	17(1)	7(1)	6(1)	7(1)
C(15)	20(1)	28(1)	17(1)	10(1)	5(1)	10(1)
C(16)	23(1)	44(1)	20(1)	16(1)	8(1)	22(1)
C(17)	22(1)	52(2)	17(1)	15(1)	5(1)	22(1)
C(18)	20(1)	43(1)	18(1)	9(1)	4(1)	14(1)
C(19)	19(1)	40(1)	18(1)	10(1)	7(1)	17(1)
C(20)	26(1)	35(1)	22(1)	6(1)	6(1)	14(1)

Table 2.18 (contin.) Anisotropic displacement parameters ($\text{\AA}^2 \times 10^3$) for **2.24-OTf**. The anisotropic displacement factor exponent takes the form: $-2\pi^2[h^2a^*2U^{11} + \dots + 2hkab^*U^{12}]$

	U¹¹	U²²	U³³	U²³	U¹³	U¹²
C(21)	32(1)	32(1)	25(1)	10(1)	9(1)	19(1)
C(22)	24(1)	35(1)	20(1)	11(1)	9(1)	20(1)
C(23)	30(1)	38(1)	24(1)	18(1)	13(1)	23(1)
C(24)	25(1)	40(1)	18(1)	16(1)	9(1)	20(1)
C(25)	17(1)	36(1)	16(1)	12(1)	7(1)	15(1)
C(26)	21(1)	35(1)	16(1)	11(1)	8(1)	18(1)
C(27)	21(1)	35(1)	16(1)	12(1)	8(1)	18(1)
C(28)	31(1)	45(1)	25(1)	15(1)	3(1)	21(1)
O(OAA)	30(1)	58(2)	19(1)	22(1)	12(1)	20(1)

Table 2.19 Hydrogen coordinates ($\times 10^4$) and isotropic displacement parameters ($\text{\AA}^2 \times 10^3$) for **2.24-OTf**

	x	y	z	U(eq)
H(1)	8959	6392	2500	31
H(2)	11092	6627	1646	37
H(3)	11816	8174	1163	41
H(4)	10339	9441	1516	39
H(7)	8653	10528	1833	47
H(8)	6735	11437	2210	41
H(9)	4689	10783	3018	31
H(12)	2944	10044	3913	24
H(13)	1220	9147	4767	27
H(14)	1603	7579	5014	27
H(15)	3696	6961	4426	25
H(16)	4472	7214	1065	30
H(17)	2773	5602	-290	33
H(18)	2288	3800	-282	33
H(20)	2890	2575	655	34
H(21)	4078	2478	2074	34
H(23)	5859	3583	3897	31
H(24)	7315	5352	5191	29
H(OAA)	10693	11645	1795	49
H(OAB)	11484	11638	2647	49

General Information

All chemicals were purchased from commercial suppliers and used without further purification. NMR data were measured at room temperature. Two Varian spectrometers were used: a 500-MHz INOVA (^1H = 499.940 MHz, ^{13}C = 125.718 MHz) and a 400-MHz Varian NMR-S (^1H = 399.753 MHz, ^{13}C = 100.525 MHz). Elemental analyses were performed at NuMega Resonance Laboratories (San Diego).

Computations

Prof. Djamaladdin Musaev of the Center for Scientific Computation at Emory University performed these computations. Geometry optimizations and frequency calculations for all reported structures were performed with the Gaussian 09 suite of programs at the B3LYP-D3BJ/[6-31G(d,p) + Lanl2dz (Ru)] level of theory with the corresponding Hay-Wadt effective core potential for Ru, and Grimme's empirical dispersion-correction (D3) with Becke-Johnson (BJ) damping for B3LYP⁴⁶⁻⁵¹. Frequency analysis was used to characterize each minimum with zero imaginary frequencies. Bulk solvent effects are incorporated for all calculations using the self-consistent reaction field polarizable continuum model (IEF-PCM)⁵²⁻⁵⁴. As a solvent we chose H₂O. The Gibbs free energies are calculated at 298.15 K temperature and 1 atm. pressure.

EPR Measurements

EPR experiments were performed at the Borovik lab at the University of California, Irvine. X-band (microwave frequency 9.62 GHz) EPR spectra were collected at 77 K on a Bruker EMX spectrometer equipped with an ER041XG microwave bridge,

a cold finger liquid nitrogen dewar flask, and a perpendicular-mode (ER4119HS-W1) cavity.

Manometry

All manometry experiments were performed with a custom made cell. The cell cap is made from PEEK and its fitted with an injection port (Hamilton, Valco), a SensorsOne UPS-HSR-B02P5-N USB pressure sensor (Stork Solutions), an UltraTorr fitting (SwageLok) to accommodate an FOSPOR oxygen optode (Ocean Optics), and a custom made fitting that accommodates a thermocouple. The body of the cell is made of glass and is immersed in a 30 °C constant temperature bath (Lauda). The system was allowed to reach thermal equilibrium before the catalyst solution was injected.

Electrochemistry

Cyclic voltammetry and square wave voltammetry experiments were performed on a CHI760E, CHI730E, or CHI600C potentiostat (CH Instruments, Inc.). Glassy carbon electrodes were purchased from CH Instruments, Inc. (CHI104) and were polished with 0.25 micron and 0.05 micron polishing compounds prior to use. Aqueous cyclic voltammetry experiments were performed with a glassy carbon working electrode, a Ag/AgCl reference electrode, and Pt wire counter electrode. The analyte solution was sparged with N₂ or Ar gas for 5 minutes prior to beginning an experiment and the cell headspace was blanketed with flowing N₂ or Ar gas throughout an experiment.

Acknowledgements

Chapter 2 is adapted from a manuscript being prepared for publication titled “A Fast and Durable Ruthenium-Based Water Oxidation Catalyst with a Sulfonate Moiety in the Active Site” by A.G. Nash, C.J. Breyer, B.D. Vincenzini, G. Elliott, D.K. Smith, A.L. Rheingold, D. Musaev, and D.B. Grotjahn. Permission to include published material in this dissertation has been obtained from all coauthors. The dissertation author is the first author of this paper.

References

1. Boyer, J. L.; Polyansky, D. E.; Szalda, D. J.; Zong, R.; Thummel, R. P.; Fujita, E. *Angew. Chem. Int. Ed.* **2011**, *50*, 12600
2. Yamazaki, H.; Hakamata, T.; Komi, M.; Yagi, M. *J. Am. Chem. Soc.* **2011**, *133*, 8846.
3. Hirahara, M.; Ertem, M. Z.; Komi, M.; Yamazaki, H.; Cramer, C. J.; Yagi, M. *Inorg. Chem.* **2013**, *52*, 6354.
4. Creus, J.; Matheu, R.; Peñafiel, I.; Moonshiram, D.; Blondeau, P.; Benet-Buchholz, J.; García-Antón, J.; Sala, X.; Godard, C.; Llobet, A. *Angewandte Chemie International Edition* **2016**, *55*, 15382.
5. Matheu, R.; Ertem, M. Z.; Benet-Buchholz, J.; Coronado, E.; Batista, V. S.; Sala, X.; Llobet, A. *J. Am. Chem. Soc.* **2015**, *137*, 10786.
6. Matheu, R.; Ertem, M. Z.; Gimbert-Suriñach, C.; Benet-Buchholz, J.; Sala, X.; Llobet, A. *ACS Catal.* **2017**, *7*, 6525.
7. Shaffer, D. W.; Xie, Y.; Szalda, D. J.; Concepcion, J. J. *J. Am. Chem. Soc.* **2017**, *139*, 15347.
8. Kamdar, J. M.; Marelius, D. C.; Moore, C. E.; Rheingold, A. L.; Smith, D. K.; Grotjahn, D. B. *ChemCatChem* **2016**, *8*, 3045.
9. Xie, Y.; Shaffer, D. W.; Lewandowska-Andralojc, A.; Szalda, D. J.; Concepcion, J. J. *Angewandte Chemie International Edition* **2016**, *55*, 8067.
10. Thuéry, P.; Atoini, Y.; Harrowfield, J. *Dalton Trans.* **2019**, *48*, 8756.
11. Díaz-Torres, R.; Alvarez, S. *Dalton Trans.* **2011**, *40*, 10742.
12. Côté, A. P.; Shimizu, G. K. H. *Coordination Chemistry Reviews* **2003**, *245*, 49.
13. Cremlyn, R. J. *An Introduction to Organosulfur Chemistry*; John Wiley & Sons Ltd.: Chichester, **1996**.
14. Mahe, R.; Sasaki, Y.; Bruneau, C.; Dixneuf, P. H. *J. Org. Chem.* **1989**, *54*, 1518.
15. Bashir, O.; Piche, L.; Claverie, J. P. *Organometallics* **2014**, *33*, 3695.
16. Li, M.; Song, H.; Wang, B. *European Journal of Inorganic Chemistry* **2015**, *2015*, 4055.

17. Koelewijn, J. M.; Lutz, M.; Dzik, W. I.; Detz, R. J.; Reek, J. N. H. *ACS Catal.* **2016**, *6*, 3418.
18. Blackmond, D. G. *Angewandte Chemie International Edition* **2005**, *44*, 4302.
19. Yoshida, M.; Kondo, M.; Torii, S.; Sakai, K.; Masaoka, S. *Angewandte Chemie International Edition* **2015**, *54*, 7981.
20. Patra, T.; Maiti, D. *Chemistry – A European Journal* **2017**, *23*, 7382.
21. Dzik, W. I.; Lange, P. P.; Gooßen, L. J. *Chem. Sci.* **2012**, *3*, 2671.
22. Gayathri, P.; Senthil Kumar, A. *Langmuir* **2014**, *30*, 10513.
23. Guo, H. C.; Zheng, R. H.; Jiang, H. J. *Organic Preparations and Procedures International* **2012**, *44*, 392.
24. Krapcho, A. P.; Lanza, J. B. *Organic Preparations and Procedures International* **2007**, *39*, 603.
25. Belabassi, Y.; Alzghari, S.; Montchamp, J.-L. *Journal of Organometallic Chemistry* **2008**, *693*, 3171.
26. Besthorn, E.; Geißelbrecht, B. *Ber. Dtsch. Chem. Ges.* **1920**, *53*, 1017.
27. Ziessel, R.; Grosshenny, V.; Hissler, M.; Stroh, C. *Inorg. Chem.* **2004**, *43*, 4262.
28. Lee, K. J.; McCarthy, B. D.; Dempsey, J. L. *Chem. Soc. Rev.* **2019**, *48*, 2927.
29. Licht, Stuart.; Cammarata, Vince.; Wrighton, M. S. *J. Phys. Chem.* **1990**, *94*, 6133.
30. Wang, Y.; Limon-Petersen, J. G.; Compton, R. G. *Journal of Electroanalytical Chemistry* **2011**, *652*, 13.
31. Takeuchi, K. J.; Thompson, M. S.; Pipes, D. W.; Meyer, T. J. *Inorg. Chem.* **1984**, *23*, 1845.
32. Sawyer, D. T.; Roberts, J. L. *Acc. Chem. Res.* **1988**, *21*, 469.
33. Busch, M.; Ahlberg, E.; Panas, I. *Phys. Chem. Chem. Phys.* **2011**, *13*, 15062.
34. Shimoyama, Y.; Ishizuka, T.; Kotani, H.; Shiota, Y.; Yoshizawa, K.; Mieda, K.; Ogura, T.; Okajima, T.; Nozawa, S.; Kojima, T. *Angew. Chem. Int. Ed.* **2016**, *55*, 14041.

35. Shimoyama, Y.; Kojima, T. *Inorg. Chem.* **2019**, *58*, 9517.
36. Shaffer, D. W.; Xie, Y.; Concepcion, J. J. *Chem. Soc. Rev.* **2017**, *46*, 6170.
37. Kobayashi, K.; Ohtsu, H.; Wada, T.; Kato, T.; Tanaka, K. *J. Am. Chem. Soc.* **2003**, *125*, 6729.
38. Ueda, T.; Kitagishi, H.; Kano, K. *Inorg. Chem.* **2014**, *53*, 543.
39. Kang, R.; Chen, K.; Yao, J.; Shaik, S.; Chen, H. *Inorg. Chem.* **2014**, *53*, 7130.
40. Kriechbaum, M.; List, M.; Berger, R. J. F.; Patzschke, M.; Monkowius, U. *Chemistry – A European Journal* **2012**, *18*, 5506.
41. Ghatak, T.; Sarkar, M.; Dinda, S.; Dutta, I.; Rahaman, S. M. W.; Bera, J. K. *J. Am. Chem. Soc.* **2015**, *137*, 6168.
42. Liu, G.; Liu, C.; Han, F.; Wang, Z.; Wang, J. *Tetrahedron Letters* **2017**, *58*, 726.
43. Kopchuk, D.; Khasanov, A.; Kovalev, I.; Kim, G.; Nikonov, I.; Zyryanov, G.; Rusinov, V.; Chupakhin, O. *Chemistry of Heterocyclic Compounds* **2014**, *50*, 864.
44. Ferretti, F.; Gallo, E.; Ragaini, F. *Journal of Organometallic Chemistry* **2014**, *771*, 59.
45. Akerboom, S.; van den Elshout, J. J. M. H.; Mutikainen, I.; Siegler, M. A.; Fu, W. T.; Bouwman, E. *Eur. J. Inorg. Chem.* **2013**, *2013*, 6137.
46. Grimme, S.; Antony, J.; Ehrlich, S.; Krieg, H. *J. Chem. Phys.* **2010**, *132*, 154104.
47. Becke, A. D. *J. Chem. Phys.* **1993**, *98*, 1372.
48. Wadt, W. R.; Hay, P. J. *J. Chem. Phys.* **1985**, *82*, 284.
49. Hay, P. J.; Wadt, W. R. *J. Chem. Phys.* **1985**, *82*, 270.
50. Becke, A. D. *Phys. Rev. A* **1988**, *38*, 3098.
51. Lee, C.; Yang, W.; Parr, R. G. *Phys. Rev. B* **1988**, *37*, 785.
52. Cancès, E.; Mennucci, B.; Tomasi, J. *J. Chem. Phys.* **1997**, *107*, 3032.
53. Mennucci, B.; Tomasi, J. *J. Chem. Phys.* **1997**, *106*, 5151.
54. Scalmani, G.; Frisch, M. J. *J. Chem. Phys.* **2010**, *132*, 114110.

Chapter 3 – Improved Instrumentation for Quantifying Oxygen

3.1 To Build a Better Pressure Testing Cell

Over the course of our investigations the need for a robust, easy-to-use instrument for routine catalyst testing became apparent. Our lab had previously used three different systems for measurement of oxygen: pressure transducer, polarographic sensors, and optical sensors¹⁻³.



Figure 3.1 A double Clark electrode system reported by the Grotjahn group in 2011. One of the electrodes is submerged in the reaction mixture whereas the other is in the headspace.

The first two systems of the systems mentioned relied on legacy hardware and software that provided output as raw voltage data. Moreover, we had limited ability to provide temperature control during the reaction and indeed did not use it initially (see Figure 3.1).

It eventually became clear that we had an opportunity to design a system that would be easy to use, provide good repeatability, and be durable. We also wanted a software interface that was intuitive and informative “at-a-glance”. As we had already

invested significantly in an optical oxygen-sensing system, we aimed to integrate the optical sensing hardware into our new system to provide two different complementary measurement methods. so we designed our custom pressure cell to include of our older optical oxygen sensing system.

For our first attempts at designing a pressure vessel we used a ground glass joints with Teflon/O-ring fittings but found them to be susceptible to leaking. Early attempts also included submerging the entire system under water in constant temperature bath. This led to the destruction of two pressure sensors that were advertising as water resistant; fortunately the company obliged us with free replacements.

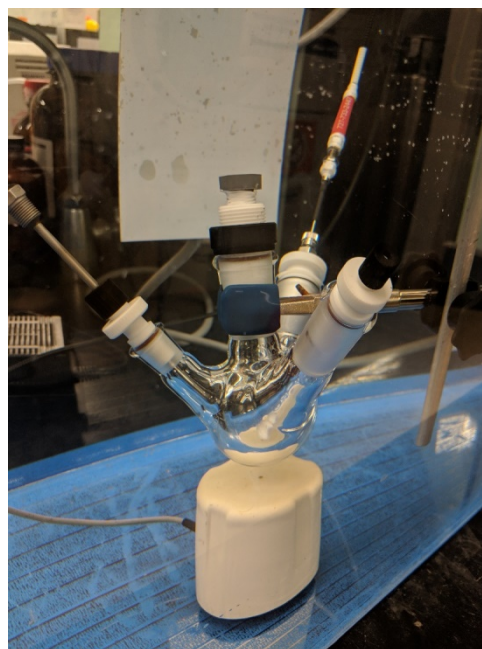


Figure 3. 2 An early attempt at cell design. We used off the shelf adapters and modified them to accommodate O-rings for extra sealing, but the cells still leaked.

Eventually we elected to construct the cell body out of glass with a threaded shank. The inner diameter needed to be wide enough to accommodate several ports for

instruments and one for injection of catalyst with sufficient room at the top of the cap to prevent crowding. We therefore opted for a ChemGlass #50 threaded blank. A custom made PEEK screwcap (machined at the Marine Research Development Center at the Scripps Institute of Oceanography) and O-ring #238 viton O-ring provides a suitable seal under pressure. Access for the Ocean Optics FOSPOR-R oxygen optode is provided by a customized SwageLok UltraTorr vacuum fitting reamed out to accommodate the sensor. We gave careful thought to the design of the injection port, as we did not want a leak developing over the course of a catalyst run. Thus, we chose to include a shut off valve to isolate the cell from the injection area. A Valco EN2SI septum injector nut provides sealing, and a Hamilton HV1-1 2-way valve provided isolation between the nut and the cell chamber. This system held pressure very well, as shown in Figure 3.3. The final pressure drop of less than 0.010 bar over such a long time period was judged quite acceptable, because typical conditions involve much less overpressure and timeframes less than 24 h.

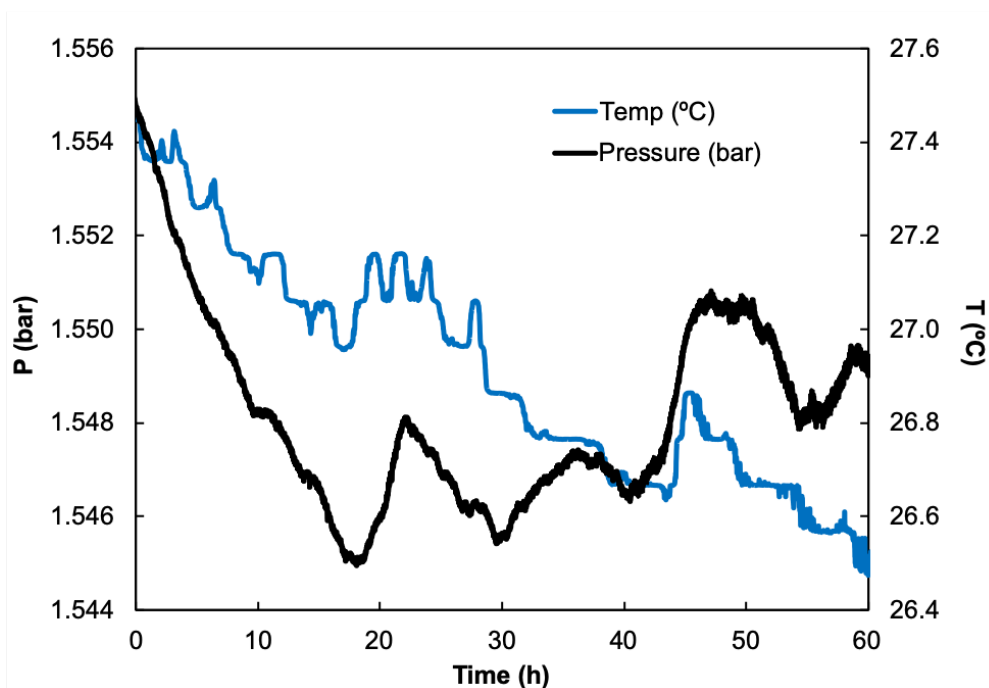


Figure 3.3 The revised cell maintained pressurization over a 60 hour leak test. Pressure fluctuations tended to vary with temperature

In a system that uses two different measurement methods, it is important to be able to start data collection simultaneously. LabView-compatible instruments can be controlled at the same time by a computer, and we were fortunate that the Ocean Optics NeoFox system we had already purchased had LabView compatibility. We sought out a suitable pressure sensor and found one from Stork Solutions (UK) UPS-HSR-B02PS-N USB pressure sensor. Graduate student colleague Colton Breyer programmed an excellent and easy to use interface in LabView that could initiate data collection from both instruments simultaneously.

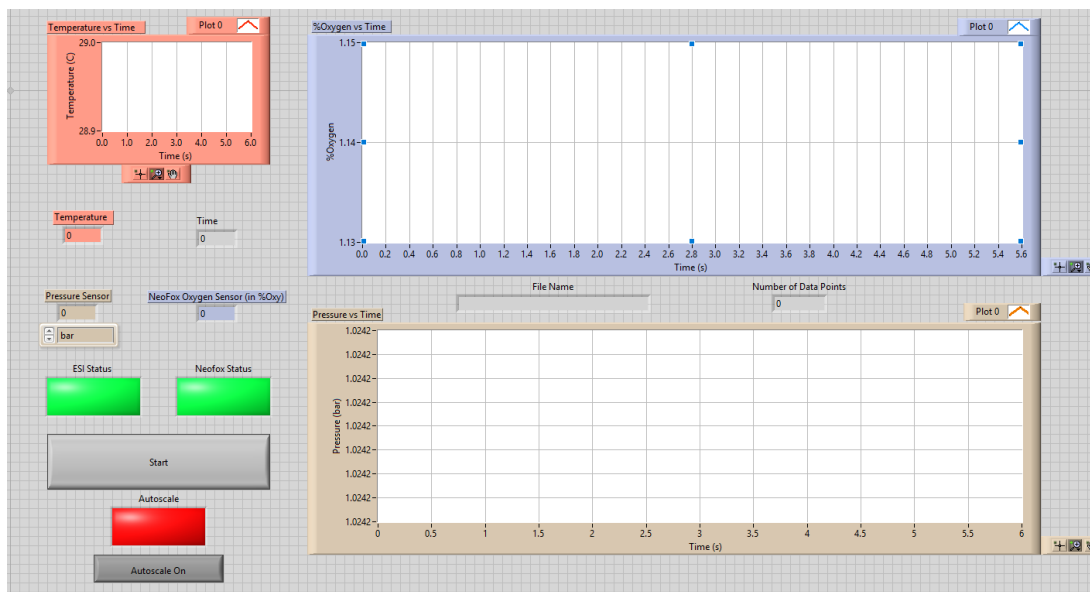


Figure 3. 4 LabView interface created by Colton Breyer. Both pressure sensor and oxygen sensor can be triggered simultaneously by pressing start. Instrument status lights show OK/off state. Data are automatically exported to Excel at the end of the run.

After testing, it was found that the NeoFox Oxygen Sensing system had several problems that dated back to the time of its purchase. Despite repeated assurances from

the manufacturer, we learned through trial and error that the high humidity environment of the cell lead to moisture condensing on the optical sensor. When the moisture beads on the optode and then drops off there is disruption in oxygen reading. This phenomenon was noted by a previous graduate student.

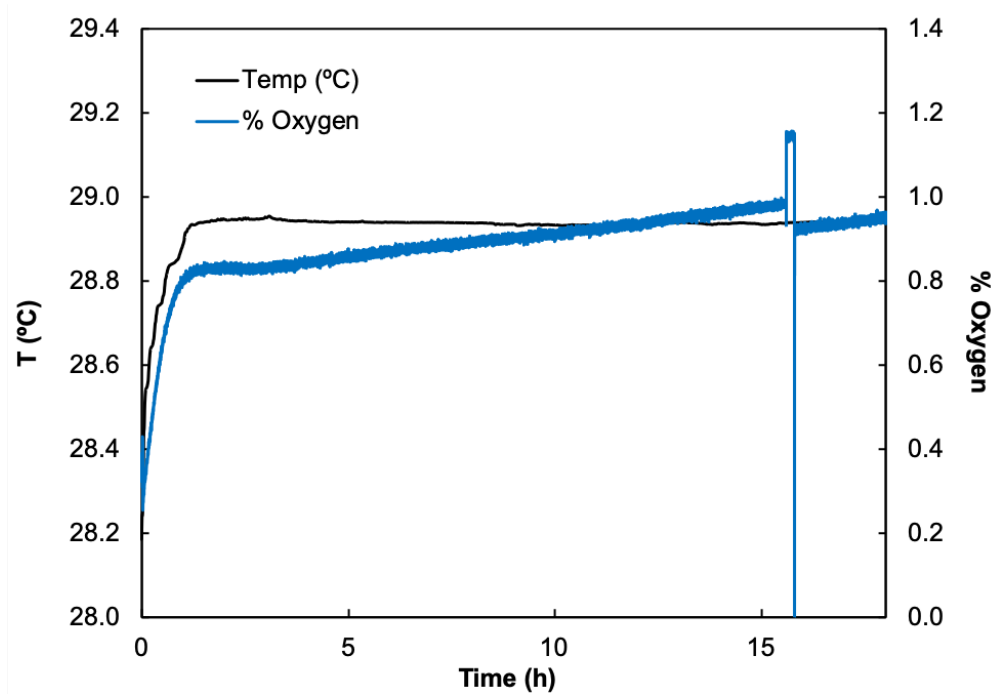


Figure 3.5 Water droplets cause errors with the oxygen sensor readings. Note that temperature trace remains steady

The NeoFox system also constantly provided falsely high oxygen readings. We believe this may result from the instrument only accepting a two-point calibration. It is hoped that continued discussions with the manufacturer will allow us to resolve these problems.

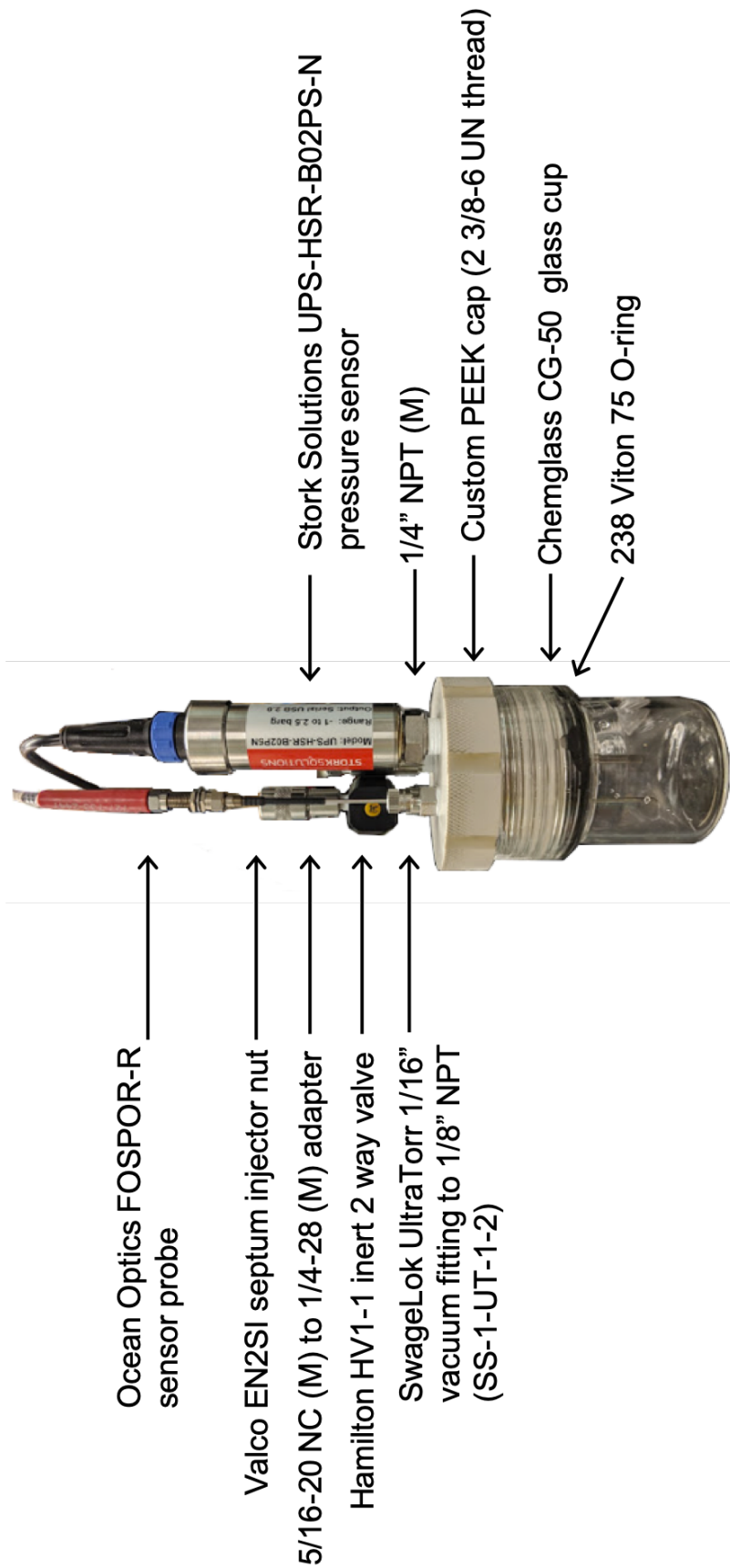


Figure 3. 6 schematic of pressure cell used in this study

3.2 Measuring oxygen and trace gases in an electrochemical cell

Our laboratory seeks to design molecular electrocatalysts to oxidize H_2O to O_2 . In a practical implementation the catalyst would have to work on large scale for a long period of time. This large-scale process is called controlled potential or bulk electrolysis, typically using a high surface area anode that is held at a potential high enough to drive the catalyst. It is possible to learn about catalyst performance as defined by oxygen production measure by sampling the headspace of the vessel. Catalyst durability can also be measured in terms of CO_2 levels that are indicative of catalyst degradation, as has been shown elsewhere. A two compartment (“H”) cell could be sampled using the following configuration:

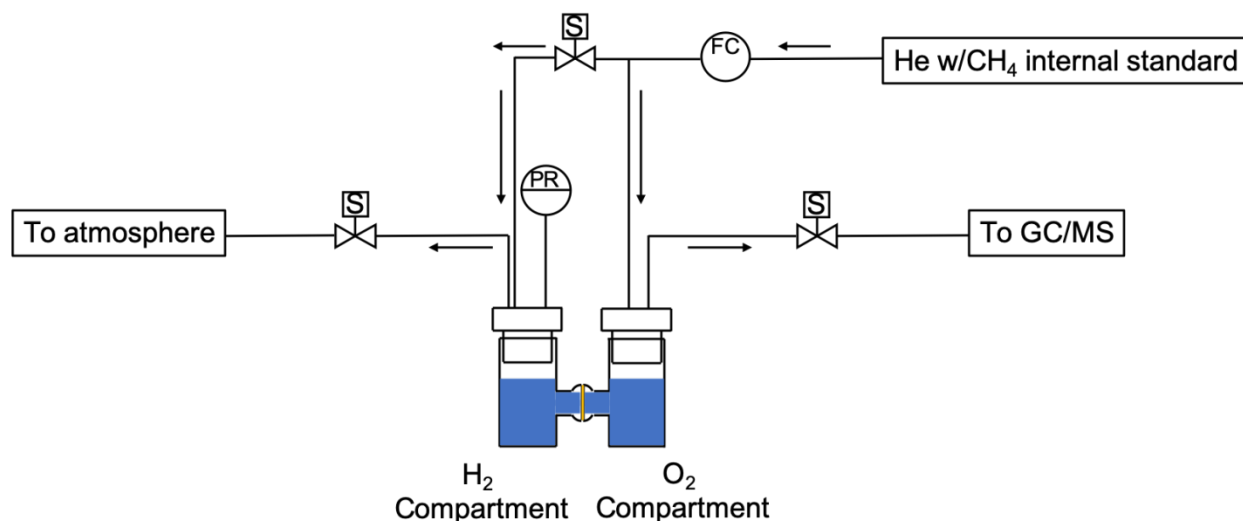


Figure 3. 7 Piping and instrumentation diagram (P&ID) for headspace sampling of a H type bulk electrolysis cell.

In the configuration above a series of solenoids open and close to move headspace from the O_2 compartment into a gas chromatograph/mass spectrometer. The hydrogen compartment is periodically vented to maintain equal pressure in each compartment. A carrier gas with CH_4 internal standard is used to push headspace into

the instrument (ThermoFisher Scientific Trace 1310 GC/MS). LabView coordinates the valve timing.

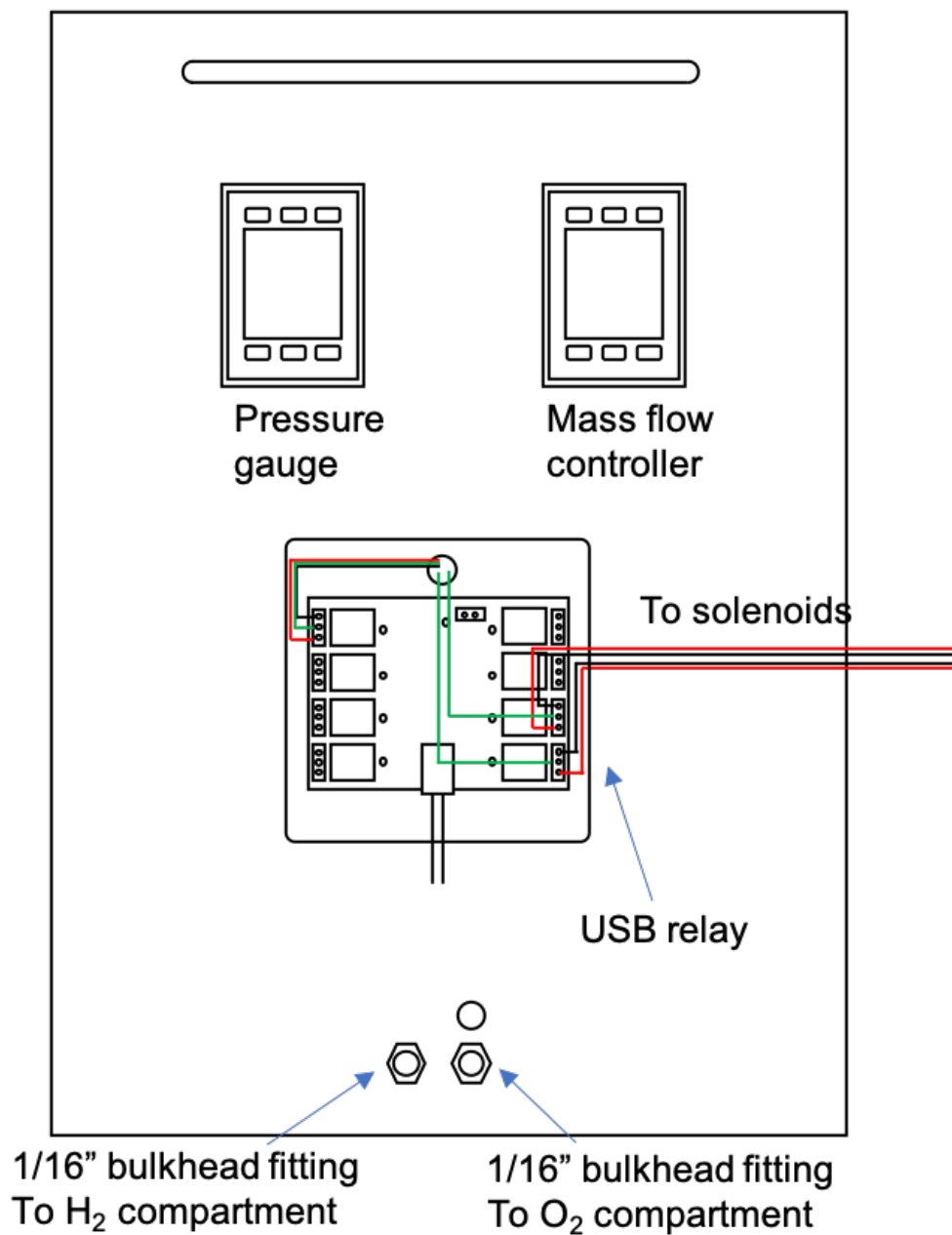


Figure 3. 8 Panel (front) of automated headspace sampling panel for bulk electrolysis cell.

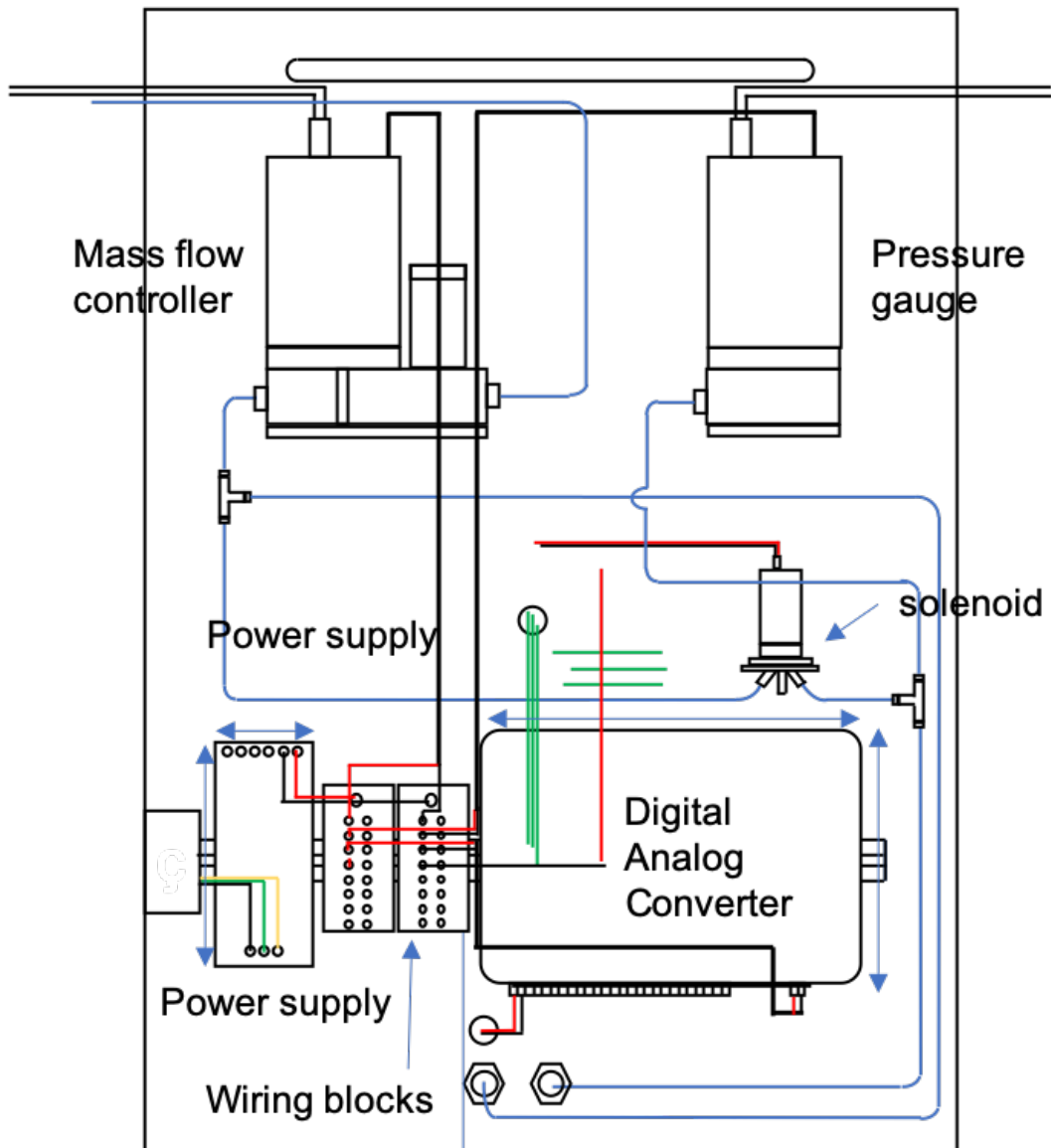


Figure 3.9 Panel (back) of automated headspace sampling panel for bulk electrolysis cell.

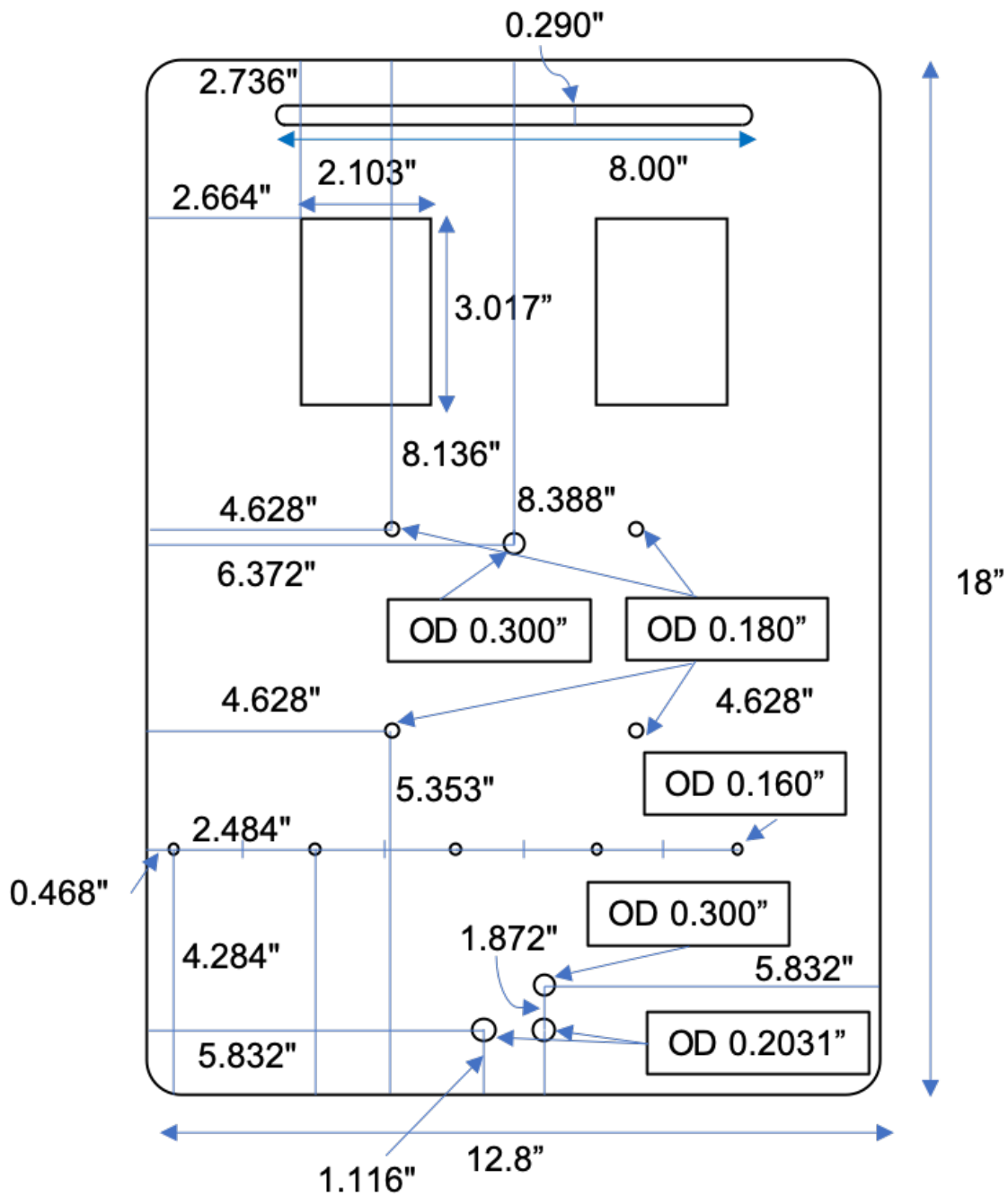


Figure 3. 10 Cutout diagram of automated headspace sampling panel for bulk electrolysis cell.



Figure 3. 11 Front of completed panel.

The panel envisioned in Figures 3.8 and 3.9 was constructed at the Campus Research Machine Shop at UCSD. It is made from black anodized aluminum and hardware is affixed via cutout holes described in Figure 3.10. Some modification (i.e. slotting some holes) proved necessary as our initial measurements did not take into account the tolerance of aluminum.

The system currently turns on and individual hardware can respond to a LabView interface. A separate manual gas manifold was constructed to serve as a testbed for the

system and has been used to demonstrate that headspace gas can be transferred repeatedly from the oxygen compartment to the GC/MS.

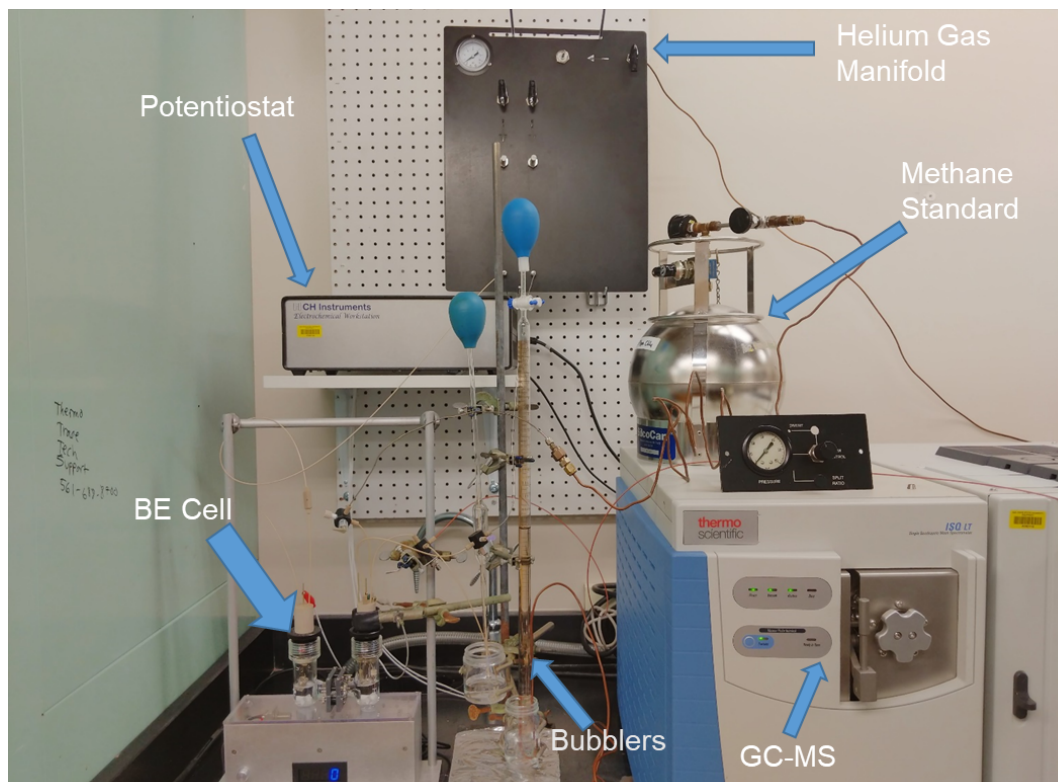


Figure 3. 12 Completed setup with manual control gas manifold. The bulk electrolysis module is sitting atop a customer made dual stirring plate.

The bulk electrolysis module is a custom built two compartment H-style cell. The two compartments are separated by a Nafion membrane and the separate compartments are held together by a custom-made screw clamp (expertly made by Prof. David Pullman). The compartments themselves were made from #25 Ace-Thred blanks that use propriety O-ring compression system to make a seal. Our process fittings were made from 1" PEEK rod. The bulk electrolysis cell was designed to accommodate a large number of process connections in a very small area. The fittings

were designed to be seamlessly removed from the glass cell without twisting the process connections. 1/4-28 connections were used where possible. For gas in/out ports tubing was glued into slip fit holes with epoxy. Cross-shaped stir bars were found to provide the best stirring without spinning out.

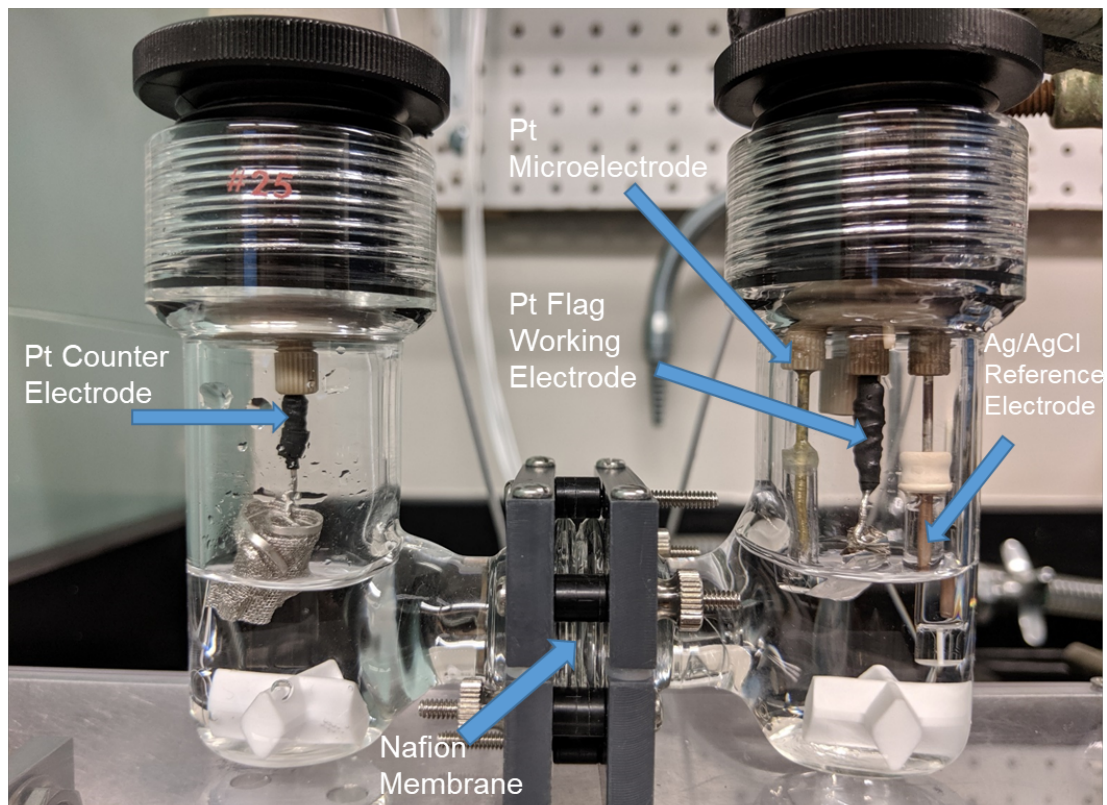


Figure 3. 13 Closeup of completed bulk electrolysis cell with process fittings.

A large area reticulated vitreous carbon electrode is used as the working electrode, platinum mesh for the counter electrode, and Ag/AgCl is used for reference electrode. Stirring is maintained on a custom-made dual stirring plate.

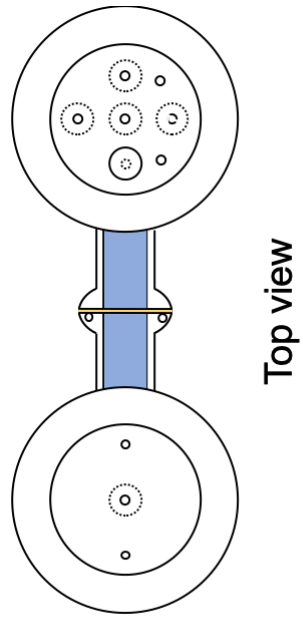
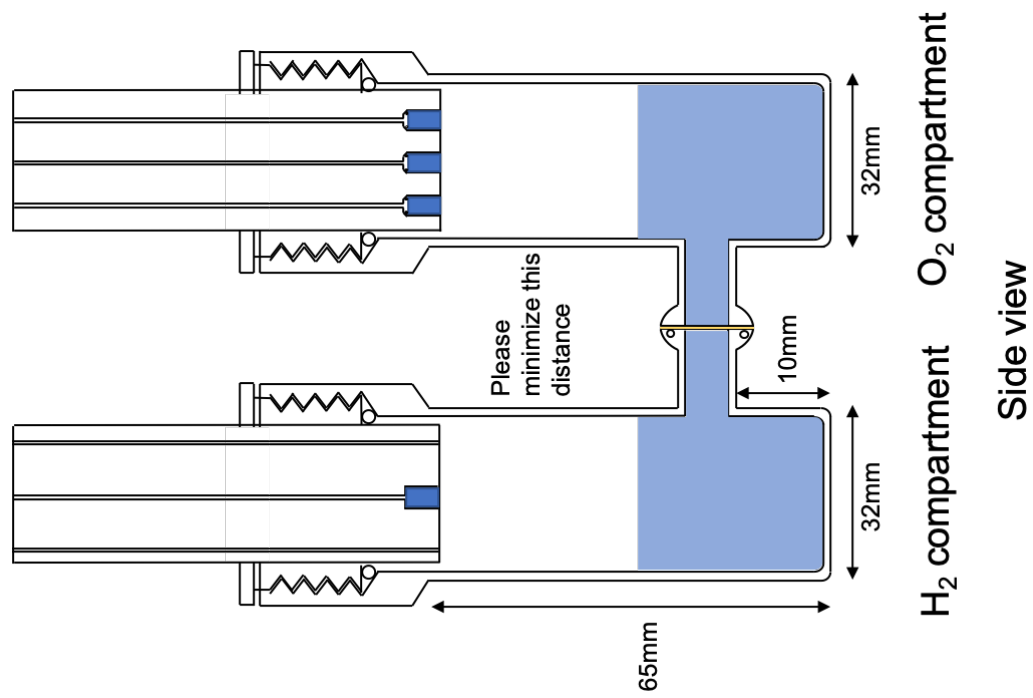
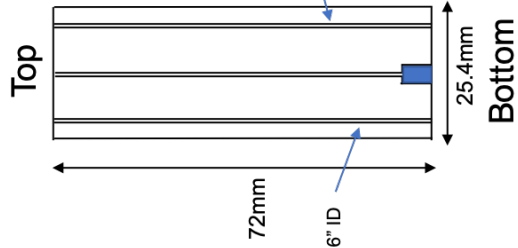
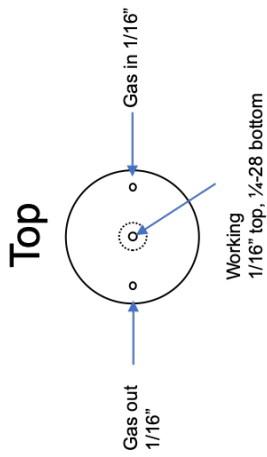


Figure 3. 14 Schematic of bulk electrolysis cell.

H₂ compartment adapter



O₂ compartment adapter

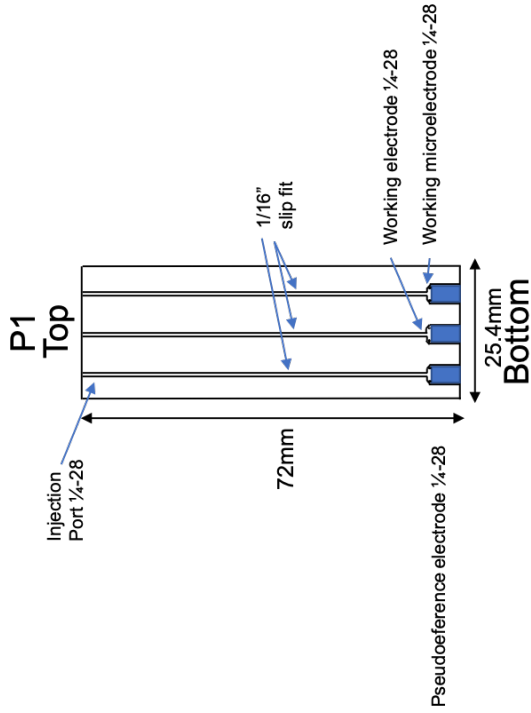
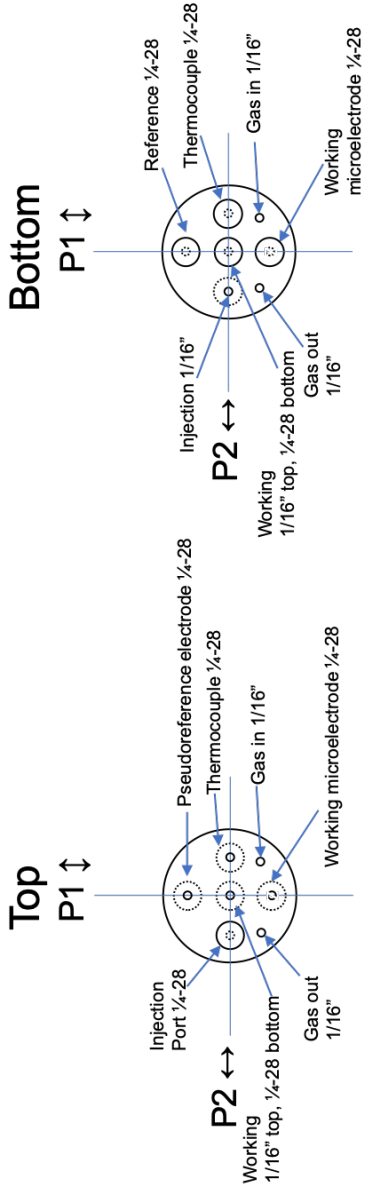


Figure 3.15 Schematic of bulk electrolysis cell.

Completion of this project will entail programming an interface for the automation panel, the potentiostat, and GC/MS. It may also be necessary to install a cryofocussing loop to remove water from the headspace sample before it enters the GC/MS. Finally, exploration of alternative anode materials such as indium tin oxide is warranted as glassy carbon will likely undergo decomposition at the potentials at which water oxidation is typically conducted (>1.6 V).

3.3 Conclusions and Future Work

While pressure data are a good measure of oxygen production it is helpful to have a second detection method to verify that oxygen is in fact produced. Future efforts will involve integrating a suitable O_2 detection method into the cell. There are alternative optical oxygen sensors from other manufacturers such as PyroScience that may be better suited to our application and worth further investigation. Additionally, there are robust polarographic systems available from companies such as EDAQ that offer a promising alternative to optical oxygen sensing.

The panel will require programming in LabView and consideration of several use cases will be necessary. CH Instruments potentiostats have limited LabView compatibility and thus an alternative instrument may be necessary for full automation. Given that the system samples headspace saturated with moisture, implementation of cryotrap will prolong the life of the GC column and may provide better gas separation. Finally exploration of anode materials other than glassy carbon, such as Indium Tin Oxide (ITO) would provide a useful site of comparison.

References

1. Grotjahn, D. B.; Brown, D. B.; Martin, J. K.; Marelius, D. C.; Abadjian, M.-C.; Tran, H. N.; Kalyuzhny, G.; Vecchio, K. S.; Specht, Z. G.; Cortes-Llamas, S. A.; Miranda-Soto, V.; van Niekerk, C.; Moore, C. E.; Rheingold, A. L. *J. Am. Chem. Soc.* **2011**, *133*, 19024.
2. Marelius David C.; Bhagan Salome; Charboneau David J.; Schroeder Kristine M.; Kamdar Jayneil M.; McGettigan Amanda R.; Freeman Benjamin J.; Moore Curtis E.; Rheingold Arnold L.; Cooksy Andrew L.; Smith Diane K.; Paul Jared J.; Papish Elizabeth T.; Grotjahn Douglas B. *European Journal of Inorganic Chemistry* **2014**, *2014*, 676.
3. Kamdar, J. M.; Marelius, D. C.; Moore, C. E.; Rheingold, A. L.; Smith, D. K.; Grotjahn, D. B. *ChemCatChem* **2016**, *8*, 3045.